TECHNICAL UNIVERSITY OF LIBEREC
Faculty of Mechatronics, Informatics
and Interdisciplinary Studies

# Large-Eddy Simulation for Aeroacoustics of Human Phonation

## Dissertation

*Study programme:* P3901 – Applied Sciences in Engineering
*Study branch:* 3901V055 – Applied Sciences in Engineering

*Author:* **Ing. Martin Lasota**
*Supervisor:* doc. Ing. Petr Šidlof, Ph.D.

Liberec 2022

# Declaration

I hereby certify, I, myself, have written my dissertation as an original and primary work using the literature listed below and consulting it with my thesis supervisor and my thesis counsellor.

I acknowledge that my dissertation is fully governed by Act No. 121/2000 Coll., the Copyright Act, in particular Article 60 – School Work.

I acknowledge that the Technical University of Liberec does not infringe my copyrights by using my dissertation for internal purposes of the Technical University of Liberec.

I am aware of my obligation to inform the Technical University of Liberec on having used or granted license to use the results of my dissertation; in such a case the Technical University of Liberec may require reimbursement of the costs incurred for creating the result up to their actual amount.

At the same time, I honestly declare that the text of the printed version of my dissertation is identical with the text of the electronic version uploaded into the IS STAG.

I acknowledge that the Technical University of Liberec will make my dissertation public in accordance with paragraph 47b of Act No. 111/1998 Coll., on Higher Education Institutions and on Amendment to Other Acts (the Higher Education Act), as amended.

I am aware of the consequences which may under the Higher Education Act result from a breach of this declaration.

.....
Martin Lasota

**Abstrakt (CZ)**
Disertační práce se zabývá numerickým modelováním 3D nestlačitelného proudění vzduchu při lidské fonaci pěti kardinálních samohlásek /u, i, ɑ, o, æ/. Vědecký přínos této práce je v popisu souvislosti mezi výpočtem turbulentního proudění při použití konvenčního subgrid modelu (jednorovnicový, WALE), či nově implementovaného anizotropního minimálně disipačního (AMD) subgrid modelu a jeho vlivu na aeroakustický výpočet fonace. Vzhledem k velké škále měřítek v turbulentním proudění a v akustice je simulace rozdělena tak, že výpočet nestlačitelného proudění v hrtanu je realizován metodou konečných objemů na jemné síti a zdroje zvuku včetně šíření zvukových vln od hrtanu až do vyzařovaného prostoru okolo úst metodou konečných prvků na hrubé akustické síti.

**Abstract**
This dissertation deals with numerical modeling of 3D incompressible laryngeal flow during human phonation of five cardinal vowels /u, i, ɑ, o, æ/. This work aims to describe the correlation between turbulent flow simulations with a conventional (One-equation, WALE) or newly implemented anisotropic minimum dissipation (AMD) subgrid-scale model and its impact on the aeroacoustic spectrum in human phonation. Given the large variety of scales in the flow and acoustics, the simulation is separated in two steps: computing the flow in the larynx using the finite volume method on a fine grid followed by computing the sound sources and wave propagation from the larynx to the radiation space around the mouth using the finite element method on a coarse acoustic grid.

**Klíčová slova (CZ)**
simulace pohybu velkých vírů; subgrid model; anizotropní minimálně disipační model; perturbovaná konvektivní vlnová rovnice; modelování lidské fonace;

**Keywords**
large-eddy simulation; subgrid-scale model; anisotropic minimum dissipation model; perturbed convective wave equation; human phonation modelling;

I gratefully acknowledge my doctoral supervisor Petr Šidlof from TU Liberec for the patient guidance, encouragement and advice he has provided me. I was lucky to have a supervisor who cared so much about this work and pushed me to sharpen my thinking in the research field.

Thanks also to Jan Valášek from TU Prague and Stefan Schoder from TU Wien for many helpful discussions and suggestions in developing this work.

Special thanks to Prof. Manfred Kaltenbacher from TU Wien for making my internship as a guest scientist at their institute possible. It has been an rewarding experience.

I express my sincere gratitude, respect and love to Veronika, who has proved indispensable in my personal life.

# Contents

# List of symbols

| Symbol | Dimension | Description |
|---|---|---|
| Latin alphabet | | |
| $\mathbf{a}^v$ | $\mathrm{m}^2.\mathrm{s}^{-1}$ | vector potential |
| $A_1, A_2$ | m | amplitude of oscillation |
| $c_0$ | $\mathrm{m}.\mathrm{s}^{-1}$ | speed of sound |
| $C_A$ | - | modified Poincaré constant (AMD model) |
| $C_S$ | - | Smagorinsky coefficient |
| $C_k, C_E, C_\Delta, C_m$ | - | model contants |
| $C_\nu, C_\epsilon, C_w$ | - | model contants |
| $\overline{\mathbb{D}}$ | $\mathrm{s}^{-1}$ | filtered stress tensor (OpenFOAM) |
| $F_1 - F_3$ | Hz | formant frequencies (formants) |
| $f, \overline{f}, f'$ | - | flow variable, filtered, fluctuating |
| $f_o$ | Hz | fundamental frequency |
| $f_2, f_3$ | Hz | second and third harmonic frequency |
| $f_{F1,F2,F3}$ | Hz | frequencies of the first three formants |
| $f_j$ | $\mathrm{N}.\mathrm{m}^{-3}$ | force density |
| $g$ | m | glottal gap |
| $G_{ij}$ | $\mathrm{s}^{-1}$ | velocity gradient tensor |
| $G_f$ | - | kernel (shape of the filter) |
| $G, \hat{G}$ | - | Green's function (time and freq. domain) |
| $I_\square, II_\square, III_\square, IV_\square$ | | first, second, third and fourth invariant of $\square$ |
| $k_w$ | $\mathrm{rad}.\mathrm{m}^{-1}$ | wave number |
| $k_{SGS}, k^W_{SGS}$ | $\mathrm{m}^2.\mathrm{s}^{-2}$ | subgrid kinetic energy |
| $K$ | Pa | bulk modulus |
| $h$ | m | height of the hill/channel |
| $L^{LH}_{ij}$ | $\mathrm{m}^2.\mathrm{s}^{-2}$ | Lighthill tensor |
| $L$ | dB | sound pressure level |
| $L_{f_o}$ | dB | sound pressure levels at fundamental frequency |
| $L_{F1,F2,F3}$ | dB | sound pressure level at first three formants |
| $p$ | Pa | static pressure |
| $p'$ | Pa | fluctuating pressure |
| $\overline{p}$ | Pa | filtered pressure |
| $p_0$ | Pa | temporal mean pressure |
| $p^a, p^a_{\mathrm{rms}}, p^a_{\mathrm{ref}}$ | Pa | acoustic pressure (root mean square, average) |
| $p^{ic}$ | Pa | incompressible pressure |
| $p^{(0)}$ | Pa | 'pseudosound' pressure (near-field) |
| $p^{(1)}$ | Pa | 'acoustic' pressure (far-field) |
| $P_k$ | $\mathrm{m}^2.\mathrm{s}^{-2}$ | kinematic pressure |
| $q_{\mathrm{ma}}, \mathbf{q}_{\mathrm{mo}}$ | $\mathrm{kg}/(\mathrm{m}^3.\mathrm{s})$, $\mathrm{kg}/(\mathrm{m}^2.\mathrm{s}^2)$ | source terms |
| $q_{\mathrm{vel}}, q_{\mathrm{vor}}$ | $\mathrm{m}.\mathrm{s}^{-2}$ | velocity and vortical source terms |
| $Q, q$ | $\mathrm{m}^3.\mathrm{s}^{-1}$ | volumetric flow rate |

| | | |
|---|---|---|
| $\mathbf{r}$ | m | spatial scale |
| $r$ | m | distance between the probe and sound generator |
| Re | - | Reynolds number<br>periodic hill |
| $\mathrm{Re}_\tau$ | - | Reynolds number based on friction velocity |
| $S_{ij}$ | $\mathrm{s}^{-1}$ | symmetric part of the<br>velocity-gradient tensor<br>or resolved rate-of-strain tensor |
| $s^d_{ij}$ | $\mathrm{s}^{-1}$ | symmetric part of a square of the<br>velocity-gradient tensor |
| $\overline{S}_{ij}$ | $\mathrm{s}^{-1}$ | filtered stress tensor $S_{ij}$ |
| St | - | Strouhal number |
| $t$ | s | time |
| $t_a$ | s | time of activating sound |
| $t_O$ | s | time at the maximum glottal opening |
| $t_C$ | s | time at the convergent position of vocal folds |
| $t_N$ | s | time at the divergent position of vocal folds |
| $\mathbf{u}$ | $\mathrm{m.s}^{-1}$ | velocity vector |
| $\mathbf{u}^a$ | $\mathrm{m.s}^{-1}$ | acoustic (particle) velocity vector |
| $\mathbf{u}_0$ | $\mathrm{m.s}^{-1}$ | temporal mean velocity |
| $\mathbf{u}_{\mathrm{jet}}$ | $\mathrm{m.s}^{-1}$ | glottal jet velocity |
| $\overline{\mathbf{u}}$ | $\mathrm{m.s}^{-1}$ | filtered velocity vector |
| $\mathbf{u}'$ | $\mathrm{m.s}^{-1}$ | fluctuating velocity vector |
| $U_b$ | $\mathrm{m.s}^{-1}$ | mean bulk velocity above hills |
| $\langle u \rangle$ | $\mathrm{m.s}^{-1}$ | temporal averaged velocity component |
| $u_i$,$u_i^{'}$ | $\mathrm{m.s}^{-1}$ | velocity components, fluctuating |
| $u_\tau$ | $\mathrm{m.s}^{-1}$ | friction velocity |
| $u^+$ | $-$ | normalized velocity |
| $w_{1,2}$ | m | sinusoidal displacement |
| $\mathbb{T}$ | Pa | viscous stress tensor |
| $\mathbb{T}^{\mathrm{LH}}$ | Pa | Lighthill tensor |
| $x_i$ | m | spatial coordinate |
| $\mathbf{x}^o$ | m | location of observer (vector) |
| $x^+, y^+, z^+$ | - | dimensionless wall distance |
| $y^+_{min}, y^+_{avg}, y^+_{max}$ | - | dimensionless wall distance<br>(minimum, average, maximum) |
| $\mathbf{y}^s$ | m | location of source (vector) |

| **Symbol** | **Dimension** | **Description** |
|---|---|---|
| Greek alphabet | | |
| $\delta_{ij}$ | - | Kronecker delta |
| $\delta_d$ | - | Dirac delta |
| $\delta x_i$ | m | filter width of the LES filter (AMD model) |
| $\Delta$ | m | filter width of the LES filter |

| | | |
|---|---|---|
| $\Delta x^+, \Delta y^+, \Delta z^+$ | - | grid spacing in wall units |
| $\Delta l^a$ | m | acoustic element length |
| $\Delta t^a$ | s | acoustic time step |
| $\Gamma_{\text{in}}, \Gamma_{\text{out}}, \Gamma_{\text{wall}}$ | - | boundary (inlet, outlet, walls) |
| $\Gamma_{\text{bVF}}, \Gamma_{\text{uVF}}$ | - | boundary (bottom and upper vocal folds) |
| $\Gamma_{\text{back}}, \Gamma_{\text{front}}$ | - | boundary (z-normal) |
| $\epsilon$ | $\text{m}^2.\text{s}^{-3}$ | dissipation rate |
| $\mu$ | Pa.s | dynamic viscosity |
| $\mu_t$ | Pa.s | turbulent dynamic viscosity |
| $\mu_{eff}$ | Pa.s | effective dynamic viscosity |
| $\nu$ | $\text{m}^2\,\text{s}^{-1}$ | kinematic molecular viscosity |
| $\nu_t$ | $\text{m}^2\,\text{s}^{-1}$ | kinematic turbulent (SGS) eddy viscosity |
| $\nu_t^S, \nu_t^O, \nu_t^W, \nu_t^A$ | $\text{m}^2\,\text{s}^{-1}$ | turbulent viscosity by the Smagorinsky, One-Equation, WALE and AMD model |
| $\nu_t^{QR}$ | $\text{m}^2\,\text{s}^{-1}$ | turbulent viscosity by the QR model |
| $\psi^{\text{a}}$ | $\text{m}^2.\text{s}^{-1}$ | acoustic scalar potential |
| $\text{D}\psi^{\text{a}}/\text{D}t$ | $\text{m}^2.\text{s}^{-2}$ | total derivative of the acoustic potential "acouPotentialD1" |
| $\text{D}p^{ic}/\text{D}t$ | $\text{Pa.s}^{-1}$ | PCWE term |
| $\lambda$ | m | wave length |
| $\rho$ | $\text{kg.m}^{-3}$ | density |
| $\rho^{'}$ | $\text{kg.m}^{-3}$ | fluctuating density |
| $\overline{\rho}$ | $\text{kg.m}^{-3}$ | filtered density |
| $\rho_0$ | $\text{kg.m}^{-3}$ | temporal mean density |
| $\rho^a$ | $\text{kg.m}^{-3}$ | acoustic density |
| $\tau_{ij}$ | $\text{m}^2.\text{s}^{-2}$ | exact sub-grid scale stress tensor |
| $\tau'$ | Pa | perturbed viscous stress tensor |
| $\tau_w$ | Pa | wall shear stress |
| $\boldsymbol{\omega}$ | $\text{s}^{-1}$ | vorticity vector |
| $\omega$ | $\text{rad.s}^{-1}$ | angular frequency |
| $\Omega_{ij}$ | $\text{s}^{-1}$ | deviatoric part of the velocity-gradient tensor |
| $\xi_1, \xi_2$ | rad | phase difference of vocal folds oscillations |
| $\mathcal{O}$ | | Bachmann–Landau notation |
| $\square^{\text{ic}}$ | | incompressible field variables |
| $\square^{\text{a}}$ | | acoustic quantities |
| $\hat{\square}$ | | Fourier transformed variables |

## Abbreviations

| | |
|---|---|
| AMD | Anisotropic Minimum Dissipation |
| APE | Acoustic Perturbation Equations |
| CAA | Computational AeroAcoustics |
| CFD | Computational Fluid Dynamics |
| CT | Computed Tomography |
| DNS | Direct Numerical Simulation |

| | |
|---|---|
| FFT | Fast Fourier Transform |
| FEM | Finite Element Method |
| FSI | Fluid-Structure Interaction |
| FVM | Finite Volume Method |
| IPA | International Phonetic Alphabet |
| SGS | Subgrid-Scale |
| LAM | "laminar model" for turbulent flow (DNS on a coarse grid, no SGS model influence on large-scales) |
| LEE | Linearized Euler Equation |
| LES | Large-Eddy Simulation |
| LES-NWR | LES with Near-Wall Resolution |
| LES-NWM | LES with Near-Wall Modeling |
| OE | One-Equation eddy-viscosity |
| OpenFOAM | Open Field Operation and Manipulation (open source software for CFD) (https://cfd.direct/openfoam/) |
| OpenCFS | Open Coupled Field Simulation (open source software for CAA) (https://www.opencfs.org/) |
| PCE | Perturbed Compressible Equations |
| PCWE | Perturbed Convective Wave Equation |
| PML | Perfectly Matched Layer |
| RANS | Reynolds-Averaged Navier-Stokes equations |
| SMAG | Smagorinsky model |
| SPL | Sound Pressure Level |
| tVSA | triangular Vowel Space Area |
| VAI | Vowel Articulation Index |
| VLHR | Very Low tone to High tone Ratio |
| WALE | Wall-Adaptive Local Eddy-viscosity |

**Mathematical operators**

| | |
|---|---|
| $\boldsymbol{\nabla} b$ | gradient of scalar-valued function $b$ |
| $\boldsymbol{\nabla} \cdot \mathbf{b}$ | divergence of vector-valued function $\mathbf{b}$ |
| $\boldsymbol{\nabla} \times \mathbf{b}$ | curl of vector-valued function $\mathbf{b}$ |
| $\Delta b = \boldsymbol{\nabla} \cdot \boldsymbol{\nabla} b$ | laplacian of scalar-valued function $b$ |
| $\mathrm{D}/\mathrm{D}t$ | total (substantial) temporal derivative |
| $\mathbf{b}^\top$ | transpose of vector-valued function $\mathbf{b}$ |
| $\mathbf{a} \otimes \mathbf{b}$ | dyadic (outer) product |

# 1 Introduction

## 1.1 Principles of voice production

The generation of a human voice is a highly complex biophysical process, where the viscoelastic multi-layered tissues of the vocal folds interact with the airflow expired from the lungs, start to self-oscillate, and close the channel periodically. The vocal fold oscillation and glottal closure modulate the mass flux, create complex turbulent structures and pressure disturbances, which form the voice source. This source signal is modulated by the vocal tract, radiated from the mouth, and perceived as a human voice. Physiological principles are precisely described in the monograph by Titze (1994).

Phonation is performed by true vocal folds, a unique paired anatomical structure, see Fig. 1.1. This paired structure produces vibrational modes during phonation, possibly due to a very soft laminated structure of lamina propria which sits between thyroarytenoid muscle and overlying epithelium surface. Elastin, colagen and interstitial proteins are fundamental to pliability and extensibility of the vocal folds, known from several voice pathology studies (Stemple et al., 2018). The vibration of true vocal folds, hereinafter called vocal folds, is one of the dominant sound sources. Phonation relies on pulmonary respiratory power caused by the abdominal and thoracic musculature. During abdominal (belly) and thoracic (upper chest) breathing the lungs are simultaneously pulling downward, followed by exhalation when the diaphragm rises back to the relaxed position. In the case of quiet exhalation, the vocal folds are abducted (open) as shown in Fig. 1.1 (left), and no sound is generated. During phonation (see Fig. 1.1 (right)), the airflow from lungs is constricted and the vocal folds are adducted (closed, in contact). This effect builds up the subglottal pressure below adducted vocal folds until vocal folds are blown apart and set the surface covering vocal folds to oscillate.

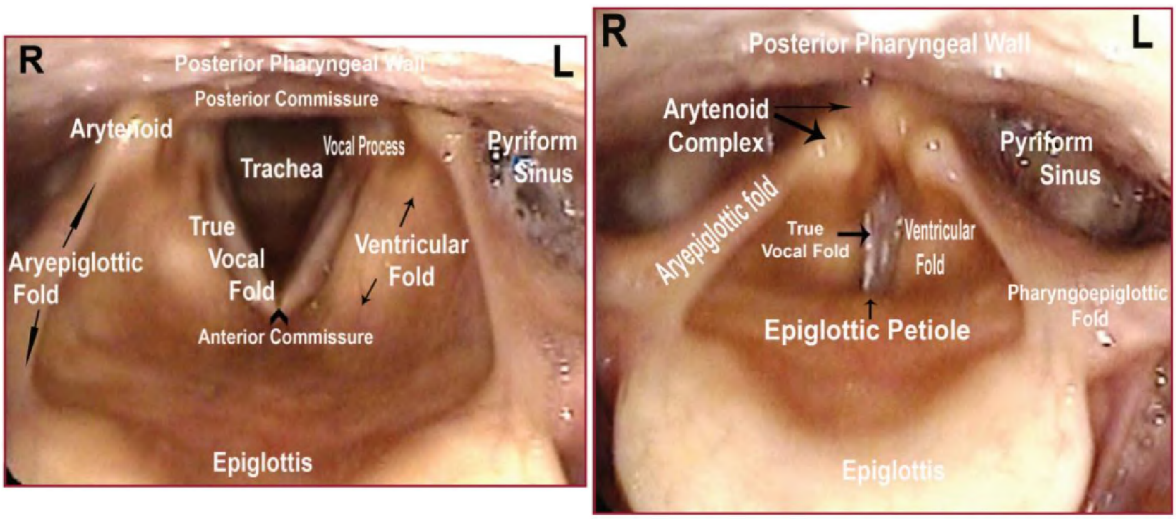


Fig. 1.1: Endoscopic view of the larynx and surrounding structures. **Left:** Fully open in respiratory position (abducted). **Right:** during speech (adducted). Overtaken from Stemple et al. (2018).

The rate between the subglottal pressure from lungs and the pressure in the glottis influences the quality of phonation (pitch, loudness, nasality etc.).

Vocal folds are able to produce four kinds of oscillations (vocal registers). The registers are divided according to kind of vibrations, ordered from the lowest register they are: (1) vocal fry, (2) modal, (3) falsetto and (4) whistle. The vocal fry register is characterized as a bubbling of air through the totally relaxed adducted vocal folds. The modal (or normal) register is typical register used in speech and lower singing voice, where the entire structure of the vocal folds oscillates with complete closure of the glottal channel for a considarable portion of the oscillation cycle. On contrary, the falsetto register is caused primarily by oscillation of edges of vocal folds rather than whole vocal folds. And the last whistle register occurs when muscles of lateral cricoarytenoid are more active than the transversal ones. This atypical muscle clenching causes the highest tones of which the vocal folds are physiologically capable (Titze, 1994).

Sound waves are carried upward in the direction of exhalation through a relatively short supraglottal volume. Afterward sound waves travel through the pharynx and articulatory structures. This airway full of cavities prolongs and reinforces acoustic waveforms. The passage is named uniformly as a vocal tract (filter). In reality, the vocal tract consists of the velum, teeth, tongue, hard and soft palate, and other structures contributing to the resonance of the entire respiratory tract. Speech created only by vocal folds without any contribution of the resonating vocal tract is just atonal buzz.

Fig. 1.2 illustrates the source-filter theory (Titze, 1994) of vocal production, where the dominant source is located in the larynx. The vocal fold oscillation is characterized by the so-called fundamental frequency $f_o$, and the sound waves travel downstream to the supralaryngeal vocal tract. The immediate shape of the vocal tract has its own resonant frequencies, which are typically called and written as formants $F_1 - F_4$. Resonances of vocal tracts are always higher than fundamental frequency $f_o$, hence the resonances have no or a very little influence on $f_o$ (Wolfe et al., 2009). The ranges of fundamental frequencies are observed from 85 to 155 Hz for adult males and from 165 to 255 Hz for adult females (Baken and Orlikoff, 2000) for ordinary spoken speech.

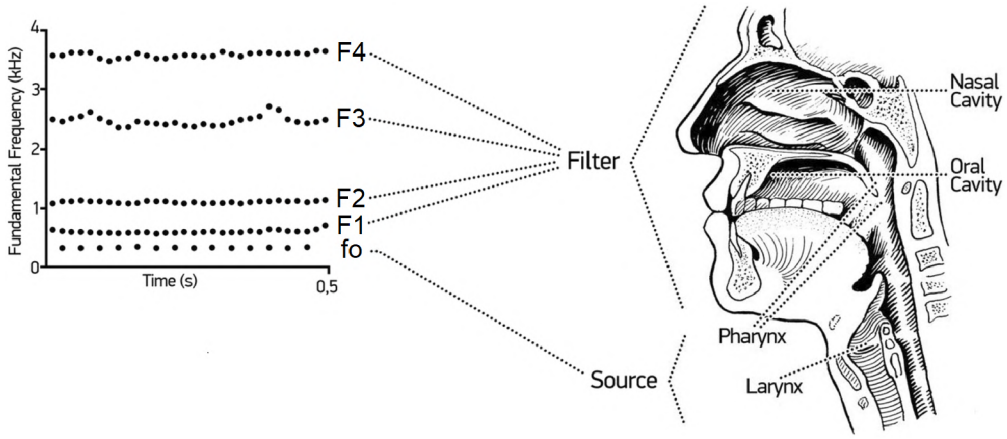


Fig. 1.2: Spectrogram of a vocalization of the vowel /a/, fundamental frequency $f_o$ and formants $F_1 - F_4$. Overtaken from Kamiloğlu et al. (2020).

More informative illustration based on the source-filter theory of voice description is shown in Fig. 1.3. From left: (1) The laryngeal source spectrum is formed by the vocal

fold oscillation, (2) the vocal tract transfer function is affected by resonance frequencies of the vocal tract itself, and (3) the previous two signals are composed into the voice spectrum, which the speaker emits and others hear. The fundamental frequency $f_o$ in the spectrum of the laryngeal source is followed by the harmonic series $f_n = f_o(n+1)$. In the broad voice spectrum, is it still a question of how to detect formants $F_1 - F_4$ precisely (usually two-three human formants are enough to determine the vowel). Some authors present their methods how to plot a spectrum envelope (as is marked by the blue line in Fig. 1.3) to identify formants (Fant, 1970; Benade, 1990). Other research groups use a more scientific approach to detect formants by the autoregressive filter based on Atal and Hanauer (1971).

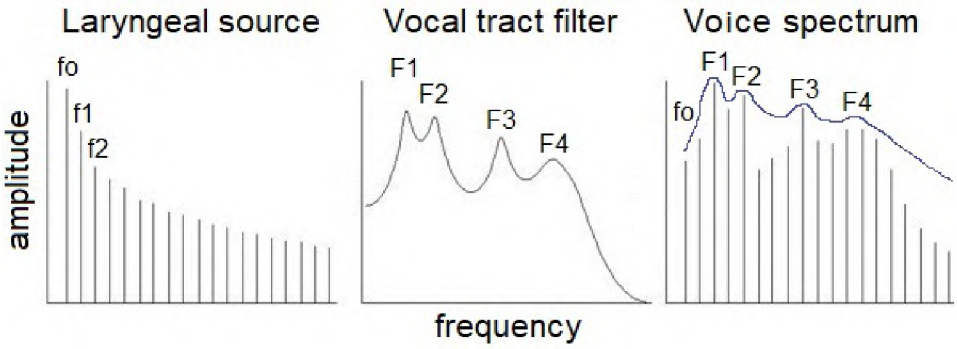


Fig. 1.3: Source-filter theory of speech production.

Locations of each formant frequencies $F_1, F_2, ..., F_n$ are affected by many factors, for example, the height and advancement of the tongue defining the articulatory working space, in general all cavities in the vocal tract. Cavities can amplify and attenuate frequencies as a band-pass filter, and damp and/or enhance specific ranges of frequencies. In non-human vocal tracts, resonant properties are often static and more predictable compared to human vocal tracts (Fitch, 1994). Human vocal tracts are much more complex, defined as series of cross-sectional areas measured from glottis to mouth. The length and shape of vocal tracts influence formant frequencies, where the main determinants are set of muscles encircling the pharynx, such as pulling the tongue backward in the example "father" (vowel /a/), or pulling the tongue front in example "beet" (vowel /i/) related with genioglossus muscle, or tongue position holding backward and up in the example "boot" (vowel /u/) related with styloglossus muscles (Fitch, 1994). Fig. 1.4 (right) shows these vowels written in the international phonetic alphabet distinguishing the vowels based directly on the tongue position, i.e. as front, central and back lines at first. The letters around the point e.g. (i•y) mean the "unrounded" /i/ and "rounded" /y/ vowel, respecting the lips position. The frontmost vowel is /i/, the highest and backmost vowel /u/, the lowest and front vowel /æ/, the lowest and backmost /ɑ/ etc. The vowels /u, i, ɑ/ are found in almost all languages on the world (Kuhl et al., 1997).

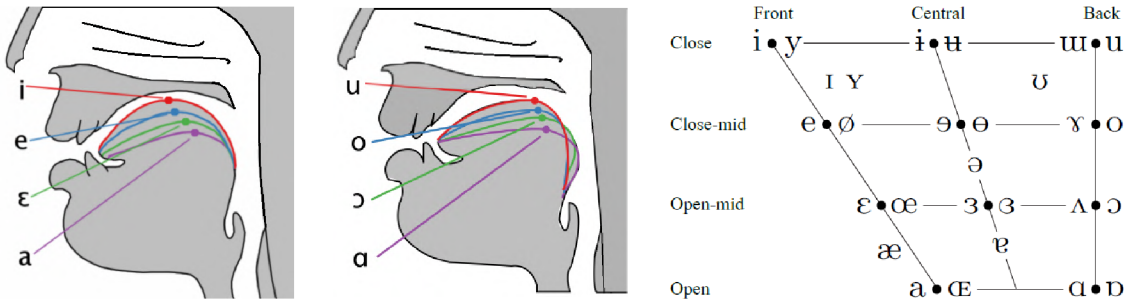


Fig. 1.4: **Left:** Position of the tongue relative to the vowels. **Right:** International Phonetic Alphabet (IPA).

The flow exhalation through the oral cavity, Fig. 1.4 (left), can be amplified when the velum is pulled up and back to seal off the nasal cavity. On the contrary, the phonation performed by both cavities (oral and nasal) is called a "nasalized" sound, for example, by a consonant /m/. Typical speakers where nasalization is common are French (more than with vowel quality, they manipulate with vowel length).

A graphic representation of voice in terms of its frequencies is shown in recordings in Fig. 1.5, where the x-axis is time (0-500 ms) and the y-axis is the frequency (0-4,000 Hz). The dark spots in the spectrogram denoted by the arrows correspond to formants ($F_1, F_2, F_3$). The intensity of the black color corresponds to the prevalence of the specific frequency. As it was seen in the rectangular trapezoid in Fig. 1.4 (right), the vowels are placed at a higher (e.g. /i, u/) and lower position (e.g. /a, ɑ/). The height of the vowel is inversely related with the first formant $F_1$, i.e. the higher placed vowel /u/ corresponds to the lower first formant $F_1$ compared to /a/. Fig. 1.5 (left) shows the first formant $F_1$ in red rectangles, which mark the high vowels. They resonate at lowest frequencies /i, u/ $\sim 280 - 310$ Hz, whereas the blue rectangles mark the first formant $F_1$ for the mid/low vowels /æ, ɑ/ $\sim$ 690 – 710 Hz. Fig. 1.5 (right) shows the same spectrogram as on the left side, but with the marked second formant $F_2$. The second formant is related to degree of backness, the green rectangle highlights front vowels (with higher $F_2$, /æ, i/ $\sim 1660 - 2250$ Hz) and the purple rectangle shows back vowels (lower $F_2$, /u, ɑ/ $\sim 870 - 1100$ Hz).

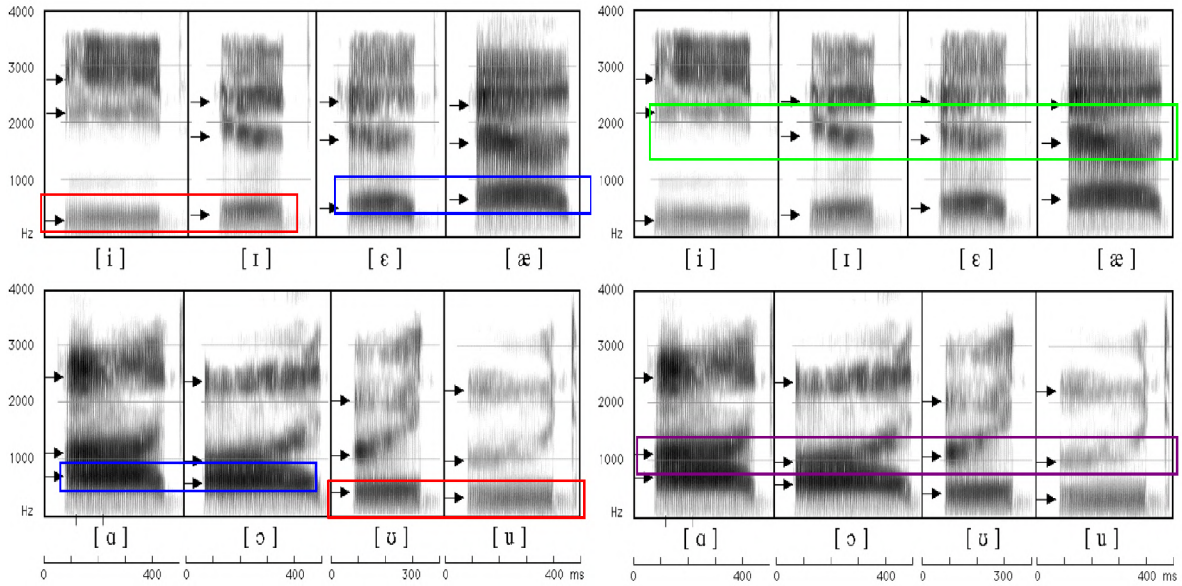


Fig. 1.5: Two identical spectrograms of eight vowels. **Left:** with marked $F_1$, high (red) and mid/low (blue) vowels. **Right:** with marked $F_2$, front (green) and back (purple) vowels. Source: (Shriberg et al., 2003)

## 1.2 Diagnostic methods

Diagnostic methods in voice production consist of instrumental and voice analysis. The instrumental analysis can be:

1. Clinical examination of the larynx (laryngoscopy), where the flexible laryngoscope is inserted through the nose or mouth into the larynx, equipped with an optical adapter for recording a video (videolaryngoscope) and source of light, see Fig. 1.1. To display complex vocal folds motions in detail, VKG techniques (VKG, HSDK and SVKG) were invented, i.e. videokymography (VKG), high-speed digital kymography (HSDK) and strobovideokymography (SVKG). VKG delivers kymographic images in real time whereas the other techniques construct the kymographic images from recordings. (Švec and Schutte, 2012).

2. Laboratory voice analysis (electroglottography (EGG)), where EGG is performed through a laryngograph, which measures impedance between contact electrodes placed on both sides of the thyroid cartilage. The signal is called the electroglottogram, which can monitor the closure of vocal folds (by contact of superficial mucosa layers).

Voice analysis has countless methods, here will be referred only those which appear in the chapter Voice disorders. Triangular vowel space area (tVSA) (1.1) and the vowel articulation index (VAI) (1.2) are extracted from the first two formants of vowels /ɑ, i, u/ by calculating (Skodda et al., 2012)

$$tVSA = \left| \frac{F_1^{/i/}(F_2^{/a/} - F_2^{/u/}) + F_1^{/a/}(F_2^{/u/} - F_2^{/i/}) + F_1^{/i/}(F_2^{/i/} - F_2^{/a/})}{2} \right|, \tag{1.1}$$

$$VAI = \frac{(F_2^{/i/} + F_1^{/a/})}{(F_1^{/i/} + F_1^{/u/} + F_2^{/u/} + F_2^{/a/})}. \tag{1.2}$$

A relatively easy technique to analyse the speech is to ask the patient to produce isolated syllables /pa/-/ta/-/ka/ as quickly as possible and as long as possible with breath. The acoustic method of repetition /pa/-/ta/-/ka/ is called diadochokinesis in clinical neurology at pre-clinical stages (Konstantopoulos et al., 2017). Another technique VLHR (Very Low tone to High tone Ratio) is used in routine as an index of nasality. The value is evaluated as a sum in dB of the low power spectrum in the range 50-600 Hz divided by a sum of high power spectrum from 601 to 8063 Hz (Lee et al., 2009).

The quality of voice can be discussed by terms jitter and shimmer (Rammage, 2013), which are defined usually from prolonged vowels /i, ɑ/. The existence of jitter means fluctuation of glottal cycle length, see Fig. 1.6 (middle) compared to reference voice Fig. 1.6 (left). Evaluation of jitter allows for early detection of carcinoma of the larynx and is related to the physiological condition rather than age. The existence of shimmer, Fig. 1.6 (right), shows different amplitude in each period. The shimmer is measured together with the jitter and can be the first signal of cancerous lesions on the vocal folds. Aging may also start a shimmer in voice, mainly related to vocal folds weakness.

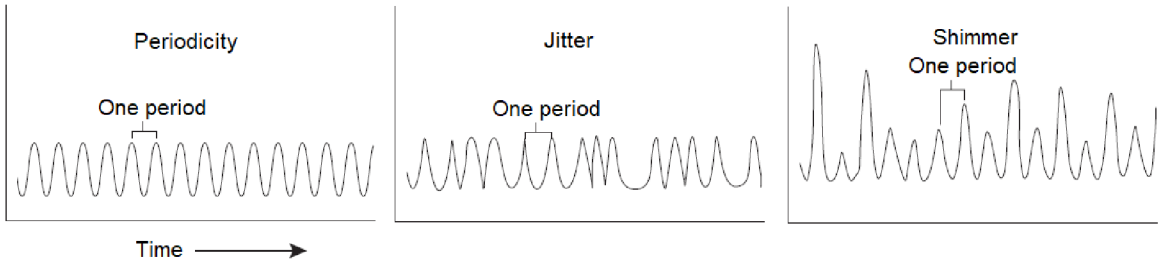


Fig. 1.6: Perturbations (jitter and shimmer) in the glottal source waveform. Overtaken from Rammage (2013).

## 1.3 Voice disorders

Most of the acoustic energy is contained in the fundamental frequency $f_o$ generated by vocal folds. Therefore one might think that healthy vocal folds have to be a guarantee of a healthy voice. Still, the situation is more complicated; the voice is also rapidly changed with the onset of neurological disease and being a physiologically healthy man at the same time. Voice disorders are also connected with common colds, as everyone has encountered, but this chapter will focus on more severe voice disorders.

*Nodules, polyps.* Among the structural disorders are, for example, vocal fold nodules, small calluses, usually located on each vocal fold separately. The voice handicapped

with nodules is perceived as singing. On the contrary, vocal fold polyps and cysts occur unilaterally and they are filled by fluid or solid. Vocal fold polyps are benign lesions with individual symptoms as hoarseness, or breathiness and vocal fatigue (Vasconcelos et al., 2019).

*Laryngitis.* Other organic causes, such as laryngitis, are caused by viruses, bacteria, tumors, parasites, antigens from the contaminated environment, and trauma (Dworkin, 2008). The immune system responds to the inflammation of the tissues of the larynx in the body and significantly affects the main functions of the larynx, which are voice production, breathing, coughing and swallowing processes. But without this protective reaction, the afflicted tissues could not survive. The larynx is an integral component of the anatomic framework. Hence the inflammation that arises within the unified airway is able to spread in the whole respiratory tract. Thereby, the voice is changed by a degree of acute laryngitis and the voice is associated with a dry barking cough, muffled voice, hoarseness, meaning the patient cannot fully control the pitch and timbre of the voice. The recent study published by Peters et al. (2021) pointed out also an effect of the physical condition of the laryngeal mucus layer on lubricating the vocal folds and viscoelasticity of vocal folds. The fact about the rigidity of mucus layers by smokers is not so surprising, nicotine was found to reduce the thickness of the mucus layer. In general, mucus is filled with 90-95% of water, 1-5% of mucins, 1% electrolytes, 1-2% lipids, other proteins etc. Especially mucins, the main component of mucus, determine vocal folds viscoelasticity.

*The Parkinson's disease* manifests itself even up to 5 years before the diagnosis by reduced vocal tract volume, tongue flexibility and articulation rate. Also, the narrower vocal range of pitches that a human is able to phonate was observed from audio samples of the healthy subjects and subjects with a confirmed diagnosis (Vaiciukynas et al., 2017). The increasing amount of samples can allow training the software helping to match the voice recorded on a smartphone's microphone with a diseased voice with some accuracy. For example, the study published by Orozco-Arroyave et al. (2015) contains a dataset including 35 Czech speakers, i.e. 20 voices affected by Parkinson's disease and 15 samples with healthy voice, following 100 Spanish speakers, and subsequent 170 German speakers. A total of four speeches were prepared, including sustained vowels, sentences repetition, read text and monologue. Results stated lower VAI (1.2) for patients with Parkinson, which means the loss of dopaminergic neurons in the mid-brain as a consequence of Parkinson disease and getting old. In addition, the tVSA value (1.1), which is computed from the first two formants as well as VAI, was significantly lower only for female patients. These indicators can be the first sign of starting the disease, directly from the locations of vowels. Towards both groups of subjects, no motor symptoms were observed, only the articulation imprecision as a predominant characteristic of Parkinson's disease. The accuracy of the method for the fore-mentioned three languages gained 98% in monologues, where the measured subject got a task to speak about daily activities for around 180 seconds and read 80 words from a paper. More results from General University Hospital in Prague can be find in Rusz et al. (2013). Medical interventions and also the progress of the disease may affect vowel articulation. The quality of each vowel is determined primarily by acoustic energy emitted by the first two formant frequencies, which are controlled inversely with tongue height and tongue advancement (Kent et al., 1999). Recordings are typically made 15-30 cm from the subject's mouth, and subjects are instructed to say a short sentence in one breath and repeated it five times. The minimal length of the vowel had to be 40 ms. Concerning the mechanism responsible for the speech in Parkinson's

disease, speech impairment is attributed to dopamine deficiency as well as hypokinesia and rigidity of the vocal tract. Articulation of the vowel /u/ requires more involvement of the orofacial muscles than in cases /i, ɑ/, thereby the measurement of $F_2^{/u/}$ based on a single vowel showed the most sensitive differentiation between the healthy and diseased groups. Acoustic measurements of the vowel articulation is a promising method for detecting the severity of Parkinson's disease early, monitoring the progress, etc.

*Down syndrome.* The voice of the Down syndrome population is perceived as breathy, rough and low-pitched (Jeffery et al., 2018). The measurements are focused on fundamental frequency, jitter (perturbation of frequency), shimmer (amplitude variation) and the so-called harmonic-to-noise ratio (extra noise in the harmonic spectrum) (Jeffery et al., 2018). The study published by Moura et al. (2008) reported the elevated study of jitter and shimmer during sustained vowels /a, e, i, o, u/ of 66 Portuguese children (4-6 yo) with Down syndrome. The children sustained vowels at lower fundamental frequencies, got higher perturbations in shimmer and jitter, and increased the ratio between the noise and strength of the phonation. The perceived voice quality by adults with Down syndrome results in detection of slightly higher mean fundamental frequency compared to a healthy population, but the other parameters were not so evident. Down syndrome is projected to the voice by several factors: harmonic-to-noise ratio, laryngeal tension, etc. In other studies, for example, published by Seifpanahi et al. (2011), the jitter was observed lower in Down population and the shimmer plus-minus comparable compared to healthy population.

*Myasthenia Gravis.* The disease manifests itself by an error in the transmission of nerve impulses to muscles. Phonatory function assessment is done using sustained phonation of the front vowel /a/ in combination with reading. The jitter, standard deviation from a fundamental frequency were higher compared to the healthy population. The group with the Myasthenia Gravis had a longer silence between /pa/-/ka/ productions and a higher duration of the consonant /t/ when the syllable /ta/ was produced.

*Vocal Tremor.* The vocal tremor is another neurological disease, which can affect voice production. This diagnosis may result in tremulousness of the larynx, tongue and palate. In the majority of cases, the physiological tremor has a frequency 8-12 Hz (Hertegård et al., 2000). In speech, it is characterized by periodic modulation in pitch, loudness and voicing. To soft this handicap, patients are treated with laryngeal botulinum toxin injections directly targeting thyroarytenoid muscles (Hertegård et al., 2000). The diagnosis of the vocal tremor is divided into several methods of investigation, i.e. with palpation, especially on abdominals, chest walls and vertical movements of the larynx (Hemmerich et al., 2017). Detection of the vocal tremor from abdominal walls by plethysmography measured from a breathing mode was also often used, but it proved to be very ineffective (under 35%). On the other side, the laryngoscopy (or nasendoscopy) focused on vocal folds and supraglottic structures can confirm the diagnosis in 95% of cases.

*Cleft Palate.* The sound production can be negatively influenced by excessive coupling of the oral and nasal cavity, resulting in an additional resonance called hypernasality. The voice of the population with cleft lips and cleft palates is an example of abnormal resonances, which results in poor speech intelligibility. In a recent study published by Dodderi et al. (2016), 30 children (8-15 yo) with congenital cleft of palates were measured to produce in 5 seconds sustained vowels /a/, /u/ and /i/ at a comfort loudness settled by a participant. The gained records were analysed in Praat software (Phonetic Sciences, University of Amsterdam) with the integrated Hillenbrand algorithm to extract VLHR.

The result score in dB was compared between preoperative and postoperative patients to discuss the varying level of hypernasality.

*Attention Deficit Hyperactivity Disorder (ADHD).* The most common neurodevelopmental disorder, ADHD is occurring most in childhood. In study published by Barona-Lleo and Fernandez (2016) performed on children (5-13 yo), including 44 patients with ADHD and 35 patiens as a control healthy group were measured. The assessment protocol observed higher subglottal pressure and lower transglottal flow rate than the control healthy group. The subglottal pressure is computed as a difference between the tracheal and pharyngeal pressures, and the transglottal flow is defined from the sum of airflows exhaled from the nose and mouth. The treatment for the ADHD population would be speech therapy containing special training programs to manipulate with the breath, phonation techniques to optimize the air for emitting the voice, and in combination with pharmacotherapy. As many investigations confirmed, the pathological findings are very common among by the ADHD children (more than 90%). In the majority of cases, it is about vocal nodules.

A particular group of voice disorders is speech-articulation disorders connected with difficulties to activate articulatory muscles precisely. *Dysarthria* is a complete inability or weakness to control the face, mouth and respiratory system. The voice is stated as soft, weak and slurred. A very similar handicap with the lack of speech musculature is the *apraxia disease* when patients have difficulty sequencing sound. Associated with speech fluency are stuttering and cluttering. The first occurs when repetitions disrupt the flow of the speech and the latter when speaking is excessive.

## 1.4 State of the art in human phonation modeling

Owing to the restricted access to the glottis, human phonation numerical modeling is becoming increasingly important. For example, the phonation model "simVoice" (Maurerlehner et al., 2021) is developed and based on an extended experimental database for voice treatment (specific vocal fold motions and boundary conditions), obtained at University Hospital Erlangen and Freiburg (Birk et al., 2017; Probst et al., 2019). During recent decades, numerical simulation of human phonation has advanced considerably towards a state where full-scale aeroacoustic simulations on realistic CT- or MRI-based geometries are possible. It can be anticipated that soon these simulations could be used for subject-specific pre-surgical predictions of vocal fold oscillations and resulting voice quality for people suffering from various vocal fold dysfunctions (Sadeghi et al., 2019a,b), or for the development of vocal folds prostheses. Authors of the simVoice software refer to a good agreement with acoustic measurements and state as a critical factor to further efficiency the optimization of the CFD part in their CFD-CAA workflow. An example of usage of simVoice in a clinical environment can be as follows. (1) The motion of vocal folds is measured by a high-speed imaging camera and the voice is recorded. (2) The examined human larynx and vocal tract are recorded by a magnetic resonance imagining. (3) The simVoice model is adapted regarding to findings and specific physiology of the patient. (4) The original and modified geometric models of the larynx are uploaded into the phonation software. In other words, the simVoice model confirms the efficiency of the suggested surgical treatment. (5) The numerical model of phonation can offer precise arguments to accept or decline a proposal for surgical

intervention. The presented workflow (1)-(5) aims to improve surgical and medical treatment of voice disorders. However, although powerful numerical simulation tools are available, the numerical methods still face challenges due to the nonlinear phenomena both in solid and fluid mechanics. One more reason why the simulations are not performed in units of lower hours is a necessity to compute 3D simulations to get a realistic turbulent flow (Mattheus and Brücker, 2011).

### 1.4.1 CFD simulations

Tab. 1.1 summarizes flow parameters for voiced speech (Baken and Orlikoff, 2000).

Tab. 1.1: Flow parameters - fundamental frequency of vocal fold oscillation $f_o$, volumetric flow rate $Q$, glottal jet velocity $|\mathbf{u}_{\text{jet}}|$, glottal gap $g$, Reynolds number Re, Strouhal number St.

| **Variable** | **Value** | **Variable** | **Value** |
|---|---|---|---|
| $f_o$ | $80 - 220$ Hz | $Q$ | $0.08 - 0.25$ l/s |
| $\|\mathbf{u}_{\text{jet}}\|$ | $15 - 45$ m/s | $g$ | $\mathcal{O}(1\,\text{mm})$ |
| Re | $\mathcal{O}(100) - \mathcal{O}(10,000)$ | St | $\mathcal{O}(0.001) - \mathcal{O}(0.01)$ |

The male vocal folds occupy the lower range of $f_o$. Low values of the Strouhal number led to an idea of a quasi-steady flow field (Mongeau et al., 1997), but lately, it has been shown that the high accelerations caused by fast-changing from the convergent and divergent position of vocal folds are dependent on a Reynolds-Strouhal relationship corresponding more to unsteady flow. Based on current knowledge, intraglottal and supraglottal flow features have been shown to affect vocal folds vibration $f_o$ and, therefore, with no big doubt phonation itself. The flow pattern is affected by jet formation, shear-layer instabilities, vortex shedding and transition to turbulence (Zhang et al., 2002a). Measurements on excised canine larynges suggest that the airflow in the trachea, subglottal and intraglottal space is typically laminar but encounters transition to turbulence shortly downstream of the glottis (Alipour and Scherer, 1995; Oren et al., 2009; Alipour and Scherer, 2006). The vortex dynamics in the supraglottal spaces and vocal tract are governed by turbulent momentum transfer. Turbulence also induces a broadband sound source, which is important especially in the case of breathy phonation, but also significant in the case of modal voice (Zhang, 2016).

Turbulence is an inherent property of medium and high Reynolds number flows, where the energy of the large flow structures is transferred in a cascade of scales towards the smallest vortices, where the turbulent kinetic energy dissipates into heat.
For numerical modeling of turbulent flow, three approaches are commonly used in CFD:

1. Direct Numerical Simulations (DNS), i.e. straightforward discretization of the Navier-Stokes equations on a sufficiently fine computational mesh, where all turbulent scales up to the smallest dissipating vortices are resolved. Even for moderate Reynolds numbers encountered in laryngeal airflow, this type of simulation is prohibitively expensive in terms of computational requirements. Sometimes, the term "laminar simulation" is incorrectly used for a DNS of flow using a coarse mesh. The term is correct for purely laminar flow with no turbulence. However, using the "laminar model" for turbulent flow is actually a

DNS on a coarse grid unable to capture the small-scale fluid motions, which introduces error since the influence of the subgrid-scale vortices on the large-scale (resolved) turbulent motions is neglected.

2. Unsteady Reynolds-Averaged Navier-Stokes equations (RANS) is the current industry standard, which completely gives up to resolve the turbulent fluctuations and dynamic evolution of vortical structures and aims to calculate the mean, time-averaged flow. The influence of turbulence on the mean flow is modeled using some of the plethora of more or less complex turbulence models. Clearly, RANS is unsuitable for aeroacoustic simulations of voice where the unsteady turbulent motions represent a crucial portion of the aeroacoustic sources.

   With rigorous DNS being infeasible and RANS inapplicable, numerical modeling of the aeroacoustic principles of voice production can use laminar simulations (de Oliviera Rosa et al., 2003; Alipour and Scherer, 2004; Bae and Moon, 2008; Larsson and Müller, 2009; Link et al., 2009; Thomson, 2015; Šidlof et al., 2015; Jiang et al., 2017; Sváček and Horáček, 2018).

3. The third arguably most promising approach is the large-eddy simulation (LES). LES may be regarded as a compromise between RANS, where the entire effect of turbulence is modeled, and DNS, where all the turbulent scales are resolved. The LES concept resolves the large, anisotropic energy-carrying fluid motions and models the effect of largely isotropic subgrid-scale turbulent structures. These large-scale simulations are still computationally expensive, especially if the boundary layer is to be resolved properly. However, current parallel computational resources make this approach viable for low and moderate Reynolds-number flows. In the numerical simulation of human phonation, the LES approach has been used in recent years. One of the first studies was the work of Suh and Frankel (2007), who used compressible LES and Ffowcs Williams-Hawkings acoustic analogy in a static model of human glottis for far-field sound predictions. Mihaescu et al. (2010, 2011) employed the LES capability of ANSYS Fluent (ANSYS, Canonsburg, PA/USA) to study the laryngeal airflow both during phonation and inspiration. The work of Schwarze et al. (2011) explores a variant called Implicit LES, where the intrinsic dissipation of the numerical method is assumed to act as a subgrid-scale model. Another compressible LES simulation on a static glottis was published by de Luzan et al. (2015). Recently, Sadeghi (Sadeghi et al., 2019c,a,b) simulated the laryngeal flow and effect of ventricular folds using the LES feature of STAR-CCM+ (Siemens PLM Software, Plano, TX/USA) and quantified the computational requirements on parallel architectures. In the study by Schickhofer et al. (2019), the same software and similar numerical approach was used to study the influence of the supraglottal coherent structures produced by flow through the static glottis on the far-field sound signal on a realistic vocal tract geometry from MRI-based data.

### 1.4.2 Modeling of the vocal fold structure and FSI simulations

*Lumped-parameter models* are based on lumped elements, such as masses, dampers and springs. From the point of view of kinematics, two-mass models cannot reproduce sagittal phase difference of the vocal fold displacement precisely and multi-mass models

also cannot control this phase difference in a direct way. The model published by Drioli and Aichinger (2021) allows to control sagittal phase difference by enabling a phase delay between oscillations at posterior and anterior parts of the vocal fold edge. This kind of models of human phonation are deployed to study structural and vibratory asymmetries, simulating vocal folds paralysis, jitter etc. Studies of complex effects, such as impact stress in fully closed vocal folds, was published by Horáček et al. (2007), concluding that the higher vocal fold loading is proportional to higher impact stress. An increase of fundamental frequency $f_o$ does not raise maximum impact stress and decrease the maximum amplitude of vibration (due to higher stiffness of the vocal folds margins).

*Continuous models.* Full fluid-structure interaction with complete structural mechanics were simulated in many studies in 2D (Luo et al., 2008; Link et al., 2009; Hájek et al., 2016), and 3D (Xue et al., 2014b; Jo et al., 2016), and special studies with pathological changes, such as tension imbalance caused by unilateral paralysis of vocal folds (Xue et al., 2014a), or the 2D model simulating a subglottal stenosis (Smith and Thomson, 2013). The subglottal stenosis occurs when the airway within the subglottal region or upper trachea is critically narrowed, often as a consequence of damage after endotracheal intubation and/or tracheotomy. In the glottic stenosis study is mentioned that disturbances in subglottal flow are already evident at 60% stenosis and increase with stenosis severity. More precisely, the disturbed flow contains on the stenosis side increased shear stress, decreased pressure, increased velocities and presence of vortices during respiration. The presence of turbulent structures in glottal flow contributes to hoarseness or breathiness in the voice (Grisel et al., 2010). Other models focusing on fluid-structure interactions take into account the morphological structure of the vocal fold cover, where computational models have more layers with different material properties (Smith and Thomson, 2012; Pickup and Thomson, 2011) since the vocal fold tissue has an anisotropic and inhomogeneous morphology (Titze and Alipour, 2006). More about nonlinear viscoelastic and hyperelastic layers is in Mittal et al. (2013).

### 1.4.3 CAA simulations

Voice generation is governed by a three-way interaction between the structure, airflow, and acoustics. The dominant aeroacoustic sound sources are located within the glottis and the supraglottal region, whereas sound sources below the glottis are not observed. Three characteristics of flow-induced sound are defined in terms of free-field radiation: First, vocal fold oscillation induces a monopole radiation pattern. Second, the interaction of the vocal folds and the air jet creates surface pressure fluctuations that radiate like a dipole. Third, the turbulent structures located downstream of the glottal constriction have a quadrupolar radiation pattern (Zhao et al., 2002; Zhang et al., 2002b). The sound due to the turbulent flow has a significant influence on the broadband noise at higher frequencies. The possibilities of how to get sound sources from tracheal flow and how to solve wave propagation are in general three:

1. Acoustic analogies: The compressible Navier-Stokes equation is transformed into an exact inhomogeneous wave equation (Lighthill, 1952)-(Lighthill, 1954). His general wave equation achieved very reasonable results, especially for cases with a low Mach number. In the following years, Lighthill proposed an equation for the free radiation

field using Green's function. The equations developed by Lighthill do not respect solid boundaries (reflection, absorption). The mentioned limit has been replaced by Curle (1955), who defined the static surfaces as a surface dipole distribution. The computation of noise radiation in cases including moving boundaries based on Kirchhoff's formula has been presented by Ffowcs Williams and Hawkings (1969).

2. Direct noise computation, i.e. computing all vortical $\mathcal{O}(u^8/c_0^5)$ and acoustic $\mathcal{O}(u^6/c_0^3)$ scales. Since the disparity of scales is enormous and this method requires computing the acoustic and fluid dynamics as a single field, few studies were published, e.g. the study of a turbulent jet, which validates an acoustic analogy (Freund et al., 2000). Recently, direct noise computations have been attempted by the Lattice-Boltzman very large-eddy simulation (LB-VLES) method. The lattice Boltzman method uses generalized Navier-Stokes equations at the microscopic level; it allows computing a flow field bounded by very complex geometries. The low dissipation and dispersion numerical scheme are also beneficial properties of the lattice Boltzman method compared to aeroacoustic results obtained by a high-order large-eddy simulation, presented by Marié et al. (2009). The method has reached good results in far-field pressure spectra also in cases with a high Reynolds number (10.5M), e.g. in the aircraft industry (landing gears), published by Fares et al. (2016) and Sanders et al. (2016).

3. Decomposition of the flow field. The main idea of this approach is hidden in the decomposition of the physical field into the temporal mean and a fluctuating component of field variables (pressure, density, and velocity). The fluctuations are further decomposed into an aerodynamic and acoustic component (based on Helmholtz decomposition). In contrast to the Lighthill analogy, the fluctuating component is further decomposed into the incompressible and acoustic ones. Last studies of the human voice are based on the Perturbed Convective Wave Equation (PCWE) developed by Hüppe and Kaltenbacher (2015). The PCWE has been used with a success on aeroacoustic simulations of human phonation by their co-workers (Zörner et al., 2016; Schoder et al., 2019; Valášek et al., 2018; Lasota et al., 2021). In (Lasota et al., 2021) large-eddy simulations were used with a variety of subgrid-scale models implemented in the OpenFOAM C++ package. The investigation has brought enough evidence to prove significant influence of the SGS modeling on the aeroacoustic spectrum.

The simplifications, which were done in acoustic phonation models are related to vocal tract geometries. Many years were used simplified vocal tracts such as circular 3D geometries of cross-section based on magnetic resonance imagining (Story et al., 1996), or computed tomography (Sundberg and Rossing, 1987). After a comprehensive study published by Arnela et al. (2016b) comparing highly realistic MRI-based, elliptical and circular geometries of vocal tracts, it is concluded that usage of simplified vocal tracts can be limited only for frequencies lower than (4,000-5,000) Hz in terms of acoustic response. The bent vocal tracts also have a weak influence on a transfer function. Some formants are shifted to lower frequencies, but not more than 5%. The cross-sectional shape affects formants less than 3% in comparison to circular and realistic vocal tract shapes. Other resonating parts such as lips have a negligible or minor impact on the transfer function (Arnela et al., 2016a), but teeth have become a subject of interest. The relevance of

teeth in computational models is dependent on oral configuration, resonant frequencies are changed with a presence of teeth, but very slightly, instead of models with side cavities and side branches, where the effect is really significant (up to the fifth formant, except the first). This occurs during high-pitched singing, or phonating an open back vowel /ɑ/. Traser et al. (2017) sheds light on resonance parts of the human respiratory tract, which could be ignored in numerical models. Hence vocal tract replicas from MRI are smoothed and averaged to a uniform model of the vocal tract, published by Probst et al. (2019), neglecting details such as lips (influence on the first formant is not relevant (Arnela et al., 2013)) and teeth (are not resolved by a standard MRI). More complex realistic vocal tracts from MRI are rather used in laboratory experiments, where the tracts are printed from silicone and mounted on a mass flow generator with a supercritical valve and silencer (Kniesburges et al., 2013; Lodermeyer et al., 2015).

## 1.5 Summary

Interdisciplinary topics combining medical application (treatment) and mathematical (or physical) modeling are increasingly common. Thereby, numerical simulations undoubtedly have strong potential to be applied in clinical routine (diagnostics, treatment control, etc.) because the computer analysis can provide 3D data of the flow and acoustic field, which are often not feasible by in-vivo, excised larynx or synthetic vocal fold measurements (Döllinger et al., 2011; Kniesburges et al., 2011). In lands where medical centers are struggling daily with voice diseases, it should be a high motivation to study the fundamentals of voice as a prevence for severe voice disease and medical costs.

## 1.6 Objectives of the thesis

This thesis builds on the work of the author's predecessors (Šidlof et al., 2015; Zörner et al., 2016). The main objectives of the thesis are as follows:

- To perform 3D large-eddy simulations of laryngeal airflow.
- To perform 3D aeroacoustic simulations of human phonation.
- To perform deep literature search and seek for recent less common subgrid-scale turbulence models, potentially suitable for laryngeal flow modeling.
- To implement such a new subgrid-scale model in OpenFOAM.
- To make a conclusion about the impact of using subgrid-scale turbulence models on human phonation modelling.

# 2 CFD model of incompressible laryngeal flow

## 2.1 Mathematical model

Large-eddy simulation is a mathematical concept for modeling turbulent flows, which deals with flow structures carrying most kinetic energy, i.e. spatially organized large scales. These consist of two main categories: coherent structures and coherent vortices of recognizable shape (Lesieur et al., 2005). In the numerical implementation, the characteristic length $\Delta$, defining a cutoff between resolved large scales and modeled subgrid scales, is usually given by the mesh grid spacing (Versteeg and Malalasekera, 2007).

In the LES concept, any flow variable $f(\mathbf{x}, t)$, where $\mathbf{x} = (x_1, x_2, x_3)$ is the spatial coordinate and $t$ time, may be decomposed as

$$f(\mathbf{x}, t) = \overline{f}(\mathbf{x}, t) + f'(\mathbf{x}, t), \tag{2.1}$$

where $\overline{f}(\mathbf{x}, t) = G_f(\mathbf{x}) * f(\mathbf{x}, t) = \int G_f(\mathbf{r}, \mathbf{x}, \Delta) f(\mathbf{x} - \mathbf{r}, t) \mathrm{d}\mathbf{r}$ is the large-scale component, obtained by spatial filtering, and $f'(x, t)$ is the small subgrid-scale contribution. Filtered variables for LES are functions of time and space, unlike the Reynolds averaged variables, hence in LES: $\overline{\overline{f}} \neq \overline{f}$, $\overline{f'} \neq 0$.

The convolution introduced above contains a filter function $G_f$ separating spatial scales. Commonly used filters are the top-hat filter (2.2), the Gaussian filter (2.3) and the spectral cut-off filter (2.4):

$$G_f(\mathbf{r}, \mathbf{x}, \Delta) = \begin{cases} 1/\Delta^3 & \text{for } |\mathbf{r}| \leq \Delta/2, \\ 0 & \text{otherwise,} \end{cases} \tag{2.2}$$

$$G_f(\mathbf{r}, \mathbf{x}, \Delta) = \left(\frac{6}{\pi \Delta^2}\right)^{1/2} \exp\left(-\frac{6|\mathbf{r}|^2}{\Delta^2}\right), \tag{2.3}$$

$$G_f(\mathbf{r}, \mathbf{x}, \Delta) = \prod_{i=1}^{3} \frac{\sin(r_i/\Delta)}{r_i}. \tag{2.4}$$

The top-hat filter is used in the current simulation, which is a common choice in low-order finite volume methods.

The effect of subgrid-scale (SGS) contributions on the large flow scales relies on the assumption of isotropic (non-directional) small-scale turbulence and is modeled. Compared to the Reynolds stresses in RANS, the SGS stresses carry much less of the turbulent energy, so the model's accuracy is less critical. The LES solution seeks to compute only the scales of motion larger or equal than the filter width $\Delta$.

The continuity and momentum equations for the incompressible fluid flow, with LES filtering applied, can be written as

$$\frac{\partial \overline{u}_i}{\partial x_i} = 0, \tag{2.5}$$

$$\frac{\partial \overline{u}_i}{\partial t} + \frac{\partial}{\partial x_j}(\overline{u_i u_j}) = -\frac{1}{\rho}\frac{\partial \overline{p}}{\partial x_i} + \nu \frac{\partial^2 \overline{u}_i}{\partial x_j \partial x_j}, \tag{2.6}$$

where $\overline{u}_i$ is the filtered velocity, $\overline{p}$ represents the filtered static pressure and $\nu$ is the kinematic molecular viscosity. The term $\overline{u_i u_j}$ is the dyadic product and cannot be expressed directly (Ferziger, 1998). Modification of the momentum equation (2.6) by $+\frac{\partial}{\partial x_j}(\overline{u}_i \overline{u}_j)$ yields

$$\frac{\partial \overline{u}_i}{\partial t} + \frac{\partial}{\partial x_j}(\overline{u}_i \overline{u}_j) = -\frac{1}{\rho}\frac{\partial \overline{p}}{\partial x_i} + \nu \frac{\partial^2 \overline{u}_i}{\partial x_j \partial x_j} - \frac{\partial \tau_{ij}}{\partial x_j}. \tag{2.7}$$

The new term on the right-hand side of (2.7) is the divergence of the subgrid-scale (SGS) turbulent stress tensor

$$\tau_{ij} = \overline{u_i u_j} - \overline{u}_i \overline{u}_j = -(\overline{u_i' u_j'} + \overline{\overline{u}_i u_j'} + \overline{u_i' \overline{u}_j} + \overline{\overline{u}_i \overline{u}_j} - \overline{u}_i \overline{u}_j), \tag{2.8}$$

where the individual tensors are: $-\overline{u_i' u_j'}$ the Reynolds-stress-like term, $-(\overline{\overline{u}_i u_j'} + \overline{u_i' \overline{u}_j})$ the Clark term (Clark et al., 1979) and $-(\overline{\overline{u}_i\, \overline{u}_j} + \overline{u}_i \overline{u}_j)$ the Leonard term (Leonard, 1975). The SGS stress tensor $\tau_{ij}$ is left to be modeled to close the set of equations.

Since the turbulence is not fully understood, a wide range of closure models have been introduced, often using heuristic and ad hoc techniques.

### 2.1.1 Smagorinsky SGS model

One of the first and simplest subgrid-scale closure models was the Smagorinsky algebraic model (Smagorinsky, 1963), based on the eddy-viscosity assumption

$$\tau_{ij} - \frac{1}{3}\tau_{kk}\delta_{ij} = -2\nu_t \overline{S}_{ij} = -\nu_t \left( \frac{\partial \overline{u}_i}{\partial x_j} + \frac{\partial \overline{u}_j}{\partial x_i} \right). \tag{2.9}$$

which states that the deviatoric part of the SGS stress tensor ($\operatorname{dev}\tau = \tau_{ij} - \frac{1}{3}\tau_{kk}\delta_{ij}$) is proportional to the rate-of-strain tensor $\overline{S}_{ij} = \operatorname{symm}(\nabla \overline{\mathbf{u}})$. The operators dev() and symm() are described in (A.9) and (A.6), respectively.
The constant of proportionality in this relation, $\nu_t$, is called the kinematic subgrid-scale eddy-viscosity (or just turbulent viscosity), which eventually adds to the kinematic molecular viscosity $\nu$. The Smagorinsky model assumes that the small scales dissipate instantaneously all energy transferred from the resolved scales. From this, Smagorinsky derived that the SGS viscosity may be estimated as

$$\nu_t^S = (C_S \Delta)^2 \sqrt{2\overline{S}_{ij}\overline{S}_{ij}} = (C_S \Delta)^2 |\overline{\mathbb{S}}|, \tag{2.10}$$

where $C_S \approx 0.18$ is the Smagorinsky constant describing the rate of the break-up of isotropic vortices in the viscous subrange of the turbulence energy spectrum, and where $|\overline{\mathbb{S}}|$ is the magnitude of the strain rate tensor (see A.11). The rotation-rate tensor $\overline{\Omega}_{ij}$, the antisymmetric part of the velocity gradient tensor, is not taken into account. Eq. (2.10) can be rewritten using the second invariant of the strain-rate tensor $II_{\overline{\mathbb{S}}} = \frac{1}{2}\operatorname{tr}(\overline{\mathbb{S}}^2)$ into the form

$$\nu_t^S = (C_S \Delta)^2 \sqrt{4 II_{\overline{\mathbb{S}}}}. \tag{2.11}$$

The main limitation of the Smagorinsky model lies in the assumption of local equilibrium between the production and dissipation of turbulent SGS energy. This assumption is not fulfilled in many real cases. Notably, free shear layer flows, separating and reattaching flows, and wall-dominated flows (which is also the case of glottal airflow). This is why more accurate SGS models have been tested in our study, as described in the following sections.

The numerical simulations used in this thesis were performed in the OpenFOAM package, which uses slightly different notations of quantities, e.g. $\overline{\mathbb{D}}$ is used in place of $\overline{\mathbb{S}}$. Implementation of the Smagorinsky model will be shown in following lines. The model comes from the assumption of local equilibrium

$$\underbrace{\overline{\mathbb{D}} : \tau}_{\text{SGS energy production}} + \underbrace{C_\epsilon \frac{k_{SGS}^{1.5}}{\Delta}}_{\text{dissipation}} = 0, \tag{2.12}$$

where the double dot scalar product between the strain-rate and subgrid-scale stress tensors represents the production of subgrid-scale energy; the second term on the left side is a dissipation of subgrid scales, where $k_{SGS}$ is the subgrid-scale turbulent energy, $\Delta$ the grid element size and $C_\epsilon$ a model constant. The subgrid-scale stress tensor $\tau$ in (2.12) can be substituted as follows

$$\overline{\mathbb{D}} : \left( \frac{2}{3} k_{SGS} \, \mathbb{I} - 2\nu_t^S \, \operatorname{dev} \overline{\mathbb{D}} \right) + C_\epsilon \frac{k_{SGS}^{1.5}}{\Delta} = 0. \tag{2.13}$$

To obtain the approximation of $k_{SGS}$ a series of modifications on (2.13) has to be done, leading to following equation

$$\overline{\mathbb{D}} : \left( \frac{2}{3} k_{SGS} \, \mathbb{I} - 2C_k \Delta \sqrt{k_{SGS}} \, \operatorname{dev} \overline{\mathbb{D}} \right) + C_\epsilon \frac{k_{SGS}^{1.5}}{\Delta} = 0. \tag{2.14}$$

And by modifying (2.14) the following form is achieved

$$\sqrt{k_{SGS}} \left( \underbrace{\frac{C_\epsilon}{\Delta}}_{\text{a}} k_{SGS} + \underbrace{\frac{2}{3} \operatorname{tr} \overline{\mathbb{D}}}_{\text{b=0}} \sqrt{k_{SGS}} - \underbrace{2C_k \Delta \left( \operatorname{dev} \overline{\mathbb{D}} : \overline{\mathbb{D}} \right)}_{\text{c}=C_k \Delta |\overline{\mathbb{D}}|^2} \right) = 0. \tag{2.15}$$

Thereby, (2.15) can be simplified into

$$a k_{SGS} - c = 0, \tag{2.16}$$

where the variable $b$ is zero for incompressible cases. Therefore the subgrid scale energy is computed from

$$k_{SGS} = \frac{c}{a} = \frac{C_k \Delta^2 |\overline{\mathbb{D}}|^2}{C_\epsilon}, \tag{2.17}$$

where

$$|\overline{\mathbb{D}}|^2 = 2 \overline{D}_{ij} \overline{D}_{ij}, \tag{2.18}$$

corresponding to the magnitude-squared of the tensor field (see A.12).

The subgrid scale viscosity computed by the Smagorinsky model is implemented as

$$\nu_t^S = C_k \Delta \sqrt{k_{SGS}} = C_k \Delta^2 \sqrt{\frac{C_k}{C_\epsilon}} |\overline{\mathbb{D}}|. \tag{2.19}$$

The modelling of $\nu_t^S$ depends on the length $\Delta$ of the user-chosen filter and model constants. The static value of the Smagorinsky model constant $C_S$ was found to cause excessive damping of large-scale fluctuations in cases with homogeneous isotropic turbulence (Germano et al., 1991). A priori tests provided by Mcmillan et al. (1980) confirmed a correlation that the Smagorinsky model constant decreases with increasing strain rate. From a practical point of view, Mason and Callen (1986) have found that $C_S = 0.2$ and fine mesh refinement were in a good agreement with experiments, whereas in cases with coarse mesh, they recommended $C_S < 0.2$. This is in direct contradiction with the study published by Piomelli et al. (1988), where the boundary layer is resolved with optimal value $y^+ = 0.1$. Piomelli used damping functions for ensuring asymptotic behavior for the SGS shear stresses near walls. Smagorinsky model cannot account for energy flow from small-scales to large-scales (known as backscatter).

To summarize, the Smagorinsky model gives acceptable results in simulations of decaying homogeneous isotropic turbulence (Rozema et al., 2015), but due to high eddy dissipation for laminar and transitional flows, the model causes wrong predictions of shear stress at walls, which delays the transition to turbulence. The classical Smagorinsky model fails in practical LES simulations. Unlike the static Smagorinsky SGS model, the dynamic procedure of the Smagorinsky coefficient published by Germano et al. (1991) has a slight computational cost augmentation, caused by local computation of the model coefficients the model coefficients locally, but the model determines the Smagorinsky coefficient $C_S$ by comparing the eddy dissipation at two filter levels. Therefore the model gives a correct level of eddy dissipation and switches off for laminar or transitional flow regime (Meneveau and Katz, 2000).

### 2.1.2 One-equation SGS model

The one-equation eddy-viscosity subgrid-scale model (or also k-equation) tries to address the deficiency of the model of Smagorinsky by solving an additional transport equation. Yoshizawa and Horiuti (1985) derived the transport equation for the turbulent kinetic SGS energy $k_{SGS}$ in the form

$$\frac{\partial k_{SGS}}{\partial t} + \frac{\partial \overline{u}_j k_{SGS}}{\partial x_j} - \frac{\partial}{\partial x_j}\left[(\nu + \nu_t)\frac{\partial k_{SGS}}{\partial x_j}\right] = -\tau_{ij}\overline{S}_{ij} - C_\epsilon \frac{k_{SGS}^{3/2}}{\Delta}, \tag{2.20}$$

where the terms represent the temporal change, convection, diffusion, production and rate of dissipation. Unlike the Smagorinsky model, which disregards the first three of these, the one-equation model takes into account also the history effects for $k_{SGS}$. The production term, modeling the decay of turbulence from the resolved scales to the SGS scales via the energy cascade, is approximated by

$$-\tau_{ij}\overline{S}_{ij} = 2\nu_t \overline{S}_{ij}\overline{S}_{ij}, \tag{2.21}$$

where the double inner product of two second-rank tensors (on both sides) is a sum of nine components, and the product is a scalar value (see A.1).

The model constant in (2.20) is set to $C_\epsilon = 1.048$, where

$$C_\epsilon = \pi \left( \frac{3C_\nu}{2} \right)^{-3/2}, \tag{2.22}$$

and where $C_\nu = 0.094$ due to the Kolmogorov law with the dissipation rate $\epsilon$

$$k_{SGS} = \left( \frac{3}{2} \right) C_\nu \left( \frac{\Delta\epsilon}{\pi} \right)^{3/2}. \tag{2.23}$$

The one-equation model relies on the SGS eddy viscosity concept with the SGS viscosity

$$\nu_t^O = C_\nu \Delta \sqrt{k_{SGS}}. \tag{2.24}$$

Both the Smagorinsky and One-Equation models cannot reproduce the laminar to turbulent transition and tend to overpredict the production rate and thus the turbulent viscosity in free shear layers and near the walls. This is caused by the fact that the term $\overline{S}_{ij}\overline{S}_{ij}$ is large in the regions of pure shear because it is only related to the rate-of-strain $\overline{S}_{ij}$, not to the rate-of-rotation $\overline{\Omega}_{ij}$ (Lesieur et al., 2005).

### 2.1.3 WALE SGS model

The inaccuracy concerning free shear and boundary layer treatment, caused by the previously described SGS models, can be alleviated by using the Wall-Adapting Local Eddy-viscosity (WALE) model (Nicoud and Ducros, 1999). The Smagorinsky model is based on the second invariant of $S_{ij}$, which means a missing relation with the rate-of-rotation tensor $\Omega_{ij}$. The WALE model considers the traceless symmetric part of the square of the velocity gradient $s_{ij}^d$ written as

$$\begin{aligned} s_{ij}^d &= \frac{1}{2}(\overline{G}_{ij}^2 + \overline{G}_{ji}^2) - \frac{1}{3}\delta_{ij}\overline{G}_{kk}^2 = \\ &= \frac{1}{2}\left( \frac{\partial \overline{u}_i}{\partial x_k}\frac{\partial \overline{u}_k}{\partial x_j} + \frac{\partial \overline{u}_j}{\partial x_k}\frac{\partial \overline{u}_k}{\partial x_i} \right) - \frac{1}{3}\delta_{ij}\frac{\partial \overline{u}_k}{\partial x_k}\frac{\partial \overline{u}_k}{\partial x_k}, \end{aligned} \tag{2.25}$$

where $\overline{G}_{ij}^2 = \overline{G}_{ik}\overline{G}_{kj}$, $\overline{G}_{ij} = \partial \overline{u}_i / \partial x_j$ is the filtered velocity gradient tensor, $\delta_{ij}$ is the Kronecker symbol. The WALE and the following model (AMD) will be presented in codes, but it should be noted that only the AMD model was implemented by the author. The term $s_{ij}^d$ is implemented on line 7 of the following code

```
1 template<class BasicTurbulenceModel>
2 tmp<volSymmTensorField> WALE<BasicTurbulenceModel>::Sd
3 (
4     const volTensorField& gradU
5 ) const
6 {
7     return dev(symm(gradU & gradU));
8 }
```

See A.1 for explanations of used functions.

The term in (2.25) can be rewritten with the symmetric part and the deviatoric part of the velocity gradient

$$s_{ij}^d = \overline{S}_{ik}\,\overline{S}_{kj} + \overline{\Omega}_{ik}\,\overline{\Omega}_{kj} - \frac{1}{3}\delta_{ij}[\overline{S}_{mn}\,\overline{S}_{mn} - \overline{\Omega}_{mn}\,\overline{\Omega}_{mn}], \tag{2.26}$$

where the terms are rate-of-strain

$$\overline{S}_{ij} = \frac{1}{2}(\overline{g}_{ij} + \overline{g}_{ij}^{\top}) \tag{2.27}$$

and rate-of-rotation

$$\overline{\Omega}_{ij} = \frac{1}{2}(\overline{g}_{ij} - \overline{g}_{ij}^{\top}) \tag{2.28}$$

tensors. The trace of (2.26) is zero and the second invariant is proportional to $s_{ij}^d s_{ij}^d$, that is

$$s_{ij}^d s_{ij}^d = \frac{1}{6}(\mathbb{S}^2\mathbb{S}^2 + \Omega^2\Omega^2) + \frac{2}{3}\mathbb{S}^2\Omega^2 + 2IV_{\mathbb{S}\Omega}, \tag{2.29}$$

where $\mathbb{S}^2 = \overline{S}_{ij}\overline{S}_{ij}$, $\Omega^2 = \overline{\Omega}_{ij}\overline{\Omega}_{ij}$ and the fourth invariant

$$IV_{\mathbb{S}\Omega} = \mathrm{tr}(\overline{S}_{ij}\overline{\Omega}_{ij}^2) = \overline{S}_{ik}\,\overline{S}_{kj}\,\overline{\Omega}_{jl}\,\overline{\Omega}_{li} \tag{2.30}$$

is used. The term (2.29) is able to detect turbulent structures with strain, or rotation rate, or even both. Regarding to this behavior, the pure shear flow located near solid boundaries during laminar flow will cause that the eddy-viscosity vanishes (Nicoud and Ducros, 1999).

The turbulent viscosity computed by the WALE model is defined as

$$\nu_t^W = C_k \Delta \sqrt{k_{SGS}^W}, \tag{2.31}$$

which refers to the code line 4

```
1 template<class BasicTurbulenceModel>
2 void WALE<BasicTurbulenceModel>::correctNut()
3 {
4     this->nut_ = Ck_*this->delta()*sqrt(this->k(fvc::grad(this->U_)));
5     this->nut_.correctBoundaryConditions();
6     fv::options::New(this->mesh_).correct(this->nut_);
7
8     BasicTurbulenceModel::correctNut();
9 }
```

where the term $k_{SGS}^W$ is computed by

$$k_{SGS}^W = \left(\frac{C_w^2\Delta}{C_k}\right)^2 \frac{(s_{ij}^d s_{ij}^d)^3}{\left((\overline{S}_{ij}\,\overline{S}_{ij})^{5/2} + (s_{ij}^d s_{ij}^d)^{5/4}\right)^2} \tag{2.32}$$

corresponding with code lines 12-20

```
1  template<class BasicTurbulenceModel>
2  tmp<volScalarField> WALE<BasicTurbulenceModel>::k
3  (
4      const volTensorField& gradU
5  ) const
6  {
7      volScalarField magSqrSd(magSqr(Sd(gradU)));
8
9      return volScalarField::New
10     (
11         IOobject::groupName("k", this->alphaRhoPhi_.group()),
12         sqr(sqr(Cw_)*this->delta()/Ck_)*
13         (
14             pow3(magSqrSd)
15            /(
16                sqr
17                (
18                    pow(magSqr(symm(gradU)), 5.0/2.0)
19                  + pow(magSqrSd, 5.0/4.0)
20                )
21              + dimensionedScalar
22                (
23                    "small",
24                    dimensionSet(0, 0, -10, 0, 0),
25                    small
26                )
27            )
28        )
29    );
30 }
```

The model constants are set to $C_w = 0.325$ and $C_k = 0.094$. The way how to determine $C_w$ is to make the assumption that the model gives the same ensemble-average subgrid kinetic energy dissipation as the classical Smagorinsky model (Nicoud and Ducros, 1999), which means

$$C_w^2 = C_S^2 \frac{\left\langle \sqrt{2}(\overline{S}_{ij}\overline{S}_{ij})^{3/2} \right\rangle}{\left\langle \overline{S}_{ij}\overline{S}_{ij}(s_{ij}^d s_{ij}^d)^{3/2}\left((\overline{S}_{ij}\overline{S}_{ij})^{5/2} + (s_{ij}^d s_{ij}^d)^{5/4}\right)^{-1} \right\rangle} \tag{2.33}$$

respecting Smagorinsky constant $C_S \approx 0.18$. Thereby, the turbulent viscosity computed by WALE has the full form

$$\nu_t^W = (C_w \Delta)^2 \frac{(s_{ij}^d s_{ij}^d)^{3/2}}{(\overline{S}_{ij}\,\overline{S}_{ij})^{5/2} + (s_{ij}^d s_{ij}^d)^{5/4}}, \tag{2.34}$$

where the term $(s_{ij}^d s_{ij}^d)^{3/2}/(\overline{S}_{ij}\,\overline{S}_{ij})^{5/2}$ would not be well conditioned, because the denominator term can be zero for pure shear or rotational strain. The added term $(s_{ij}^d s_{ij}^d)^{5/4}$ keeps the turbulent viscosity finite.

In summary, the WALE algebraic model formulation accounts for the rotational rate in the computation of $\nu_t^W$, and thus the turbulent viscosity tends to zero near walls. Hence it is not necessary to use any *ad hoc* damping methods.

### 2.1.4 AMD SGS model

The anisotropic minimum-dissipation (AMD) subgrid-scale model was derived by Rozema et al. (2015) with modified Poincaré inequality addressing the grid anisotropy. The AMD model has not yet been applied in numerical simulation of human phonation, and thus the model was chosen as a candidate to new implementation performed by the author of this thesis into the OpenFOAM CFD package.

AMD is developed from the QR model (Verstappen, 2011), and both models are in the category "minimum-dissipation models". The main objective of these models is to ensure that the energy of subgrid scales is not increasing

$$\partial_t \int_{\Omega_\delta} \frac{1}{2} u_i' u_i' \mathrm{d}x \leq 0. \tag{2.35}$$

In the situation where subgrid scales are assumed to be periodical on filter box $\Omega_\delta$, it is possible to apply the Poincaré inequality, and define thus the upper bound of the SGS energy on the left side

$$\int_{\Omega_\delta} \frac{1}{2} u_i' u_i' \mathrm{d}x \leq C_A \int_{\Omega_\delta} \frac{1}{2} (\partial_i u_j)(\partial_i u_j) \mathrm{d}x. \tag{2.36}$$

The right hand side corresponds to the velocity gradient energy, and $C_A$ is the Poincaré constant

$$C_A = (\delta/\pi)^2 \tag{2.37}$$

for the LES filter of width $\delta$. The evolution of the right hand side in (2.36) can be written, considering Taylor expansion of the exact subgrid-scale tensor, as

$$\partial_t \left( \frac{1}{2} (\partial_i u_j)(\partial_i u_j) \right) = \overbrace{-(\partial_k u_i)(\partial_k u_j) S_{ij}}^{R1} - (\partial_k S_{ij}) \partial_k (2\nu S_{ij}) - (\partial_k S_{ij}) \partial_k (2\nu_t^{QR} S_{ij}) + \partial_i f_i, \tag{2.38}$$

where $f_i$ is the flux of velocity gradient energy and $\nu_t^{QR}$ is the turbulent viscosity defined by the QR model. Upon spatial integration over the LES filter, the divergence term $\partial_i f_i$ can be rewritten to a boundary integral. The boundary integrals express transport of velocity gradient energy instead of production or dissipation and thus can be ignored in the derivation of minimum-dissipation models (Rozema et al., 2015). The term $R1$ from (2.38) is the production of the velocity gradient energy and can be rewritten to

$$-(\partial_k u_i)(\partial_k u_j) S_{ij} = 4 III_{\mathbb{S}} + \boldsymbol{\nabla} \cdot (...), \tag{2.39}$$

having the important third invariant of the resolved strain-rate tensor

$$III_{\mathbb{S}} = -\det \mathbb{S} = -\frac{1}{3} \mathrm{tr}(\mathbb{S}^3) = -\frac{1}{3} S_{ij} S_{jk} S_{ki}. \tag{2.40}$$

The dissipation rate of the velocity gradient energy is

$$\int_{\Omega_\delta} 2 II_{\mathbb{S}} \, \mathrm{d}x = \int_{\Omega_\delta} S_{ij} S_{ij} \mathrm{d}x \leq C_\delta \int_{\Omega_\delta} (\partial_k S_{ij})(\partial_k S_{ij}) \mathrm{d}x, \tag{2.41}$$

where the second invariant is

$$II_{\mathbb{S}} = \frac{1}{2}\mathrm{tr}(\mathbb{S}^2) = \frac{1}{2}S_{ij}S_{ij}. \tag{2.42}$$

Finally, the condition which is necessary for the eddy disipation to stop the production of the velocity gradient energy is in the form

$$4\int_{\Omega_\delta} III_{\mathbb{S}}\ \mathrm{d}x \leq 4\frac{\nu_t^{QR}}{C_A}\int_{\Omega_\delta} II_{\mathbb{S}}\ \mathrm{d}x. \tag{2.43}$$

The minimum eddy dissipation is thus equal to

$$\nu_t^{QR} = C_A\delta^2\frac{\max\{III_{\mathbb{S}}, 0\}}{II_{\mathbb{S}}}, \tag{2.44}$$

where $C_A$ is a model constant. The third invariant $III_{\mathbb{S}}$ vanishes in flows that are laminar (Vreman, 2004). To summarize:

- The production term in (2.38) is proportional to the dissipation of the leading term on the right-hand side in (2.39).
- The dissipation of the energy of subgrid-scales is proportional to $III_{\mathbb{S}}$.
- The QR model is consistent with the eddy dissipation of the exact subgrid-scale tensor.

The main drawback of the QR model is necessity to set a filter width $\delta$ and applicability on isotropic grids only.

The AMD model can sidestep the dependence of model constants on the filter width by using the modified Poincaré inequality

$$\int_{\Omega_\delta}\frac{1}{2}u_i'u_i'\mathrm{d}x \leq C_A\int_{\Omega_\delta}\overbrace{\frac{1}{2}(\underbrace{\delta x_i\partial_i}_{R3}u_j)(\delta x_i\partial_i u_j)}^{R2}\,\mathrm{d}x, \tag{2.45}$$

where $\Omega_\delta$ is the filter box, having dimensions $\delta x_1$, $\delta x_2$ and $\delta x_3$, and $C_A$ is a model constant, which will be discussed later. The term $R2$ is the scaled velocity gradient energy, $R3$ the scaled gradient operator. The inequality (2.45) demonstrates that the subgrid energy is confined by imposing a bound on the term $R2$ (Rozema et al., 2015). Time derivative is applied on the term $R2$ and the evolution equation of $R2$ on the filter box $\delta x_i$ is expressed

$$\begin{aligned}\partial_t\left(\frac{1}{2}(\delta x_i\partial_i u_j)(\delta x_i\partial_i u_j\right) = &\overbrace{-(\delta x_k\partial_k u_i)(\delta x_k\partial_k u_j)S_{ij}}^{R4} - \\ &-(\nu+\nu_t^A)\delta x_k\partial_k(\partial_i u_j)\delta x_k\partial_k(\partial_i u_j) + \partial_i f_i,\end{aligned} \tag{2.46}$$

where the term $R4$ is the production of the scaled velocity gradient energy. This means the third invariant is not computed from the resolved strain-rate tensor $S_{ij}$, such as in the QR model (2.40), and for the second invariant in (2.42).

The following inequality ensures that the AMD model predicts sufficient dissipation to stop the production of scaled velocity gradient energy $R4$

$$\int_{\Omega_\delta} -(\delta x_k \partial_k u_i)(\delta x_k \partial_k u_j) S_{ij} \mathrm{d}x \leq \frac{\nu_t^A}{C_A} \int_{\Omega_\delta} (\partial_i u_j)(\partial_i u_j) \mathrm{d}x, \tag{2.47}$$

where the minimum dissipation effect is held by satisfying

$$\nu_t^A = C_A \frac{\max\{\int_{\Omega_\delta} -(\delta x_k \partial_k u_i)(\delta x_k \partial_k u_j) S_{ij} \mathrm{d}x, 0\}}{\int_{\Omega_\delta} (\partial_l u_m)(\partial_l u_m) \mathrm{d}x}. \tag{2.48}$$

Integrals in (2.48) can be approximated by the mid-point rule, and the turbulent viscosity from AMD $\nu_t^A$ results in a more practical form

$$\nu_t^A = C_A \frac{\overbrace{\max\{\overbrace{-(\delta x_k \partial_k u_i)(\delta x_k \partial_k u_j) S_{ij}}^{-A_{ij}S_{ij}}, 0\}}^{n_-}}{\underbrace{(\partial_l u_m)(\partial_l u_m)}_{d_-}}. \tag{2.49}$$

The terms $-A_{ij}S_{ij}$ and $d_-$ are written as

$$\begin{aligned}
A_{ij}S_{ij} &= (\delta x_k \partial_k u_i)(\delta x_k \partial_k u_j) S_{ij} = \\
&= \sum_{i,j=1}^{3} \left(\delta x_1 \frac{\partial u_i}{\partial x_1} + \delta x_2 \frac{\partial u_i}{\partial x_2} + \delta x_3 \frac{\partial u_i}{\partial x_3}\right)\left(\delta x_1 \frac{\partial u_i}{\partial x_1} + \delta x_2 \frac{\partial u_i}{\partial x_2} + \delta x_3 \frac{\partial u_i}{\partial x_3}\right) S_{ij} = \\
&= S_{11}\left(\delta x_1 \frac{\partial u_1}{\partial x_1} + \delta x_2 \frac{\partial u_1}{\partial x_2} + \delta x_3 \frac{\partial u_1}{\partial x_3}\right)\left(\delta x_1 \frac{\partial u_1}{\partial x_1} + \delta x_2 \frac{\partial u_1}{\partial x_2} + \delta x_3 \frac{\partial u_1}{\partial x_3}\right) + \\
&+ S_{12}\left(\delta x_1 \frac{\partial u_1}{\partial x_1} + \delta x_2 \frac{\partial u_1}{\partial x_2} + \delta x_3 \frac{\partial u_1}{\partial x_3}\right)\left(\delta x_1 \frac{\partial u_2}{\partial x_1} + \delta x_2 \frac{\partial u_2}{\partial x_2} + \delta x_3 \frac{\partial u_2}{\partial x_3}\right) + \\
&+ S_{13}\left(\delta x_1 \frac{\partial u_1}{\partial x_1} + \delta x_2 \frac{\partial u_1}{\partial x_2} + \delta x_3 \frac{\partial u_1}{\partial x_3}\right)\left(\delta x_1 \frac{\partial u_3}{\partial x_1} + \delta x_2 \frac{\partial u_3}{\partial x_2} + \delta x_3 \frac{\partial u_3}{\partial x_3}\right) + \\
&+ S_{21}\left(\delta x_1 \frac{\partial u_2}{\partial x_1} + \delta x_2 \frac{\partial u_2}{\partial x_2} + \delta x_3 \frac{\partial u_2}{\partial x_3}\right)\left(\delta x_1 \frac{\partial u_1}{\partial x_1} + \delta x_2 \frac{\partial u_1}{\partial x_2} + \delta x_3 \frac{\partial u_1}{\partial x_3}\right) + \\
&+ S_{22}\left(\delta x_1 \frac{\partial u_2}{\partial x_1} + \delta x_2 \frac{\partial u_2}{\partial x_2} + \delta x_3 \frac{\partial u_2}{\partial x_3}\right)\left(\delta x_1 \frac{\partial u_2}{\partial x_1} + \delta x_2 \frac{\partial u_2}{\partial x_2} + \delta x_3 \frac{\partial u_2}{\partial x_3}\right) + \\
&+ S_{23}\left(\delta x_1 \frac{\partial u_2}{\partial x_1} + \delta x_2 \frac{\partial u_2}{\partial x_2} + \delta x_3 \frac{\partial u_2}{\partial x_3}\right)\left(\delta x_1 \frac{\partial u_3}{\partial x_1} + \delta x_2 \frac{\partial u_3}{\partial x_2} + \delta x_3 \frac{\partial u_3}{\partial x_3}\right) + \\
&+ S_{31}\left(\delta x_1 \frac{\partial u_3}{\partial x_1} + \delta x_2 \frac{\partial u_3}{\partial x_2} + \delta x_3 \frac{\partial u_3}{\partial x_3}\right)\left(\delta x_1 \frac{\partial u_1}{\partial x_1} + \delta x_2 \frac{\partial u_1}{\partial x_2} + \delta x_3 \frac{\partial u_1}{\partial x_3}\right) + \\
&+ S_{32}\left(\delta x_1 \frac{\partial u_3}{\partial x_1} + \delta x_2 \frac{\partial u_3}{\partial x_2} + \delta x_3 \frac{\partial u_3}{\partial x_3}\right)\left(\delta x_1 \frac{\partial u_2}{\partial x_1} + \delta x_2 \frac{\partial u_2}{\partial x_2} + \delta x_3 \frac{\partial u_2}{\partial x_3}\right) + \\
&+ S_{33}\left(\delta x_1 \frac{\partial u_3}{\partial x_1} + \delta x_2 \frac{\partial u_3}{\partial x_2} + \delta x_3 \frac{\partial u_3}{\partial x_3}\right)\left(\delta x_1 \frac{\partial u_3}{\partial x_1} + \delta x_2 \frac{\partial u_3}{\partial x_2} + \delta x_3 \frac{\partial u_3}{\partial x_3}\right)
\end{aligned} \tag{2.50}$$

and

$$
\begin{aligned}
d_{\_} &= (\partial_l u_m)(\partial_l u_m) = \\
&= \sum_{l,m=1}^{3} \left(\frac{\partial u_m}{\partial x_l}\right)\left(\frac{\partial u_m}{\partial x_l}\right) = \\
&= \left(\frac{\partial u_1}{\partial x_1}\right)\left(\frac{\partial u_1}{\partial x_1}\right) + \left(\frac{\partial u_2}{\partial x_1}\right)\left(\frac{\partial u_2}{\partial x_1}\right) + \left(\frac{\partial u_3}{\partial x_1}\right)\left(\frac{\partial u_3}{\partial x_1}\right) + \\
&+ \left(\frac{\partial u_1}{\partial x_2}\right)\left(\frac{\partial u_1}{\partial x_2}\right) + \left(\frac{\partial u_2}{\partial x_2}\right)\left(\frac{\partial u_2}{\partial x_2}\right) + \left(\frac{\partial u_3}{\partial x_2}\right)\left(\frac{\partial u_3}{\partial x_2}\right) + \\
&+ \left(\frac{\partial u_1}{\partial x_3}\right)\left(\frac{\partial u_1}{\partial x_3}\right) + \left(\frac{\partial u_2}{\partial x_3}\right)\left(\frac{\partial u_2}{\partial x_3}\right) + \left(\frac{\partial u_3}{\partial x_3}\right)\left(\frac{\partial u_3}{\partial x_3}\right) = \\
&= (\boldsymbol{\nabla}\mathbf{u}) : (\boldsymbol{\nabla}\mathbf{u}).
\end{aligned} \tag{2.51}
$$

The implementation of $-A_{ij}S_{ij}$ is shown on lines 10 and 13, the whole nominator $n_{\_}$ is on line 13, and the whole denominator $d_{\_}$ refers to line 14; implemented into OpenFOAM (version 6 and 7).

```
1  template<class BasicTurbulenceModel>
2  void LAAMD<BasicTurbulenceModel>::correct()
3  {
4      LESeddyViscosity<BasicTurbulenceModel>::correct();
5
6      const volVectorField& U = this->U_;
7      tmp<volTensorField> tgradU(fvc::grad(U));
8      const volTensorField& gradU = tgradU();
9      volSymmTensorField S(dev(symm(gradU())));
10     volTensorField Aij= (this->delta()*gradU)&(this->delta()*(gradU).T());
11     dimensionedScalar my_null_("my_null_",
12         dimensionSet(0,2,-3,0,0,0,0), scalar(0));
13     volScalarField n_ = max(-Aij && S,my_null_);
14     volScalarField d_ = gradU && gradU;
15
16     //scalar C_A_ = 0.57735;
17     nu_amd_ = (0.57735*n_)/d_;
18
19     correctNut();
20 }
21
22 template<class BasicTurbulenceModel>
23 void LAAMD<BasicTurbulenceModel>::correctNut()
24 {
25     volScalarField k(this->k(fvc::grad(this->U_)));
26
27     this->nut_ =nu_amd_;
28     this->nut_.correctBoundaryConditions();
29     fv::options::New(this->mesh_).correct(this->nut_);
30
31     BasicTurbulenceModel::correctNut();
32 }
```

Line 17 shows the turbulent viscosity via computed by (2.49), including the value of the model constant $C_A$. The constant suitable for the AMD model is recommended from (Rozema et al., 2015) with respect to the order of discretization of Navier-Stokes equations, tested on decaying grid turbulence cases. The AMD model gave the best results with $C_A = 0.300$ for a central second-order scheme and $C_A = 0.212$ for a fourth-order scheme. A recent study by Zahiri and Roohi (2019) states an optimal value of the constant $C_A = \frac{1}{\sqrt{3}} = 0.577$ based on various study cases. Author's own test of model constants ($C_A = 0.3$ and $C_A = 0.57735$) was performed and results are discussed in Chap. 2.1.5.

Rozema et al. (2015) has shown that after a Taylor expansion of $\tau_{ij}$ it can be shown that the AMD model is really consistent with the exact subgrid-scale stress tensor

$$\tau_{ij} = \overline{u_i u_j} - \overline{u}_i \overline{u}_j = \frac{1}{12}(\delta x_k \partial_k u_i)(\delta x_k \partial_k u_j) + \mathcal{O}(\delta x_i^4) \tag{2.52}$$

and the eddy dissipation of the exact subgrid-scale stress tensor is approximated as

$$-\tau_{ij} S_{ij} = -\frac{1}{12}(\delta x_k \partial_k u_i)(\delta x_k \partial_k u_j) S_{ij} + \mathcal{O}(\delta x_i^4), \tag{2.53}$$

which means that the term $A_{ij}$ in (2.49) is consistent with the product of Taylor series in (2.53). The term $A_{ij}$ is also referred as the gradient sub-filter model (Vreman, 1995). If the exact eddy dissipation gives zero dissipation, then the term $A_{ij}$ as well, this means the AMD model can be switched off for flows where the exact eddy dissipation is vanishing. Thus, the AMD model also switches off when no SGS energy is created (Rozema et al., 2015; Vreugdenhil and Taylor, 2018).

One of the complex applications of the AMD model has been made by Zahiri and Roohi (2019), including cavitating and non-cavitating external flow around a sphere. Despite a coarser grid, the AMD model predicts accurate location of separation point, pressure and friction coefficients (compared to a detached eddy simulation).

Another application of the AMD model is for example computation of atmospheric boundary layer flows in the thermally stratified atmosphere (Abkar and Moin, 2017), where authors slightly modified the AMD model by adding a contribution of buoyant forces. In addition, the authors pointed out a relatively high grid-independence of the modified AMD model.

The anisotropic behavior of the AMD model can be advantageous in dynamic mesh applications, such as the moving grid within the glottis. In the following sections, the new implementation of the AMD model is thus verified on two test cases.

### 2.1.5 Verification of the AMD implementation: plane channel

As a first case validating the newly implemented AMD model in OpenFOAM was chosen "channel395", internal horizontal incompressible flow between parallel smooth walls with Reynolds number based on friction velocity, $\mathrm{Re}_\tau = |u_\tau| h/\nu = 395$, $\mathrm{Re} = 7890$. The mesh used in the unsteady simulation was built from 80x120x60 hexahedral elements $(x, y, z)$ and the initial steady simulation, from which the results were mapped into the finer mesh, was performed on a coarse grid (40x60x30). The boundary condition at walls was treated by the no-slip condition. The periodic boundary conditions were prescribed at inlet and outlet to cope with continuous inflow and outflow to ensure a fully turbulent regime. First, the AMD model was tested with two model constants introduced in the literature

to handle the settings for this case and get a close agreement with the DNS provided by Moser et al. (1999). The graph in Fig. 2.1 (left) shows the difference between the AMD model with $C_A = 0.300$ and $C_A = 0.577$. The case with $C_A = 0.300$ follows the trend of the DNS curve in range $y^+ \in (40; 140)$ better, whereas the $C_A = 0.577$ seems to be closer in $y^+ < 40$. Hence, for next computations was chosen $C_A = 0.577$. In Fig. 2.1 (right), the newly implemented AMD model is compared to traditional SGS models. It can be seen that the prediction of the AMD model lies closer to the DNS data. This confirms proper implementation of the AMD code into the OpenFOAM package.

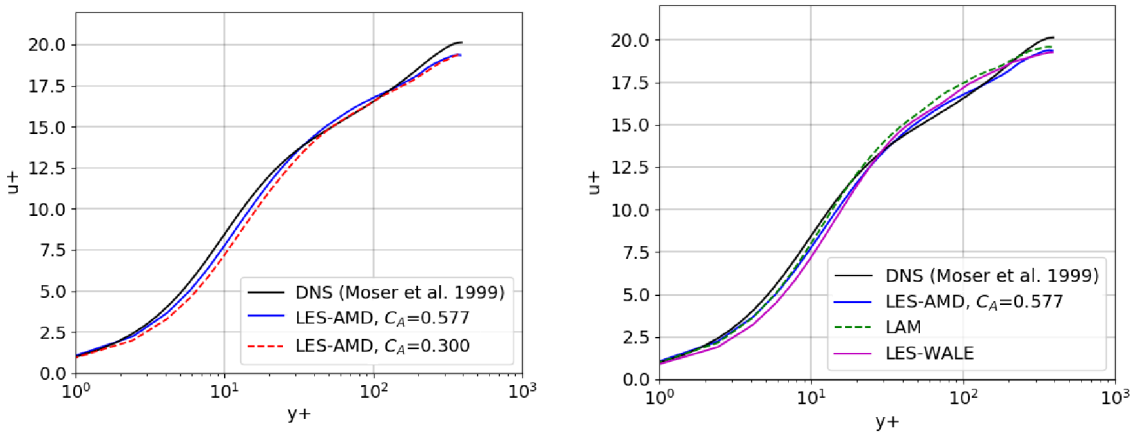


Fig. 2.1: Turbulent flow in a plane channel. $u^+ = \langle u \rangle / u_\tau$ denotes normalized velocity.

### 2.1.6 Verification of the AMD implementation: periodic hill

This section contains another test case of incompressible single-phase turbulent flow in a channel, but this time involving a periodic arrangement of smooth curved constrictions to force flow separation. The sketch of the instantaneous flow field, geometry configuration and position of vertical lines for subsequent analysis is attached in Fig. 2.2. Boundary conditions are cyclic in the streamwise (x-axis) and spanwise (z-axis) direction and at the top and bottom walls the no-slip condition is prescribed. The mean bulk velocity $U_b$ is set to 1 m/s. The height of the hill $h$ is 0.028 m, the length of the domain is $9\,h$ and the last parameter, height of the channel, is $3.035\,h$. The mesh consists of 160x200x80 hexahedral elements. Flow parameters are held in a fully turbulent regime at Re = 10595, with streamwise Görtler-type vortices and spanwise Kelvin-Helmholtz instabilities in separated shear-layer (Schlichting and Gersten, 2016).

The test case was chosen from the following reasons:

- The Reynolds number is set up to 10595, corresponding to the laryngeal flow more precisely than the previous test case "channel395";
- The separated flow is included;
- Validation DNS data are well available (Fröhlich et al., 2005);

The flow is driven from the left side downstream into the domain. The separation occurs shortly downstream of the crest due to adverse pressure gradient forming the

recirculation zone at the "lee-ward side" of the hill. Afterward, the flow reattaches between the two hills. The exact point of the separation and reattachment varies with the Reynolds number.

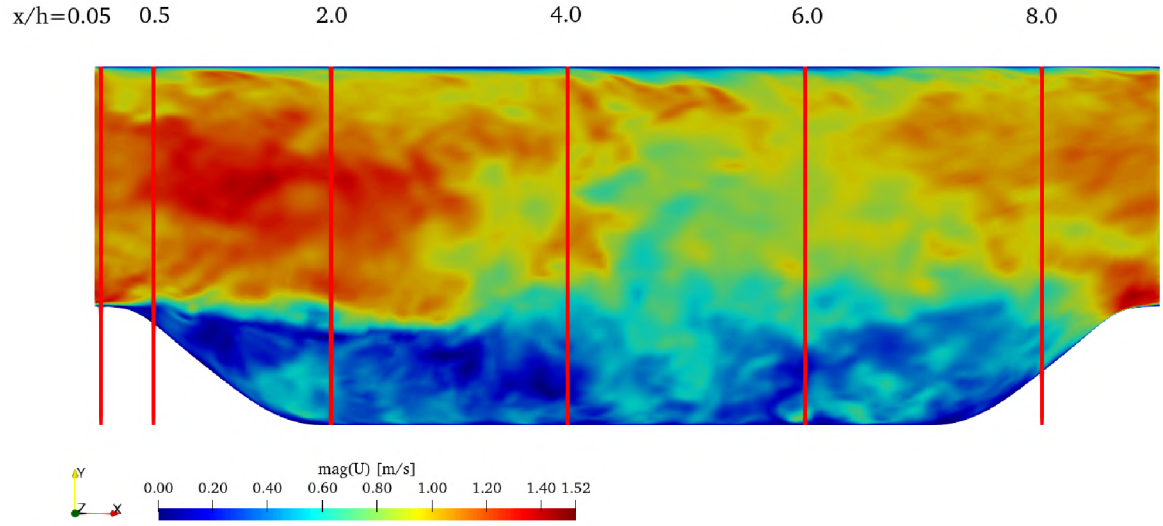


Fig. 2.2: Periodic hill test case: geometry, instantaneous velocity, evaluation locations.

In this paragraph, normalized velocity profiles from simulations are shown in Figs. 2.3-2.5, presenting the temporal averaged normalized velocity component $\langle u \rangle$ in different locations to highlight the fundamental characteristics of the flow when using various subgrid-scale models.

In Fig. 2.3 (left) are velocity profiles at $x/h = 0.05$, where the flow is attached to the bottom wall. Near the bottom wall, the AMD model predicts significantly higher flow velocity than other models. On the other side, the other simulations underestimate the velocities compared to the DNS curve.

Fig. 2.3 (right) shows velocity profiles at $x/h = 0.5$, where the simulation with AMD was not able to capture the reverse flow.

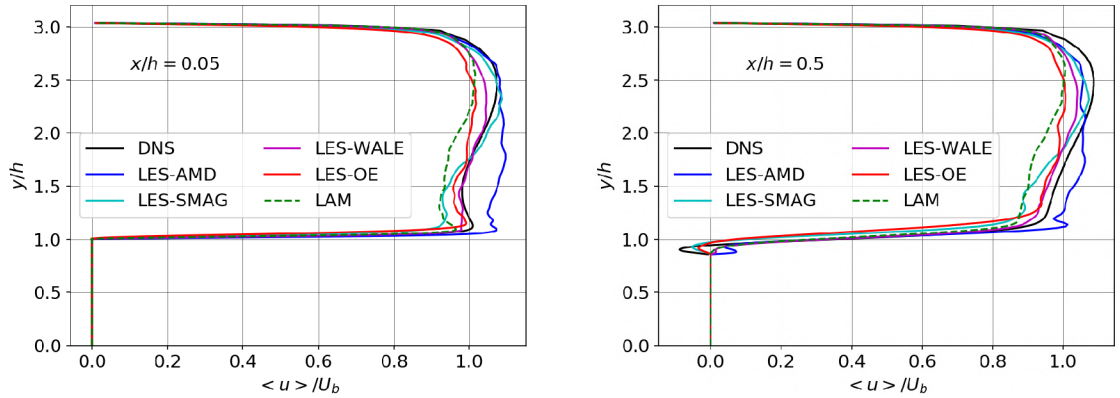


Fig. 2.3: Mean velocity profiles of the flow over a periodic hill at $x/h$=0.05 (left), where the flow is attached on the bottom, and at $x/h$=0.5 (right), where the first separation is indicated.

In Fig. 2.4 (left) are plotted velocity profiles at $x/h$=2, where the recirculation zone behind the hill is catched. The velocity profile at the bottom obtained from the simulation with AMD is in good agreement with the DNS data, and surprisingly the curves corresponding to simulations with WALE and SMAG models overpredict the mean velocity.

Fig. 2.4 (right) shows velocity profiles at $x/h$=4, where the reattachment zone is catched. The simulation with AMD shifted the maximum mean velocity from $y/h = 2.5$ to 2.0, as compared with the DNS curve. The simulation with SMAG predicted the mean velocity best at the reattachment zone.

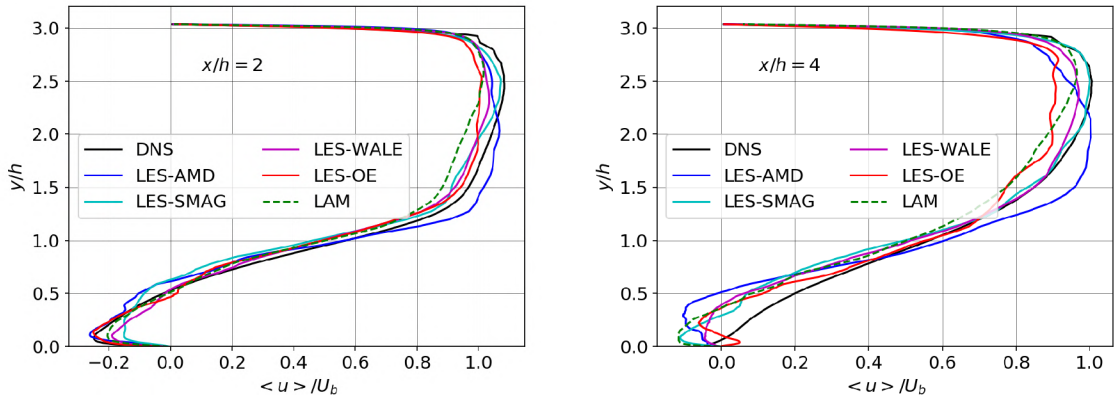


Fig. 2.4: Mean velocity profiles of the flow over the periodic hill at $x/h$=2 (left) and $x/h$=4 (right), where the recirculation zone and reattachment zone are seen, respectively.

In Fig. 2.5 (left) are velocity profiles $x/h = 6$, where the flow is reattached again. The simulation with AMD predicted higher mean velocity at the half-height of the domain compared to velocity obtained from DNS, whereas simulations with WALE and SMAG models were in relatively good agreement.

Fig. 2.5 (right) shows the velocity profiles at $x/h = 8$, where the reacceleration of the flow is identified. The velocity profile predicted by AMD is acceptable. Velocity profiles from simulations with OE underpredicted mean velocity from $x/h = 4$ and further downstream.

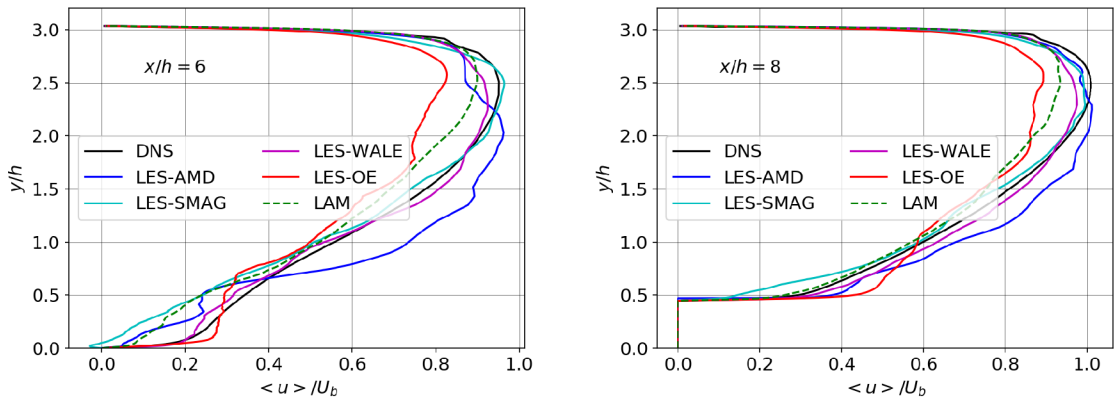


Fig. 2.5: Mean velocity profiles of the flow over the periodic hill at $x/h$=6, where the flow is reattached and at $x/h$=8, where the flow is reaccelerated.

The usage of the AMD model required an improvised numerical setup due to the absence of tuned tutorial cases in OpenFOAM with the AMD model. This probably affects the quality of the simulation.

## 2.2 Geometry and boundary conditions

The computational domain for the CFD simulation represents a simplified model of the human larynx with a rectangular cross-section, consisting of a short subglottal channel, glottal constriction formed by the vocal folds, ventricles, further contraction by the false vocal folds, and straight supraglottal channel (see Fig. 2.6).

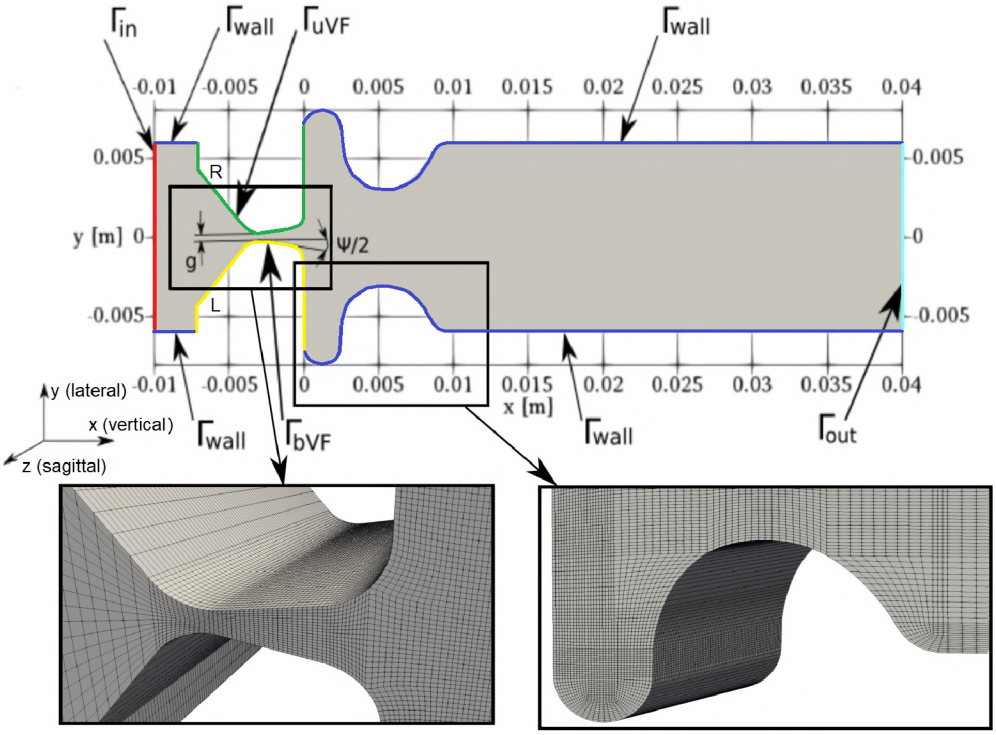


Fig. 2.6: Mid-coronal (x-y) section of the CFD computational domain, domain boundaries and details of the computational mesh. The z-normal (front and back) boundaries belong to $\Gamma_{\text{wall}}$. Enclosed figures about mesh representation are discussed in Chap. 2.3.

The geometry of vocal folds is based on the M5 parametric shape by Scherer et al. (2001). The false vocal folds were specified according to data published by Agarwal et al. (2003). The geometrical model is in 3D, having a square cross-section at inlet 12x12 mm. More details can be found in (Šidlof et al., 2015). The boundary conditions for the CFD model are summarized in Tab. 2.1. The flow is driven by constant pressure difference $P_k = \overline{p}/\rho = 300$ m$^2$/s$^s$ between the inlet $\Gamma_{\text{in}}$ and outlet $\Gamma_{\text{out}}$. The velocity on $\Gamma_{\text{in}}$ and $\Gamma_{\text{out}}$ is computed from the flux. The flow enters at the inlet and exits at the outlet or is set to zero in case of backflow. On the fixed channel walls, a no-slip boundary condition $\mathbf{u} = \mathbf{0}$ is prescribed.

Tab. 2.1: Boundary conditions for the filtered flow velocity $\overline{\mathbf{u}}$ and static pressure $\overline{p}$. The symbol $\mathbf{n}$ is the unit outer normal and $h(\mathbf{x}, t)$ is the prescribed displacement of the vocal folds. $\Gamma_{\text{wall}}$ also includes the front and back surface.

| **Boundary** | $\overline{\mathbf{u}}$ [ms$^{-1}$] | $\overline{p}$ [Pa] |
|---|---|---|
| $\Gamma_{\text{in}}$ | $\overline{\mathbf{u}} = \mathbf{0}$ if $\overline{\mathbf{u}} \cdot \mathbf{n} < 0$, $\nabla(\overline{\mathbf{u}}) \cdot \mathbf{n} = \mathbf{0}$ if $\overline{\mathbf{u}} \cdot \mathbf{n} > 0$ | 350 |
| $\Gamma_{\text{out}}$ | $\overline{\mathbf{u}} = \mathbf{0}$ if $\overline{\mathbf{u}} \cdot \mathbf{n} < 0$, $\nabla(\overline{\mathbf{u}}) \cdot \mathbf{n} = \mathbf{0}$ if $\overline{\mathbf{u}} \cdot \mathbf{n} > 0$ | 0 |
| $\Gamma_{\text{bVF}}$, $\Gamma_{\text{uVF}}$ | $\overline{u}_1 = 0$, $\overline{u}_2 = \frac{\partial}{\partial t} h(\mathbf{x}, t)$, $\overline{u}_3 = 0$ | $\nabla(\overline{p}) \cdot \mathbf{n} = 0$ |
| $\Gamma_{\text{wall}}$ | $\overline{\mathbf{u}} = \mathbf{0}$ | $\nabla(\overline{p}) \cdot \mathbf{n} = 0$ |

On the moving boundaries $\Gamma_{\text{bVF}}$ and $\Gamma_{\text{uVF}}$, the flow velocity is equal to the velocity of the moving vocal fold surface, given by function $h(\mathbf{x}, t)$. The function $h(\mathbf{x}, t)$ based on the sinusoidal displacement $w_{1,2} = A_{1,2} \sin(2\pi f_o t + \xi_{1,2})$ ensures the vibrating motion of vocal folds in the medial-lateral ($y$) direction with two degrees of freedom. In the current simulation, the vocal folds oscillate symmetrically with a frequency $f_o = 100$ Hz, amplitudes at the superior and inferior vocal fold margin are $A_1 = A_2 = 0.3$ mm. The medial surface convergence angle is marked in Fig. 2.6 as $\psi/2$, which confines the convergent and divergent position (-10 deg and +10 deg). The phase difference between the inferior $w_1(\xi_1)$ and superior $w_2(\xi_2)$ vocal fold margin is $\xi_1 - \xi_2 = \pi/2$. The distance (y) between both ventricles and both false vocal folds equals 16 and 6.15 mm, respectively. In this study, the oscillation of the vocal folds allows closing/opening the glottal gap $g$ in the range 0.42-1.46 mm.

## 2.3 Mesh

In wall-bounded flows, the presence of solid walls fundamentally influences the flow dynamics, turbulence generation, and transport in the near-wall regions due to significant viscous stresses. The accuracy of the numerical simulation is thus closely related to the grid resolution near the fixed walls. According to the classification by Pope (2000), large-eddy simulations of wall-bounded flows can be classified as large-eddy simulations with near-wall resolution (LES-NWR) with a grid sufficiently fine to resolve 80% of the turbulent energy in the boundary layer, and large-eddy simulation with near-wall modeling (LES-NWM), which simulation employs a modeling approach similar to RANS in the near-wall region. For these simulations, an important parameter is the wall unit

$$y^+ = \frac{u_\tau y}{\nu} \,, \tag{2.54}$$

where $u_\tau = \sqrt{\frac{|\tau_w|}{\rho}}$ is the friction velocity, $\tau_w = \mu_{\text{eff}} \left(\frac{\partial U}{\partial y}\right)\Big|_{y=0}$ is the wall shear stress, $\mu_{eff} = (\mu + \mu_t)$ is the effective dynamic viscosity and $y$ the dimensional distance in normal direction from the wall. The wall unit $y^+$, commonly referred to as "y plus", is used as the dimensionless wall-normal distance. Using the same normalization, $x^+$ and and $z^+$ denote the dimensionless streamwise and spanwise distances. Wall units are also

commonly used to indicate LES adequacy. According to (Georgiadis et al., 2010) and (Jiang and Lai, 2016), in LES-NWR the theoretical limits for the grid spacing adjacent to the wall are $50 \leq \Delta x^+ \leq 150$, $\Delta y^+ < 1$ and $15 \leq \Delta z^+ \leq 40$, with at least 3-5 gridpoints between $0 < y^+ < 10$.

The computational mesh in the current CFD simulation (see Fig. 2.1) is block-structured to capture well the boundary layer and consists of 2.1M hexahedral elements. An open source 3D finite volume mesh generator blockMesh was used to build the mesh. The mesh deforms in time due to vocal fold oscillation. The grid resolution in wall units was evaluated in three distinct time instants, corresponding to a maximum opening of the vocal folds, full closure during the divergent phase and full closure during the convergent phase. On the boundary $\Gamma_{\mathrm{bVF}}$ at the critical time when the vocal folds are maximally adducted were evaluated these values: $y^+_{avg} = 1.77$, $z^+ = 14$ and $x^+ = 8$.

## 2.4 Discretization and numerical solution

The Navier-Stokes equations were discretized using the collocated cell-centered Finite Volume Method. Fletcher (1991) demonstrated that even-ordered derivatives in the truncation error are associated with numerical dissipation, and odd-ordered spatial derivatives are associated with the numerical dispersion in the solution. Ideally, LES simulations should use schemes with low numerical dissipation. The non-dissipative central differencing scheme, which was applied in this study, allows an accurate representation of the changing flow field (Launchbury, 2016). The discretization of the diffusion term is split into an orthogonal and cross-diffusion term, using a procedure described in (Jasak, 1996). Unlike the discretization of the temporal, convective, and orthogonal part of the diffusive term, the nonorthogonal correctors are treated explicitly.

CFD simulations were run in parallel on:

1. Charon (Metacentrum NGI - Faculty of Mechatronics, Technical University of Liberec)
   - 20 cores on a computational cluster, composed of nodes with two 10-core Intel Xeon Silver 4114 2.20GHz CPUs with 96GB RAM,
2. Fox (Computing center of the Czech Technical University in Prague)
   - 20 cores on a supercomputer (SGI Altix UV 100) with shared memory 576GB RAM with the involvement of 6-core Intel Xeon Nehalem 2.66GHz CPUs.

In order to have sufficient resolution in the spectrum of the aeroacoustic signal, a sufficiently long simulation time $t = 0.2$ s, i.e. 20 periods of vocal fold vibration, is needed. For such a setting, one CFD simulation required 27 - 37 days, i.e. about 15000 core-hours of computational time.

## 2.5 CFD results

The current study reports on the results of four CFD simulations using different turbulence modeling approaches, which are summarized in Tab. 2.2. The laminar case "LAM" used no turbulence model. "OE", "WALE" and "AMD" are LES simulations with the One-Equation, WALE SGS and AMD SGS models, respectively. The simulations were run in

parallel on 20 CPU cores for 20 periods of vocal fold oscillations, i.e. $t = 0.2$ s, either on the computational cluster Charon, or on the symmetric multiprocessing machine Fox. Hardware specifications are included in Chap. 2.4.

Tab. 2.2: Overview of the CFD simulations.

| Case | Type | SGS model | CPU | Cluster | Wall-time |
|---|---|---|---|---|---|
| LAM | laminar | - | 20 | Charon | 27d 13h |
| OE | LES | One-Equation | 20 | Charon | 34d 05h |
| WALE | LES | WALE | 20 | Charon | 37d 13h |
| AMD | LES | AMD | 20 | Fox | 34d 18h |

### 2.5.1 Laryngeal flow rate

Fig. 2.7 shows the glottal opening and flow rates during the last four simulated cycles of vocal fold oscillation. The time $t_N$ corresponds to the instant where the inferior margins of the vocal folds approach most and reduce the glottal opening to 5.58 mm$^2$. Time instant $t_C$ is the maximum approach of the superior vocal fold margins, where the glottal opening drops to 4.98 mm$^2$. The third time instant, $t_O$, corresponds to the maximum glottal opening of 17.51 mm$^2$. Glottal gaps listed in mm are in Tab. 2.3.

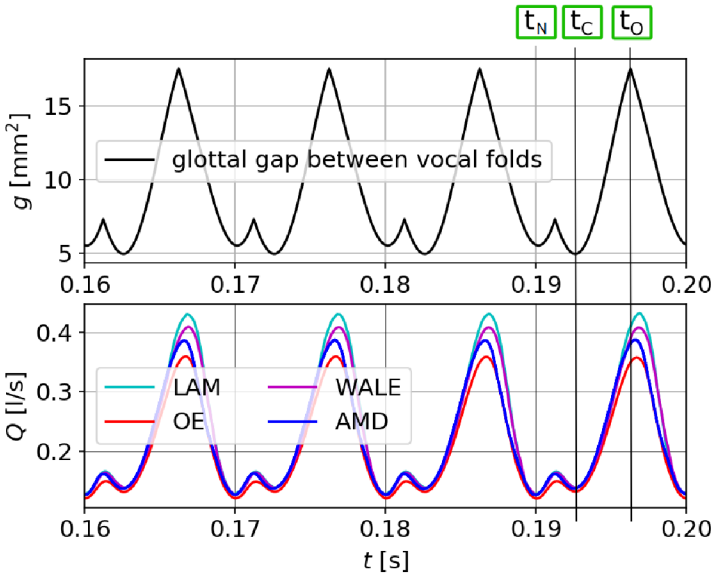


Fig. 2.7: Glottal gap and flow rates during four oscillation cycles. Time instants for further analysis: $t_N = 0.1900$ s, $t_C = 0.1927$ s and $t_O = 0.1963$ s.

Tab. 2.3: Glottal gaps at time instants.

| Time | $g$[mm$^2$] | VF gap[mm] |
|---|---|---|
| $t_N$ | 5.58 | 0.465 |
| $t_C$ | 4.98 | 0.415 |
| $t_O$ | 17.51 | 1.459 |

The subgrid-scale models affected the flow rates $Q$[l/s] (see Fig. 2.7): the predicted peak flow rate in the laminar case is higher than in the One-Equation, WALE and AMD

SGS models by 16.76%, 5.26% and 9.3%, respectively. This is caused by the different values of the SGS viscosity, which adds to the molecular viscosity and limits the flow rate through the glottal constriction. The laminar model does not capture the influence of small-scale turbulence, which corresponds to $\nu_t = 0$. The WALE SGS model and the One-Equation SGS model compute with non-zero SGS viscosity, with the latter one significantly higher due to the already mentioned deficiency of the One-Equation model, which overestimates the turbulent viscosity near the vocal fold surfaces. The flow rate does not reach zero value, corresponding physiologically to breathy phonation. The vocal folds do not fully close the glottal channel from technical reasons. The minimum flow rate is $Q_{min} \approx 0.122$ l/s. The maximum flow rates are between $0.358 - 0.434$ l/s, see Tab. 2.4. The peak flow rate predicted by the AMD model occurs sooner than in other simulations (when 66% of the VF cycle is reached).

Tab. 2.4: Minimum and maximum flow rates [l/s] and state of the oscillation cycle of vocal folds [%] when the maximum flow rate is reached.

| Case | $Q_{\min}$[l/s] | $Q_{\max}$[l/s] | VF cycle($Q_{\max}$)[%] |
|---|---|---|---|
| LAM | 0.129 | 0.434 | 69 |
| OE | 0.122 | 0.358 | 67 |
| WALE | 0.128 | 0.409 | 69 |
| AMD | 0.127 | 0.389 | 66 |

### 2.5.2 Velocity and pressure distribution

The CFD simulations provide filtered velocity and pressure fields $(\overline{u}, \overline{p})$. For simplicity the overbars are dropped in the following presentation of results. Fig. 2.8 shows 3D laryngeal velocity fields during vocal fold oscillation. The vocal folds at $t_N$ and $t_C$ reduced the glottal jet. The strongest jet is visible at $t_O$ when the vocal folds are maximally open.

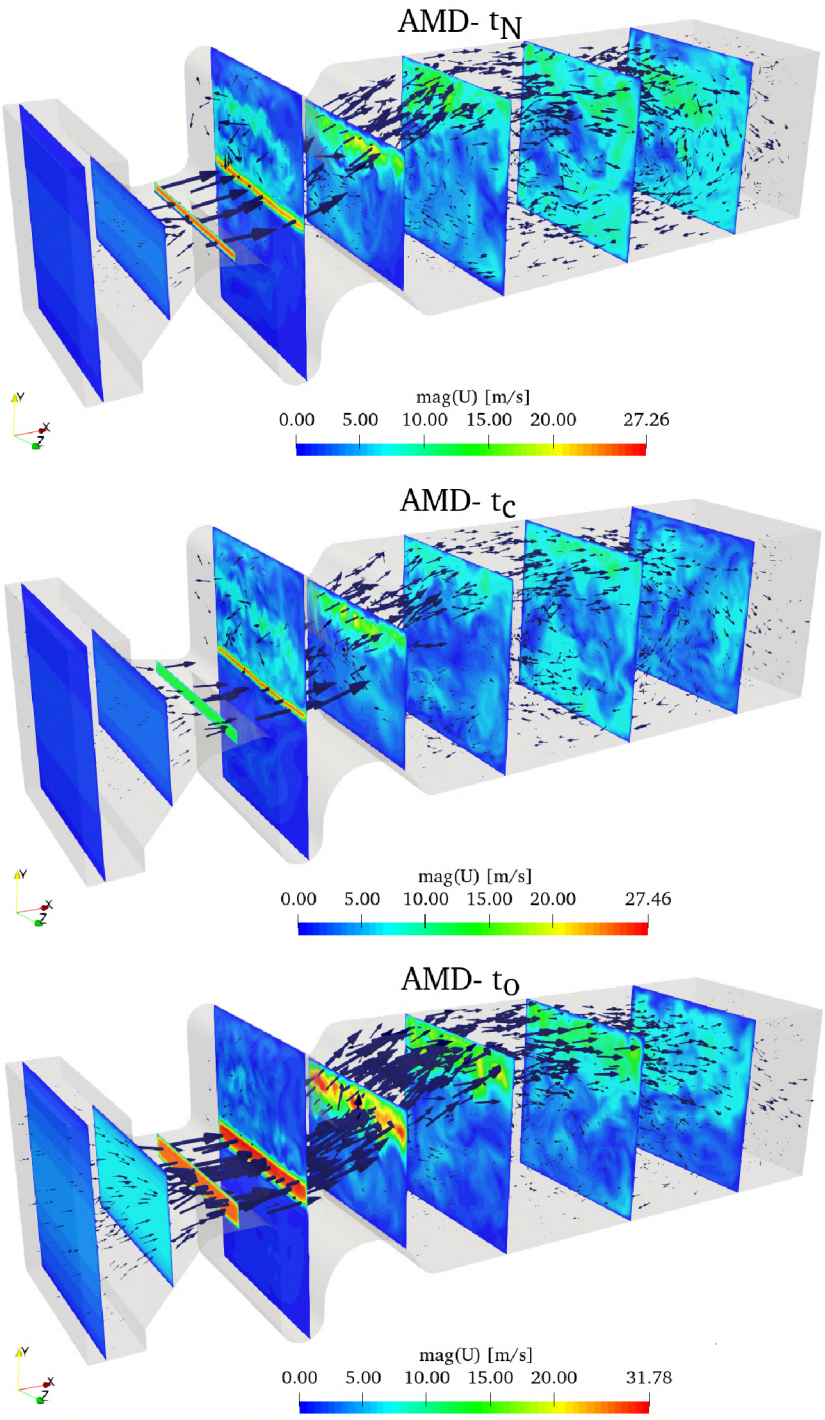


Fig. 2.8: Visualization of laryngeal flow at $t_N$, $t_C$ and $t_O$. Contours of the jet can be observed.

In Fig. 2.9, the effect of the SGS models is analysed in the mid-coronal plane. Velocity magnitudes at three distinct times obtained from four simulations can be compared. The jet in the supraglottal region interacts with turbulent structures and gradually decays.

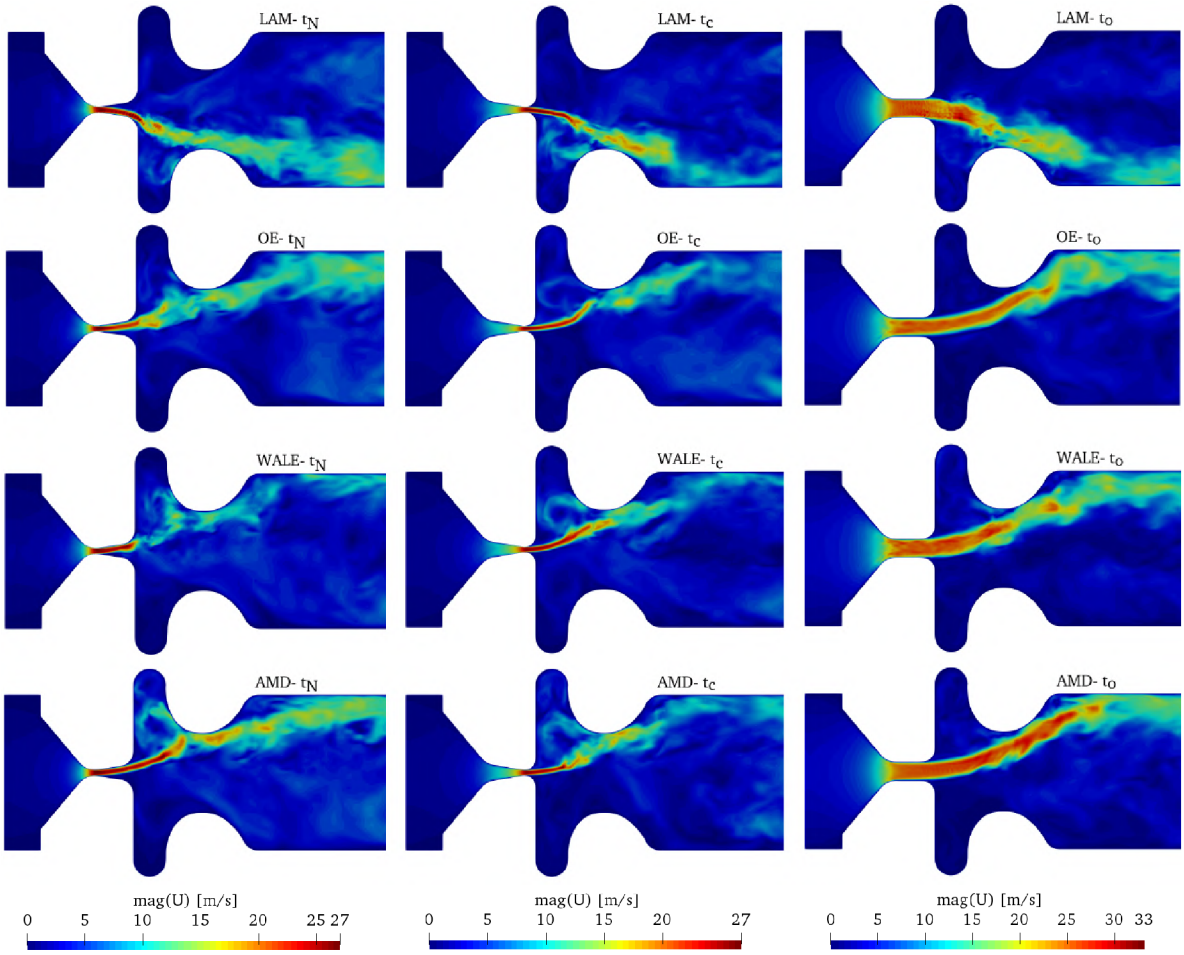


Fig. 2.9: Mid-coronal view on the velocity magnitude.

Fig. 2.10 shows velocity fields in the mid-sagittal (x-z) plane, where spanwise structures of expanding jets during phonation can be seen (airflow is from left to right). Velocity fields obtained from the simulation with AMD have smooth distribution of velocity through the glottis.

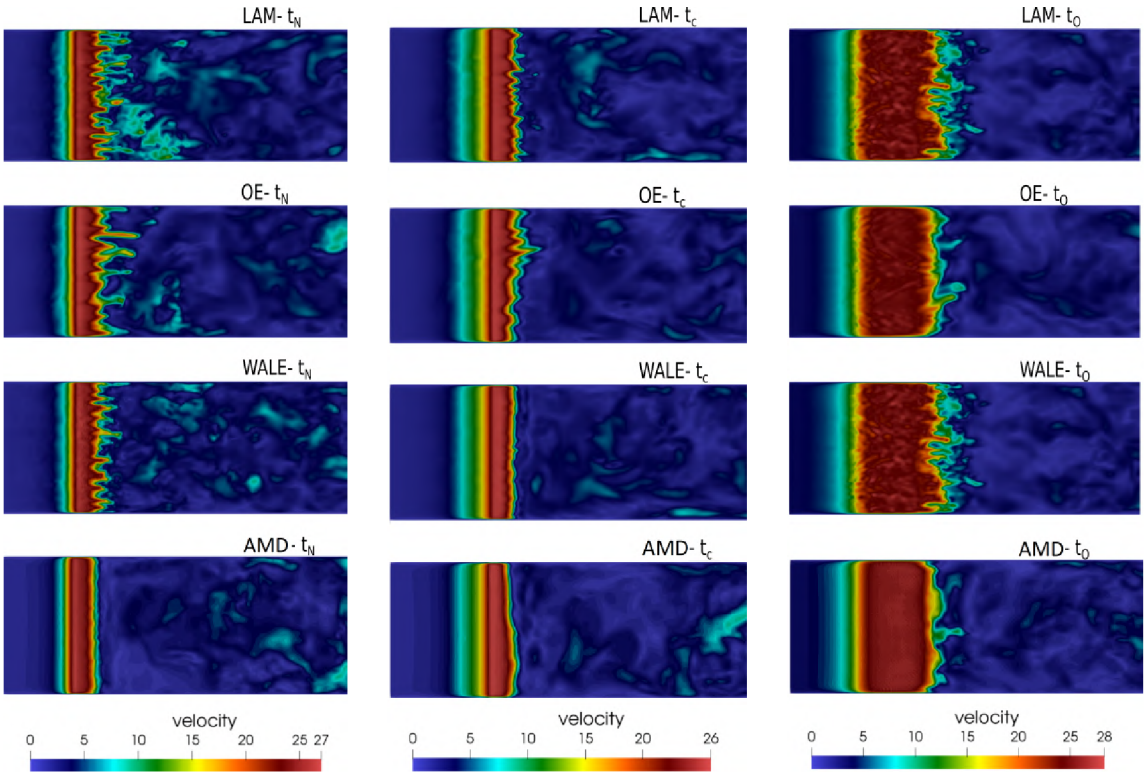


Fig. 2.10: Instantaneous velocity fields [m/s] in mid-sagittal plane in three time instants.

The velocity and pressure fluctuations along the glottal mid-line ($x$) are plotted in Fig. 2.11. The glottal region (bounded by the inferior and superior margin of the vocal folds) is shaded. The maximum flow velocity in the glottis reaches 26.2 m/s. The velocity curve obtained from the simulation with AMD seems to be perturbed least in the supraglottal turbulent region, which is evident especially at $t_N$, where the finite volumes are stretched. This may be a feature of AMD reacting on mesh deformation. The right column shows the pressure profiles in the laryngeal domain, where lower pressure corresponds to increased velocities and *vice versa*. The location of the minimum pressure in the glottis is shifted by change from the divergent ($t_N$) to convergent ($t_C$) position of vocal folds by 2 mm. In the divergent position of the vocal folds, the flow is perturbed even within glottis. The 3D pressure distribution is also visualized in Fig. 2.12.

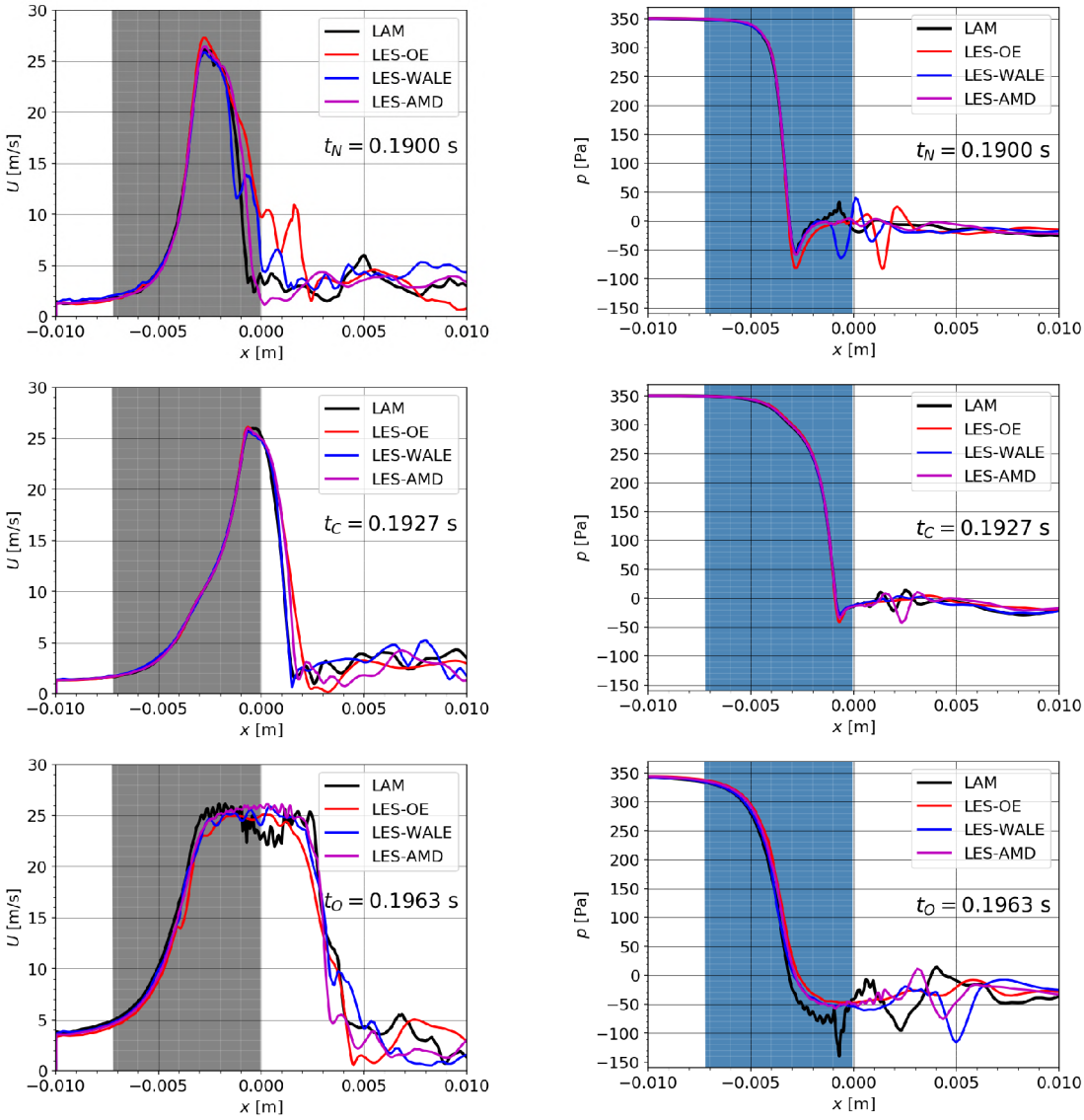


Fig. 2.11: Velocity magnitude (left) and pressure distributions (right) along the glottal mid-line ($x$) in time instant $t_N$ (1st row), $t_C$ (2nd row) and $t_O$ (3rd row). Color background denotes the region of the moving vocal folds (glottis).

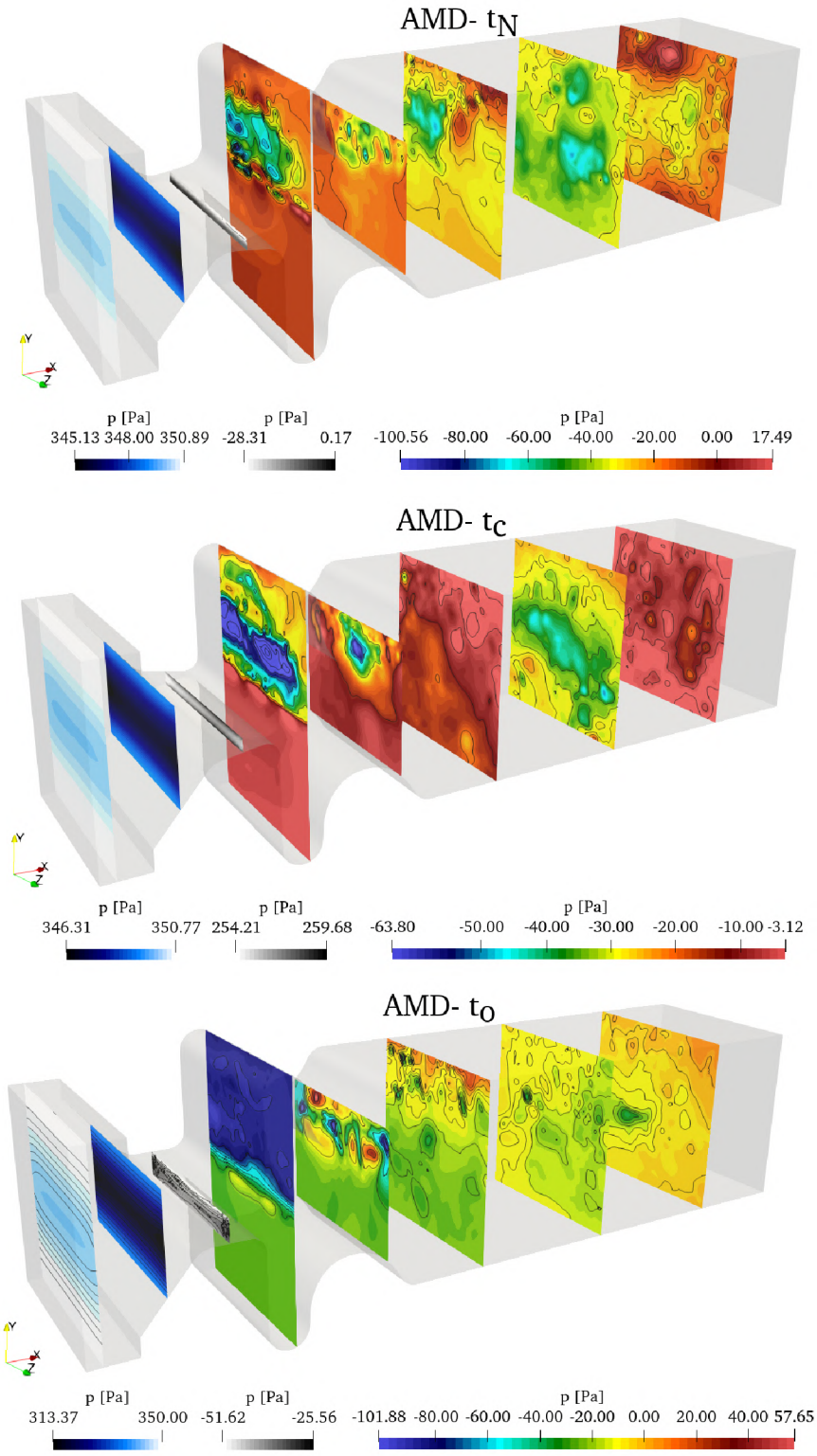


Fig. 2.12: 3D visualization of the pressure distribution in the human larynx during vocal fold oscillation.

### 2.5.3 Vorticity field

Vorticity ($\boldsymbol{\omega} = \nabla \times \mathbf{u}$) is commonly used for characterizing turbulence in cases with no entrainment rotation. The vorticity fields reveal the shear layers, where vortices are shed as a consequence of Kelvin-Helmholtz instability. The vortices may undergo successive instabilities, leading to a direct kinetic-energy cascade towards the small scales. This paragraph presents vorticity fields at mid-coronal and mid-sagittal planes.

Fig. 2.13 shows vorticity fields presented in mid-coronal plane (x-y). The supraglottal jet deflects stochastically towards either of the ventricular folds. This behavior is not a consequence of the SGS model, it is caused by the bistability of the flow in this symmetric geometry (Erath and Plesniak, 2010; Lodermeyer et al., 2015). Detailed analysis of the vorticity within the glottal region shows that the average value of vorticity in glottal region is similar for all SGS models.

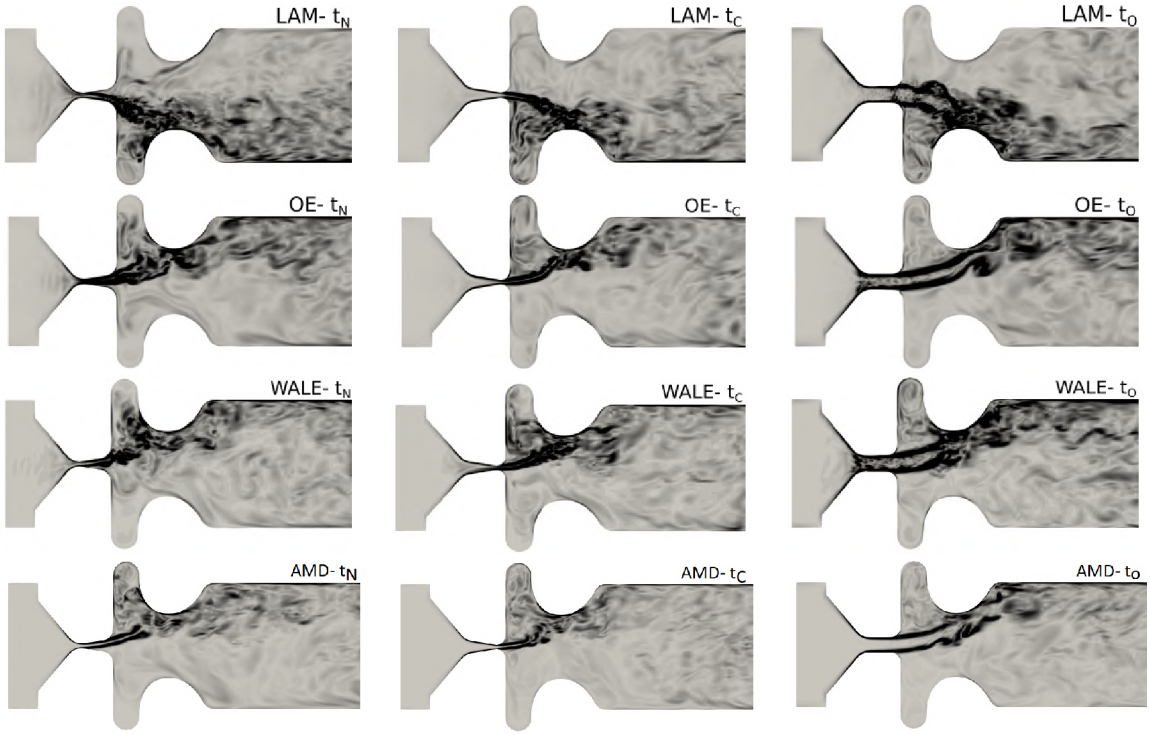


Fig. 2.13: Vorticity fields $|\boldsymbol{\omega}|$ in mid-coronal plane in range (0,30000) [$s^{-1}$].

Fig. 2.14 shows a complementary view on the magnitude of the vorticity vector $|\boldsymbol{\omega}|$ in mid-sagittal plane (x-z). The simulation with the AMD model predicts low vorticity in the vicinity of the glottis. The absence of vorticity may imitate the situation in the realistic larynx where the jet is frequently stopped and renewed, and thus the turbulent eddies are forced to be dissipated.

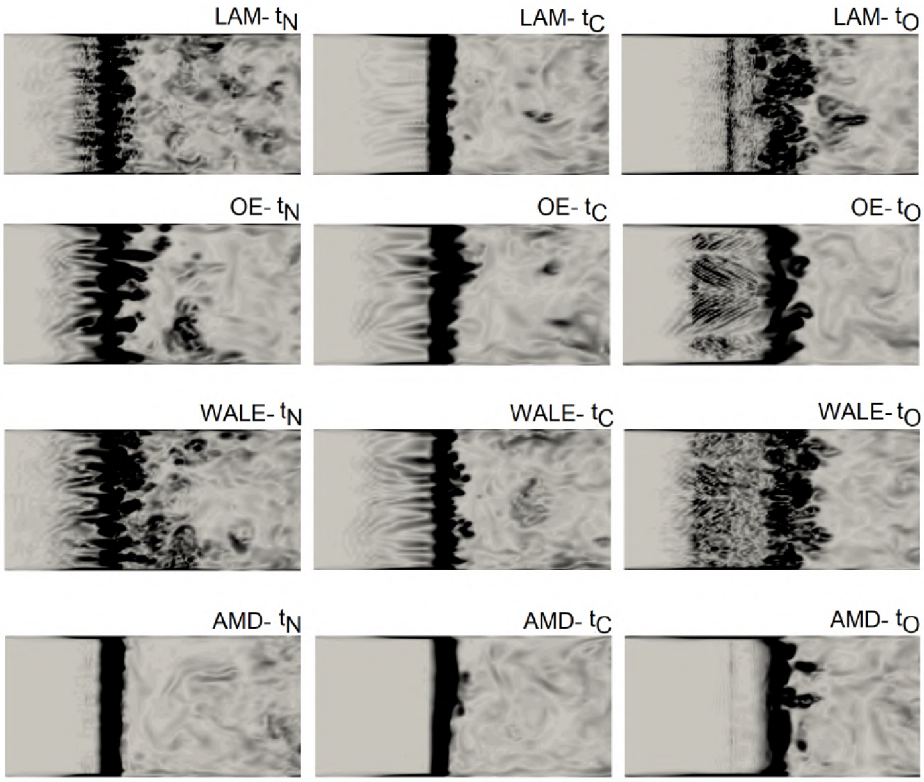


Fig. 2.14: Vorticity fields $|\boldsymbol{\omega}|$ in mid-sagittal plane in range (0,30000) [$s^{-1}$].

### 2.5.4 Turbulent viscosity field

The effect of the unresolved turbulent subgrid scales on the resolved scales is carried by the subgrid-scale turbulent viscosity $\nu_t$, represented by equations (2.24) for $\nu_t^O$, (2.34) for $\nu_t^W$ and (2.49) for $\nu_t^A$. The comparison between computations is shown in Figs. 2.15-2.17.

Figs. 2.15-2.16 show that the turbulent viscosity predicted by the simulation with the One-Equation model is very high in regions of pure shear, especially within glottis. This may be the reason why the simulation with the OE model predicted most of the time the lowest intraglottal velocity. In contrast to this, WALE and AMD subgrid-scale models predicted considerably lower subgrid-scale viscosity in the shear layers at $t_N$ and $t_C$. The fields computed by the AMD model seem to be similar to fields computed by WALE with spots of gently higher subgrid-scale viscosity at $t_N$ and $t_C$. The other situation occurs in $t_O$ when the turbulent viscosity predicted by the AMD model is around two times higher than by OE and five times higher than by WALE.

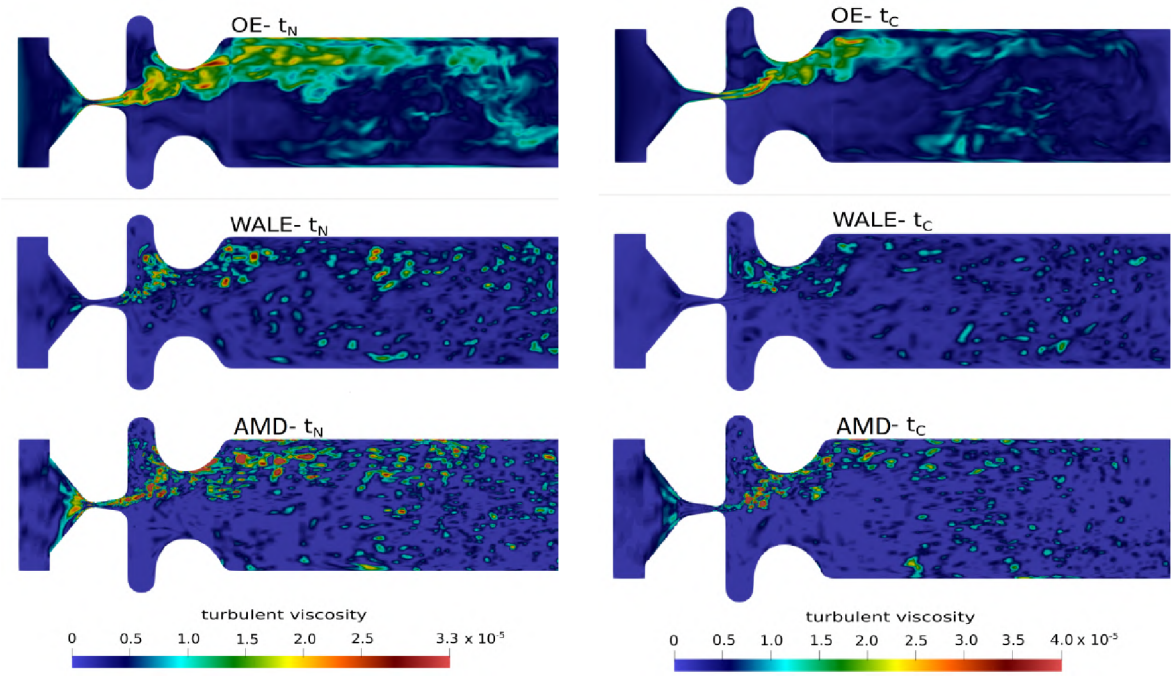


Fig. 2.15: Turbulent viscosity $\nu_t$ [$m^2.s^{-1}$] in the mid-coronal plane at $t_N$ (left) and $t_C$ (right).

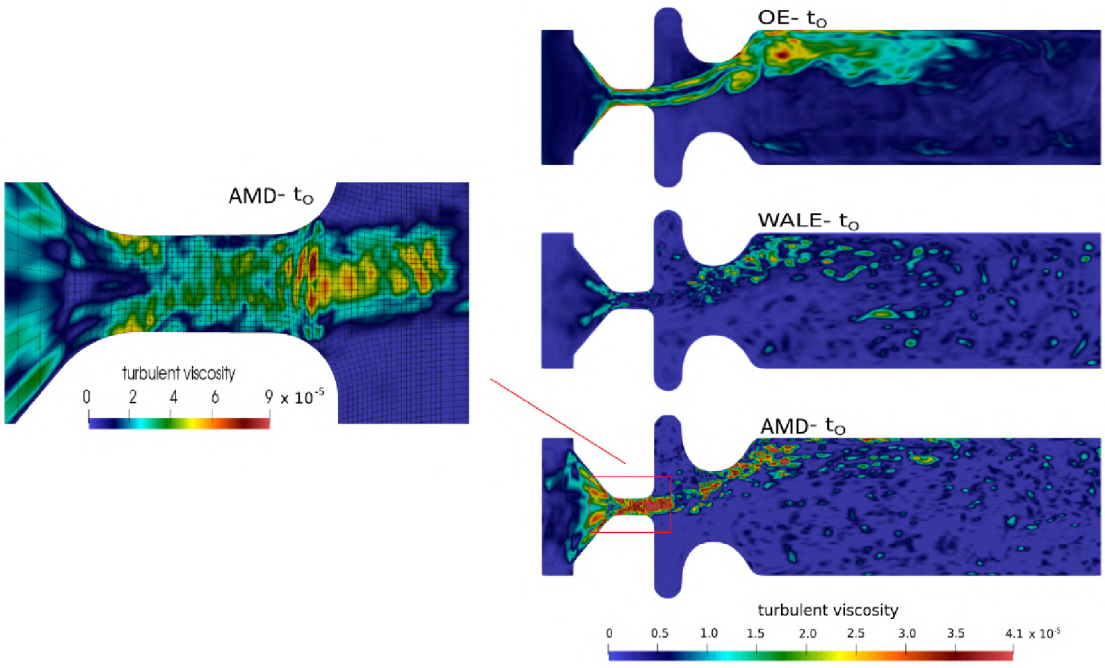


Fig. 2.16: Turbulent viscosity $\nu_t$ [$m^2.s^{-1}$] in the mid-coronal plane presented at fully open vocal folds.

Fig. 2.17 shows turbulent viscosity fields in mid-sagittal plane. The simulation with OE predicted twice higher turbulent viscosity located at vicinity of the inferior margin of the vocal folds than others. The narrow barrier of turbulent viscosity at $t_N$ in the case with AMD reduced the flow rate just by 0.8% (1 ml/s of air) compared to WALE.

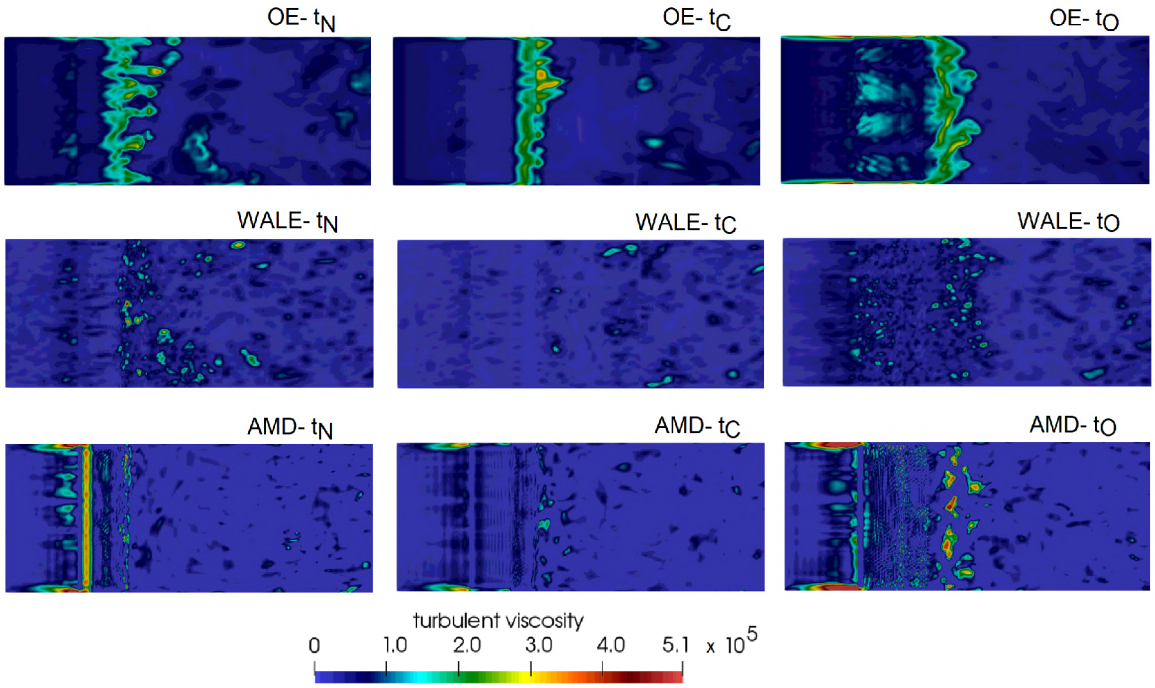


Fig. 2.17: Turbulent viscosity $\nu_t$ [$m^2.s^{-1}$] in the mid-sagittal plane.

## 2.6 Summary of findings

This paragraph summarizes the major findings after performing four CFD simulations of laryngeal flow based on various subgrid-scale models.

- Subgrid-scale turbulence model selection and configuration: The adjustment of dynamic constant in the subgrid-scale turbulence model and damping functions is not needed when the WALE and AMD models are used for the simulation of wall-bounded flows. The models contain a prediction of turbulent viscosity combining the strain rate and rotation rate tensor.

- Benchmark cases: The newly implemented AMD model has been subjected to two tests. The normalized velocity profiles from simulations of turbulent flow within the periodic plane channel were compared with DNS. The AMD model achieved better agreement with the DNS curve than the conventional WALE model. However, the second verification case showed that the AMD model has a tendency to overpredict the mean velocity in the middle of the channel.

- Laryngeal flow rates: The simulation with AMD predicted by 5.1% lower, 11.6% lower and 8.7% higher maximum than the WALE, LAM and OE models, respectively. In the AMD and OE cases, the peak flow rate in the vocal fold

oscillation cycle occurs noticeably sooner than with LAM and WALE subgrid-scale models.

- Velocity fields: High value of the turbulent viscosity has a tendency to reduce the airflow in the glottis and decrease intraglottal velocity. The simulation using the OE model, which is known to overestimate the turbulent viscosity near walls, confirms this statement.

- Vorticity fields: In the glottis was observed a significant reduction of vorticity predicted by AMD compared to WALE and the other models. This finding confirms the expectation that the AMD model is able to stop the production of the scaled velocity gradient energy, and hence the minimum dissipation is kept to a suitable range. This feature leads to the increased estimation of local turbulent viscosity, which smooths the rotation of velocity.

- Turbulent viscosity: The simulation with the AMD model predicted the highest local increase of the turbulent viscosity, identified directly before the glottal constriction and partly on the sagittal walls. The OE model also predicts high turbulent viscosity, expecially in the vicinity of the vocal fold margins and in the shear layer. The AMD model contributed to less turbulence intensity in the glottis.

# 3 CAA model of wave propagation in vocal tract

Aeroacoustics deals with flow-induced sound generation and wave propagation. Sound generation is caused by the turbulent motion of fluid, periodic varying flow fields, or aerodynamic forces acting on solids. The sources in the case of human phonation are commonly denoted as:

i. A monopole source term due to the motion of vocal folds (the term is zero when the vocal folds are fixed).

ii. A dipole source term due to the unsteady force exerted by the surface of the vocal folds onto the fluid.

iii. A quadrupole sound term due to the unsteady flow inside the vocal tract.

See (Zhao et al., 2002) for more details.

The numerical simulation of aeroacoustic effects can be performed either by using direct simulations or hybrid methods. Direct simulation is based on the compressible Navier-Stokes equations, which capture both the fluid dynamic and acoustic fluctuations. The limitation of this approach is hidden in the computational effort associated with the disparity of scales between the flow and acoustic variables (the small turbulent scales and the large acoustic wavelength during common speech), which can reach several orders of magnitude. To circumvent this problem, hybrid approaches are commonly used, where the flow field and the acoustic field are computed separately (Bae and Moon, 2008; Schoder et al., 2020; Lasota et al., 2021; Valášek, 2021). This work is also based on the hybrid approach.

For simplicity, the overbars $(\bar{\cdot})$ from the LES filtering are dropped in the following paragraphs and equations.

## 3.1 Acoustics

### 3.1.1 Linear acoustic wave equation

The linear acoustic wave equation is derived from the linearized Euler equations using acoustic perturbations $(\cdot)^a$ around variables $(\cdot)_0$

$$p = p_0 + p^a(\mathbf{x}, t), \quad \rho = \rho_0 + \rho^a(\mathbf{x}, t), \quad \mathbf{u} = \mathbf{u}_0(\mathbf{x}) + \mathbf{u}^a(\mathbf{x}, t), \tag{3.1}$$

where $\mathbf{u}^a$ is the acoustic particle velocity and $\mathbf{u}_0$ ambient flow velocity. Acoustic perturbations are

$$|p^a| \ll p_0, \quad |\rho^a| \ll \rho_0, \quad \mathbf{u}_0 = \mathbf{0}, \tag{3.2}$$

where a non-static solution of a very small order is considered.
Conservation of mass is reformulated using terms $(\cdot)_0$ and $(\cdot)^a$ as

$$\frac{\partial(\rho_0+\rho^a)}{\partial t}+\boldsymbol{\nabla}\cdot((\rho_0+\rho^a)(\mathbf{u}_0+\mathbf{u}^a))=q_{\mathrm{ma}}, \tag{3.3}$$

that is

$$\underbrace{\frac{\partial\rho_0}{\partial t}}_{=0}+\frac{\partial\rho^a}{\partial t}+\boldsymbol{\nabla}\cdot(\rho_0\mathbf{u}^a+\underbrace{\rho_0\mathbf{u}_0}_{=0}+\underbrace{\rho^a\mathbf{u}^a}_{\approx 0}+\underbrace{\rho^a\mathbf{u}_0}_{=0})=q_{\mathrm{ma}}, \tag{3.4}$$

where $q_{\mathrm{ma}}$ is a source term, the term $\mathbf{u}_0=0$ hence $\boldsymbol{\nabla}\cdot(\rho_0\mathbf{u}_0)=0$ and $\boldsymbol{\nabla}\cdot(\rho^a\mathbf{u}_0)=0$, and finally the multiplication of two perturbation quantities $\rho^{\mathrm{a}}\mathbf{u}^a$ is negligible. This leads to

$$\frac{\partial\rho^a}{\partial t}+\underbrace{\rho_0\boldsymbol{\nabla}\cdot\mathbf{u}^a+\boldsymbol{\nabla}\cdot(\rho^a\mathbf{u}^a)}_{\approx\rho_0\boldsymbol{\nabla}\cdot\mathbf{u}^a}=q_{\mathrm{ma}}. \tag{3.5}$$

Conservation of momentum is reformulated using terms $(\cdot)_0$ and $(\cdot)^a$ as well leading to

$$(\rho_0+\rho^a)\frac{\partial(\mathbf{u}_0+\mathbf{u}^a)}{\partial t}+\big((\rho_0+\rho^a)(\mathbf{u}_0+\mathbf{u}^a)\cdot\nabla\big)(\mathbf{u}_0+\mathbf{u}^a)+\boldsymbol{\nabla}(p_0+p^a)=\mathbf{q}_{\mathrm{mo}}, \tag{3.6}$$

where $\mathbf{q}_{\mathrm{mo}}$ is a source term and

- $\partial\mathbf{u}_0/\partial t$ and $\partial\rho_0/\partial t$ are zero,
- $\rho^a\partial\mathbf{u}^a/\partial t$ is a second-order term, which can be neglected,
- spatial derivatives in the convective term containing $\mathbf{u}_0$ are zero,
- and $\boldsymbol{\nabla}p_0=0$ is taken, i.e. $p_0$ does not vary over space.

Thereby, the equation (3.6) arrives at

$$\rho_0\frac{\partial\mathbf{u}^a}{\partial t}+\underbrace{\big((\rho_0+\rho^a)\mathbf{u}^a\cdot\nabla\big)\mathbf{u}^a}_{\approx 0}+\nabla p^a=\mathbf{q}_{\mathrm{mo}}, \tag{3.7}$$

where the convective term is neglected.
Next, the thermodynamic relation is taken into account with a constant entropy and linear pressure-density relation

$$p^a=c_0^2\rho^a, \tag{3.8}$$

employing speed of sound $c_0$. Now, after manipulations of (3.5)–(3.7) and using the relation (3.8), the linear acoustic wave equation can be written as

$$\frac{1}{c_0^2}\frac{\partial^2p^a}{\partial t^2}-\boldsymbol{\nabla}\cdot\boldsymbol{\nabla}p^a=\frac{\partial q_{\mathrm{ma}}}{\partial t}-\boldsymbol{\nabla}\cdot\mathbf{q}_{\mathrm{mo}}, \tag{3.9}$$

or as the Helmholtz's equation of acoustics

$$k^2\hat{p}^a+\boldsymbol{\nabla}\cdot\boldsymbol{\nabla}\hat{p}^a=j\omega\hat{q}_{\mathrm{ma}}-\boldsymbol{\nabla}\cdot\hat{\mathbf{q}}_{\mathrm{mo}}, \tag{3.10}$$

where $(\hat{\cdot})$ are Fourier transforms of the pressure and source terms; $\omega$ is the angular frequency (not to be confused with the vorticity vector $\boldsymbol{\omega}$); $j$ is the imaginary unit, and $k_w$ is the wave number

$$k_w = \frac{\omega}{c_0} = \frac{2\pi}{\lambda}, \tag{3.11}$$

representing spatial periodicity of waves, using the wavelength $\lambda$.

If (3.5) and (3.7) are written with zero sources, i.e.

$$\frac{\partial \rho^a}{\partial t} + \rho_0 \boldsymbol{\nabla} \cdot \mathbf{u}^a = 0 \tag{3.12}$$

and

$$\rho_0 \frac{\partial \mathbf{u}^a}{\partial t} + \boldsymbol{\nabla} p^a = \mathbf{0}, \tag{3.13}$$

then the linear wave equation (3.9) can be written with no source terms as

$$\frac{1}{c_0^2} \frac{\partial^2 p^a}{\partial t^2} - \Delta p^a = 0. \tag{3.14}$$

Applying a curl operator on the equation (3.13) leads to

$$\boldsymbol{\nabla} \times \frac{\partial \mathbf{u}^a}{\partial t} = \mathbf{0}, \tag{3.15}$$

which means that the acoustic velocity is a potential (curl-free) vector field. This allows expressing the acoustic velocity as a gradient of an acoustic scalar potential $\psi^a$

$$\mathbf{u}^a = -\boldsymbol{\nabla} \psi^a. \tag{3.16}$$

The negative gradient means the acoustic velocity is oriented from the higher potential to lower potential. (3.16) can be substituted into (3.13) to get another relation between acoustic pressure and acoustic potential

$$p^a = \rho_0 \frac{\partial \psi^a}{\partial t}. \tag{3.17}$$

The combination of relations (3.17), (3.16) and (3.8) in (3.12) and (3.13) results in

$$\frac{1}{c_0^2} \frac{\partial^2 \psi^a}{\partial t^2} - \Delta \psi^a = 0, \tag{3.18}$$

which is an attractive form of the wave equation with the acoustic scalar potential. It saves computational effort due to the absence of vector representation.

### 3.1.2 Analytic solution of wave equation

The analytic solution will be presented first. Green's functions are fundamental solutions of partial differential equations forced by Dirac distributions $\delta_d$

$$\frac{1}{c_0^2} \frac{\partial^2 G(\mathbf{x}^{\mathrm{o}}, \mathbf{y}^{\mathrm{s}}, t)}{\partial t^2} - \Delta G(\mathbf{x}^{\mathrm{o}}, \mathbf{y}^{\mathrm{s}}, t) = \delta_d(\mathbf{x}^{\mathrm{o}} - \mathbf{y}^{\mathrm{s}}) \delta_d(t - t_a) \tag{3.19}$$

where $G(\mathbf{x}^{\mathrm{o}}, \mathbf{y}^{\mathrm{s}}, t)$ is the Green's function, $\mathbf{x}^{\mathrm{o}}$ means a coordinate of the observer and $\mathbf{y}^{\mathrm{s}}$ is a coordinate of the source. On the right-hand side there are two Dirac functions. The first is spatial dependent, whereas the latter one is time dependent. The term $t_a$ represents time when the sound is activated, hence if $t < t_a$ then $G(\mathbf{x}^{\mathrm{o}}, \mathbf{y}^{\mathrm{s}}, t) = 0$.

The simple equation of a free field Green's function of the wave equation, representing the solution without any obstacles, is dependent mainly on the distance between the observer and source, i.e. $|\mathbf{x}^{\mathrm{o}} - \mathbf{y}^{\mathrm{s}}|$

$$G(\mathbf{x}^{\mathrm{o}}, \mathbf{y}^{\mathrm{s}}, t) = \frac{1}{4\pi|\mathbf{x}^{\mathrm{o}} - \mathbf{y}^{\mathrm{s}}|}\delta_d\left(t - t_a - \frac{|\mathbf{x}^{\mathrm{o}} - \mathbf{y}^{\mathrm{s}}|}{c_0}\right). \tag{3.20}$$

The wave equation for general sound distribution $\mathcal{F}$ is in the form

$$\frac{1}{c_0^2}\frac{\partial^2 p^a}{\partial t^2} - \Delta p^a = \mathcal{F}(\mathbf{x}^{\mathrm{o}}, t), \tag{3.21}$$

where the right-hand side is a convolution

$$\mathcal{F}(\mathbf{x}^{\mathrm{o}}, t) = \int_0^T \int_{-\infty}^{\infty} \mathcal{F}(\mathbf{y}^{\mathrm{s}}, t_a)\delta_d(\mathbf{x}^{\mathrm{o}} - \mathbf{y}^{\mathrm{s}})\delta_d(t - t_a)d\mathbf{y}^{\mathrm{s}}dt_a. \tag{3.22}$$

The sound distribution is written as a superposition of impulsive point sources, which are integrated first over the whole space and second integrated over time.

The solution of acoustic pressure is

$$p^a(\mathbf{x}^{\mathrm{o}}, t) = \int_0^T \int_{-\infty}^{\infty} \mathcal{F}(\mathbf{y}^{\mathrm{s}}, \tau)G(\mathbf{x}^{\mathrm{o}}, \mathbf{y}^{\mathrm{s}}, t - t_a)d\mathbf{y}^{\mathrm{s}}dt_a, \tag{3.23}$$

where the Green's function from (3.20) is inserted into (3.23). The final product is written as

$$p^a(\mathbf{x}^{\mathrm{o}}, t) = \frac{1}{4\pi}\int_0^T \int_{-\infty}^{\infty} \frac{\mathcal{F}(\mathbf{y}^{\mathrm{s}}, t_a)}{|\mathbf{x}^{\mathrm{o}} - \mathbf{y}^{\mathrm{s}}|}\delta_d\left(\overbrace{t - t_a - \frac{|\mathbf{x}^{\mathrm{o}} - \mathbf{y}^{\mathrm{s}}|}{c_0}}^{RT}\right)d\mathbf{y}^{\mathrm{s}}dt_a, \tag{3.24}$$

where the term in the bracket (RT) is called retarded time. If RT is zero then the final form of the general source distribution is

$$p^a(\mathbf{x}^{\mathrm{o}}, t) = \frac{1}{4\pi}\int_{-\infty}^{\infty} \frac{\mathcal{F}\left(\mathbf{y}^{\mathrm{s}}, t - \frac{|\mathbf{x}^{\mathrm{o}} - \mathbf{y}^{\mathrm{s}}|}{c_0}\right)}{|\mathbf{x}^{\mathrm{o}} - \mathbf{y}^{\mathrm{s}}|}\mathrm{d}\mathbf{y}^{\mathrm{s}}; \tag{3.25}$$

integrated over the whole space with respect to the absolute value of the distance (observer-source).

Right-hand sides of (3.21) can represent well-known multipole sound sources (Howe, 2014):

- A monopole source term

$$\mathcal{F}(\mathbf{x}, t) = \rho_0\frac{\partial q}{\partial t} \tag{3.26}$$

induced by the volumetric flow $q(\mathbf{x}, t)$, which could be in example volume flow during closing and opening the glottis.

- A dipole source term

$$\mathcal{F}(\mathbf{x},t) = \boldsymbol{\nabla}\cdot(\mathbf{f}(\mathbf{x},t)\delta_d(\mathbf{x})) = \frac{\partial}{\partial x_j} f_j(\mathbf{x},t), \tag{3.27}$$

where the difference against the previous sound source is hidden in $f_j$, representing a force density on a surface (or negative gradient of pressure). It could be imagined as sound distribution where the flow goes around some surface (vocal folds, ventricles, etc.).

- A quadrupole source term

$$\mathcal{F}(\mathbf{x},t) = \boldsymbol{\nabla}\cdot\boldsymbol{\nabla}\cdot\mathbb{L}^{\mathrm{LH}} = \frac{\partial^2 L_{ij}^{LH}(\mathbf{x})}{\partial x_i \partial x_j}, \tag{3.28}$$

having second spatial derivative of the arbitrary tensor $\mathbb{L}^{LH}$, called as the Lighthill tensor, which can be approximated for subsonic flow as $L_{ij}^{LH} \approx \rho_0 U_i U_j$. In this dissertation, aeroacoustic simulations based on aeroacoustic analogy is not included, unlike in (Šidlof et al., 2015; Zörner et al., 2013). Aeroacoustic simulations based on perturbation equations are discussed in this work.

### 3.1.3 Far-field approximation

Fig. 3.1 illustrates the far-field approximation of acoustic pressure $p^a(\mathbf{x}^{\mathrm{o}},t)$, assuming the condition $|\mathbf{x}^{\mathrm{o}}| \gg |\mathbf{y}^{\mathrm{s}}|$ measured from the origin of the coordinate system (point 0).

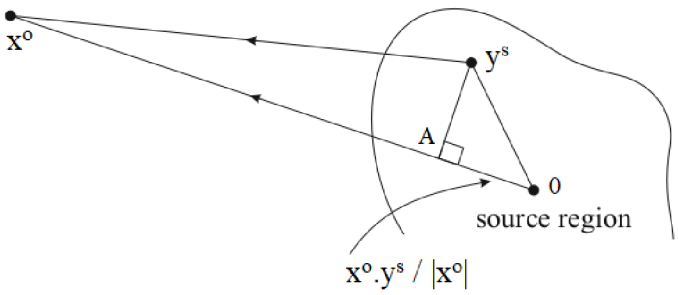


Fig. 3.1: Schema of a far-field approximation.

The computation of $p^a(\mathbf{x}^{\mathrm{o}},t)$ is executed far enough from the source region. The distance is approximated by

$$|\mathbf{x}^{\mathrm{o}} - \mathbf{y}^{\mathrm{s}}| \approx |\mathbf{x}^{\mathrm{o}}| - \frac{\mathbf{x}^{\mathrm{o}}\cdot\mathbf{y}^{\mathrm{s}}}{|\mathbf{x}^{\mathrm{o}}|}, \tag{3.29}$$

Projection of $\mathbf{x}^{\mathrm{o}}\cdot\mathbf{y}^{\mathrm{s}}/|\mathbf{x}^{o}|$ is drawn in Fig. 3.1 as a short line between A and 0. Next, (3.29) is inserted into (3.25), thus a Fraunhofer approximation of the acoustic pressure $p^a$ in the position $\mathbf{x}^{\mathrm{o}}$ can be used

$$p^a(\mathbf{x}^{\mathrm{o}},t) \approx \frac{1}{4\pi|\mathbf{x}^{\mathrm{o}}|}\int_{-\infty}^{\infty}\mathcal{F}\left(\mathbf{y}^{\mathrm{s}}, t - \frac{|\mathbf{x}^{\mathrm{o}}|}{c_0} + \frac{\mathbf{x}^{\mathrm{o}}\cdot\mathbf{y}^{\mathrm{s}}}{c_0|\mathbf{x}^{\mathrm{o}}|}\right)\mathrm{d}\mathbf{y}^{\mathrm{s}}. \tag{3.30}$$

Compared to far field approximation, the near-field approximation makes sense in cases of small distances

$$|\mathbf{x}^{\mathrm{o}} - \mathbf{y}^{\mathrm{s}}| \ll \lambda. \tag{3.31}$$

## 3.2 Acoustics and Fluid Dynamics

In this section the compressible and incompressible components of the velocity field are presented as a product of a Helmholtz decomposition

$$\mathbf{u} = \mathbf{u}^a + \mathbf{u}^v, \quad |\mathbf{u}^a| << |\mathbf{u}^v|, \tag{3.32}$$

where $\mathbf{u}^v$ is the incompressible vortical part with the property $\boldsymbol{\nabla} \cdot \mathbf{u}^v = 0$, and $\mathbf{u}^a$ is the compressible acoustic part of the velocity field. The acoustic component requires compressible fluid and is valid for low Mach numbers. The behaviour of the acoustic field is limited to be irrotational

$$\boldsymbol{\nabla} \times \mathbf{u}^a = \mathbf{0}. \tag{3.33}$$

Irrotational deformation produces no volume change, see Fig. 3.2 (left). The existence of the irrotational component leads to a decomposition of the vector field into the gradient of the scalar potential and the rotation of the vector potential

$$\mathbf{u} = \mathbf{u}^a + \mathbf{u}^v = -\boldsymbol{\nabla}\psi^a + \boldsymbol{\nabla} \times \mathbf{a}^v, \tag{3.34}$$

and getting the following property

$$\boldsymbol{\nabla} \cdot (\mathbf{u}^a + \mathbf{u}^v) = -\boldsymbol{\nabla} \cdot \boldsymbol{\nabla}\psi^a + \underbrace{\boldsymbol{\nabla} \cdot \boldsymbol{\nabla} \times \mathbf{a}^v}_{=0} = -\Delta\psi^a, \tag{3.35}$$

where the scalar potential $\psi^a$ is associated with the fluid compressibility ($\boldsymbol{\nabla} \cdot \mathbf{u} \neq 0$). This leads to the property that the volumetric rate of expansion $\boldsymbol{\nabla} \cdot \mathbf{u}$ is proportional to the isotropic expansion, see Fig. 3.2 (middle). Afterward, the rigid-body rotation is ensured, see Fig. 3.2 (right), due to the vortical flow structures which are described by the vorticity

$$\boldsymbol{\omega} = \boldsymbol{\nabla} \times (\mathbf{u}^a + \mathbf{u}^v) = \underbrace{-\boldsymbol{\nabla} \times \boldsymbol{\nabla}\psi^a}_{=0} + \boldsymbol{\nabla} \times \boldsymbol{\nabla} \times \mathbf{a}^v. \tag{3.36}$$

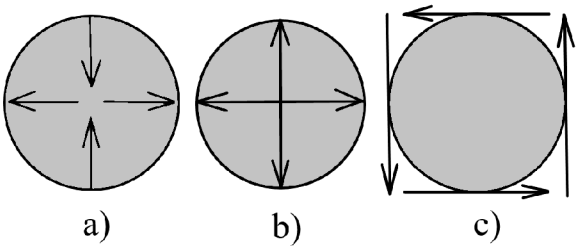


Fig. 3.2: Decomposition of the flow field. Deformation shapes: a) irrotational deformation, b) isotropic expansion and c) rigid-body rotation.

## 3.3 Aeroacoustic models

In this dissertation is used a hybrid method based on the incompressible flow computation and utilizing a perturbation ansatz to obtain perturbation equations for the aeroacoustic simulation. The word *ansatz* comes from German and means *approach*. Before we get into the perturbation equations, the perturbation ansatz will be presented first; applied on the linearized Euler equations (LEE)

$$\frac{\mathrm{D}\rho}{\mathrm{D}t} + \rho\boldsymbol{\nabla}\cdot\mathbf{u} = 0, \tag{3.37}$$

$$\rho\frac{\mathrm{D}\mathbf{u}}{\mathrm{D}t} + \boldsymbol{\nabla}p = \mathbf{0}, \tag{3.38}$$

that describe non-viscous compressible flow, neglecting viscous and heat conduction terms. The field variables $(\rho, \mathbf{u}, p)$ are decomposed into the temporal mean component $(\cdot)_0$ and perturbed fluctuating component $(\cdot)'$

$$p = p_0(\mathbf{x}) + p'(\mathbf{x},t), \quad \rho = \rho_0(\mathbf{x}) + \rho'(\mathbf{x},t), \quad \mathbf{u} = \mathbf{u}_0(\mathbf{x}) + \mathbf{u}'(\mathbf{x},t), \tag{3.39}$$

leading to the general form of LEE. The conservation of mass

$$\frac{\partial\rho'}{\partial t} + \mathbf{u}_0\cdot\boldsymbol{\nabla}\rho' + \mathbf{u}'\cdot\boldsymbol{\nabla}\rho_0 + \rho_0(\boldsymbol{\nabla}\cdot\mathbf{u}') + \rho'(\boldsymbol{\nabla}\cdot\mathbf{u}_0) = 0 \tag{3.40}$$

and conservation of momentum

$$\frac{\partial\mathbf{u}'}{\partial t} + (\mathbf{u}_0\cdot\boldsymbol{\nabla})\mathbf{u}' + (\mathbf{u}'\cdot\boldsymbol{\nabla})\mathbf{u}_0 + \frac{1}{\rho_0}\boldsymbol{\nabla}p' - \frac{1}{\rho_0^2}\boldsymbol{\nabla}(p_0\rho') = \mathbf{0} \tag{3.41}$$

equations, neglecting conductivity, can be written. (3.41) should not be confused with the decomposition $(\cdot)_0 + (\cdot)^a$ in (3.1), which leads to first order differential equations known as the conservation equations of linear acoustics. The fluctuating density $\rho'$ was introduced by Meecham and Ford (1958), and Blokhintsev (1956); Ribner (1962) formulated the fluctuating pressure $p'$ as a sum of a 'pseudosound' pressure (near-field) $p^{(0)}$ and an 'acoustic' pressure (far-field) $p^{(1)}$. In contrast to Ribner (1962), the fluctuating component is decomposed by Hardin and Pope (1993) with usage of the viscous/acoustic splitting technique

$$p = p^{ic}(\mathbf{x},t) + p'(\mathbf{x},t), \quad \rho = \rho_0 + \rho_1(\mathbf{x},t) + \rho'(\mathbf{x},t), \quad \mathbf{u} = \mathbf{u}^{ic}(\mathbf{x},t) + \mathbf{u}'(\mathbf{x},t), \tag{3.42}$$

where $\mathbf{u}, p$ and $\rho$ are set of compressible variables, $(\cdot)^{ic}$ are incompressible values, $(\cdot)'$ are perturbations of the system, the term $\rho_1(\mathbf{x},t)$ is referred by Hardin and Pope (1993) as a density correction and ensures constant entropy in the fluid and $\rho_0+\rho_1$ is called 'corrected' incompressible density. These decomposed variables can be inserted into the mass and momentum equations (3.40) and (3.41), and the system is closed with the equation of state $p'(\rho')$.

### 3.3.1 Perturbed compressible equations (PCE)

The primed variables $(\cdot)'$ have been described as a difference between the compressible and incompressible solution in the near field (Hardin and Pope, 1993), where the coupling effect plays a fundamental role. Seo and Moon (2005) introduced PCE for handling near-field coupling effects. The coupling effect in the near field is investigated by the perturbed vorticity $\boldsymbol{\omega'}$, in

$$\boldsymbol{\omega} = \boldsymbol{\omega}^{ic} + \boldsymbol{\omega'}, \tag{3.43}$$

where $\boldsymbol{\omega}^{ic}$ is the incompressible vorticity term. Seo and Moon (2005) derived PCE by extracting the incompressible flow equations from their compressible counterparts, leading to the conservation of mass

$$\frac{\partial \rho'}{\partial t} + \mathbf{u} \cdot \boldsymbol{\nabla} \rho' + \rho \boldsymbol{\nabla} \cdot \mathbf{u}' = 0 \tag{3.44}$$

and the conservation of momentum equations

$$\frac{\partial \mathbf{u}'}{\partial t} + \mathbf{u} \cdot \boldsymbol{\nabla} \mathbf{u}' + \frac{1}{\rho} \boldsymbol{\nabla} p' + \mathbf{u}' \cdot \boldsymbol{\nabla} \mathbf{u}^{ic} + \frac{\rho'}{\rho} \frac{\mathrm{D}\mathbf{u}^{ic}}{\mathrm{D}t} = \frac{1}{\rho} \boldsymbol{\nabla} \cdot \tau', \tag{3.45}$$

where the tensor $\tau'$ represents perturbed viscous stresses (difference between incompressible and compressible viscous stresses). At cases with low Mach number the perturbed vorticity $\boldsymbol{\omega'}$ is negligible, due to a minor effect on the sound field, and also, what is essential, introduces a grid dependency. Therefore, (Seo and Moon, 2006) reformulated PCE into the equation suppressing $\boldsymbol{\omega'}$ and ensuring grid independence - linear PCE. The linear PCE is written by the conservation of mass

$$\frac{\partial \rho'}{\partial t} + \mathbf{u}^{ic} \cdot \boldsymbol{\nabla} \rho' + \rho^{ic} \boldsymbol{\nabla} \cdot \mathbf{u}' = 0 \tag{3.46}$$

and by the conservation of momentum equations

$$\frac{\partial \mathbf{u}'}{\partial t} + \boldsymbol{\nabla} \left( \mathbf{u}^{ic} \cdot \mathbf{u}' \right) + \frac{1}{\rho^{ic}} \boldsymbol{\nabla} p' = -(\boldsymbol{\omega}^{ic} \times \mathbf{u}') - (\boldsymbol{\omega}' \times \mathbf{u}^{ic}) - \frac{\rho'}{\rho^{ic}} \frac{\mathrm{D}\mathbf{u}^{ic}}{\mathrm{D}t} + \frac{1}{\rho^{ic}} \boldsymbol{\nabla} \cdot \tau'. \tag{3.47}$$

This approach was used in simulations of human phonation (Bae and Moon, 2008).

### 3.3.2 Acoustic Perturbation Equations (APE)

The acoustic perturbation equations are based on the decomposition introduced by Ewert and Schröder (2003)

$$\mathbf{u} = \mathbf{u}_0(\mathbf{x}) + \mathbf{u}'(\mathbf{x}, t) = \mathbf{u}_0(\mathbf{x}) + \mathbf{u}^v(\mathbf{x}, t) + \mathbf{u}^a(\mathbf{x}, t), \tag{3.48}$$

where $\mathbf{u}^v$ is the vortical (solenoidal) velocity fluctuation and $\mathbf{u}^a$ is the acoustic (irrotational) velocity fluctuation. The solenoidal component of the velocity field $\mathbf{u}^v$ plays no role in sound generation, but it has an important role in the energy transfer across turbulent eddies, since the vorticity fluctuations are fundamental in the turbulent motion. On the other hand, the irrotational component of the velocity field $\mathbf{u}^a$ produces the sound mode and cannot produce vorticity mode (Chu and Kovásznay, 1958).

This decomposition is used in APE-x equations. The APE-1 formulation is written with $p'$ and $\mathbf{u}^a$ terms on the left-hand sides

$$\frac{\partial p'}{\partial t} + c_0^2 \boldsymbol{\nabla} \cdot \left( \rho_0 \mathbf{u}^a + \mathbf{u}_0 \frac{p'}{c_0^2} \right) = c_0^2 \Big( - \boldsymbol{\nabla} \rho \cdot \mathbf{u}^v + \frac{\rho_0}{c_\mathrm{p}} \frac{\mathrm{D}s'}{\mathrm{D}t} \Big), \tag{3.49}$$

and

$$\frac{\partial \mathbf{u}^a}{\partial t} + \boldsymbol{\nabla}(\mathbf{u}_0 \cdot \mathbf{u}^a) + \boldsymbol{\nabla}\left( \frac{p'}{\rho_0} \right) = \boldsymbol{\nabla} q_\mathrm{vel} + \boldsymbol{\nabla} q_\mathrm{vor} + T' \boldsymbol{\nabla} s_0 - s' \boldsymbol{\nabla} T_0, \tag{3.50}$$

where on the right-hand sides are entropy ($s'$, $s_0$), temperature ($T'$, $T_0$), velocity source terms $q_\mathrm{vel}$ and vortical source terms $q_\mathrm{vor}$. For incompressible flow and low Mach number cases the velocity sound term $q_\mathrm{vel}$ is computed from

$$q_\mathrm{vel} \approx \frac{\boldsymbol{\nabla} (p^{ic})'}{\rho_\infty}. \tag{3.51}$$

### 3.3.3 Perturbed Convective Wave Equation (PCWE)

The APE-2 form for isothermal and low Mach numbers can be written as a system of three partial differential equations (Hüppe et al., 2014)

$$\frac{\partial \rho'}{\partial t} + \boldsymbol{\nabla} \cdot (\rho' \mathbf{u}_0 + \rho_0 \mathbf{u}^a) = 0, \tag{3.52}$$

$$\rho_0 \frac{\partial \mathbf{u}^a}{\partial t} + \rho_0 \boldsymbol{\nabla}(\mathbf{u}_0 \cdot \mathbf{u}^a) + \boldsymbol{\nabla} p' = \mathbf{0}, \tag{3.53}$$

$$\frac{\partial p^a}{\partial t} - c_0^2 \frac{\partial \rho'}{\partial t} = - \frac{\partial p^{ic}}{\partial t}, \tag{3.54}$$

where the last equation has a source term. Combining (3.52), (3.54) and the equation of state $\rho' = p'/c_0^2$ leads (after some manipulation) to

$$\frac{1}{c_0^2} \left( \frac{\partial p^a}{\partial t} + \mathbf{u}_0 \cdot \boldsymbol{\nabla} p' \right) + \rho_0 \boldsymbol{\nabla} \cdot \mathbf{u}^a = - \frac{1}{c_0^2} \frac{\partial p^{ic}}{\partial t}, \tag{3.55}$$

and employing $p' = p^{ic} + p^a$ the form results in

$$\frac{1}{c_0^2} \left( \frac{\partial p^a}{\partial t} + \mathbf{u}_0 \cdot \boldsymbol{\nabla} p^a \right) + \rho_0 \boldsymbol{\nabla} \cdot \mathbf{u}^a = - \frac{1}{c_0^2} \left( \frac{\partial p^{ic}}{\partial t} + \mathbf{u}_0 \cdot \boldsymbol{\nabla} p^{ic} \right). \tag{3.56}$$

Next, (3.53) and (3.56) are modified. (3.56) is differentiated with respect to time, on (3.53) is taken a divergence, and finally mean flows are neglected; after modifications the equations result in the exact reformulation of APE-2

$$\frac{1}{c_0^2} \frac{\partial^2 p^a}{\partial t^2} - \boldsymbol{\nabla} \cdot \boldsymbol{\nabla} p^a = - \frac{1}{c_0^2} \frac{\partial^2 p^{ic}}{\partial t^2}. \tag{3.57}$$

If the relation $\mathbf{u}^a = -\boldsymbol{\nabla} \psi^a$ is used in (3.53)

$$\rho_0 \frac{\partial (-\nabla \psi^a)}{\partial t} + \rho_0 \nabla (\mathbf{u}_0 \cdot (-\nabla \psi^a)) + \nabla p^a = \mathbf{0}, \tag{3.58}$$

then

$$\nabla\left(\rho_0\frac{\partial\psi^a}{\partial t}+\rho_0\mathbf{u}_0\cdot\nabla\psi^a-p^a\right)=\mathbf{0}. \tag{3.59}$$

The argument of the gradient is a constant, which can be set to zero, and results in the acoustic pressure

$$p^a=\rho_0\frac{\mathrm{D}\psi^a}{\mathrm{D}t}=\rho_0\frac{\partial\psi^a}{\partial t}+\rho_0\mathbf{u}_0\cdot\nabla\psi^a. \tag{3.60}$$

Now, (3.56) can be rewritten using the substantial derivative to

$$\frac{\mathrm{D}p^a}{\mathrm{D}t}+\rho_0c_0^2\boldsymbol{\nabla}\cdot\mathbf{u}^a=-\frac{\mathrm{D}p^{ic}}{\mathrm{D}t}, \tag{3.61}$$

and finally the relation (3.60) is inserted into (3.61), using $\mathbf{u}^a=-\boldsymbol{\nabla}\psi^a$ and multiplied by $1/\rho_0c_0^2$; a scalar-valued partial differential equation called Perturbed Convective Wave Equation (PCWE) published first by Hüppe et al. (2014) is obtained

$$\frac{1}{c_0^2}\frac{\mathrm{D}^2\psi^a}{\mathrm{D}t^2}-\nabla\cdot\nabla(\psi^a)=-\frac{1}{\rho_0c_0^2}\frac{\mathrm{D}p^{ic}}{\mathrm{D}t}. \tag{3.62}$$

The vector-valued APE-2 has been reformulated into the scalar PCWE, which can spare computational resources avoiding the vector form. In this dissertation PCWE was used in all cases, while following should be remembered:

- The sound sources are discussed in terms of $\mathrm{D}p^{ic}/\mathrm{D}t$, i.e. in dimension [Pa/s].
- The wave propagation (3.62) contains the factor $-1/(\rho_0c_0^2)=-1/(1.025\cdot343.25^2)=-0.0000087\ \mathrm{ms^2/kg}$.
- From the solution of equation (3.62), i.e. $\psi^a$, the acoustic pressure $p^a$ [Pa] is calculated according to (3.60). The convective term $\rho_0\mathbf{u}_0\cdot\nabla\psi^a$ contributes only a minor part to the solution, and thus $p^a=\rho_0\partial\psi^a/\partial t$ is computed.

Benefits of PCWE are evident: faster computation with a scalar unknown, lower memory requirements compared to APE-x, includes convection inside the wave operator and solves the acoustic quantity compared to Lighthill's analogy (Lighthill, 1952).

## 3.4 Geometry and mesh

Fig. 3.3 illustrates the geometry used for aeroacoustic simulations, where from the left side are: the PML layer at inlet (dark green), larynx (red), vocal tract (purple) and the radiation zone protected by PML (green hollow cube). PML (Perfectly matched layer) is a technique published first by Berenger (1994). The original method was modified by Kaltenbacher et al. (2013) by adding damping layers to guarantee that no wave reflections occur at boundaries.

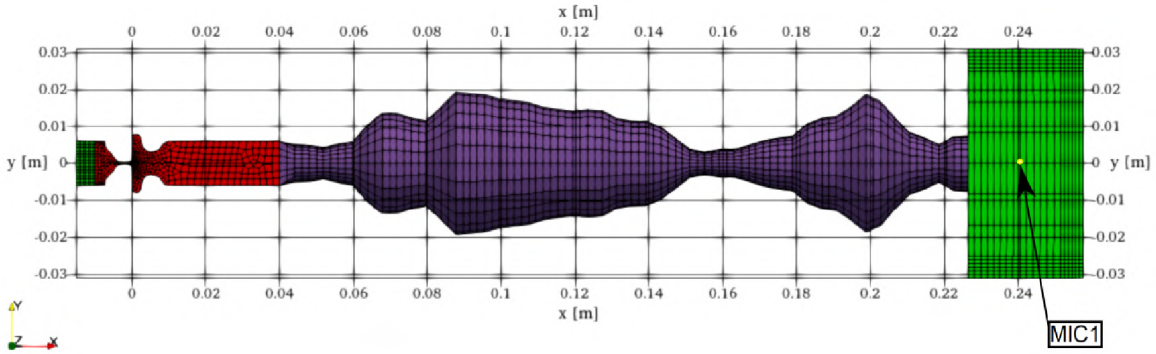


Fig. 3.3: Geometry and mesh representation for the aeroacoustic simulation. This vocal tract is in the shape for vowel /u/.

The geometry of the vocal tract was modeled from frustums (0.397 cm long) concatenated one after another. The shape of the frustums was defined according to the vocal tract area function measured by magnetic resonance imaging (Story et al., 1996).

The vocal tract was conformally attached to the larynx. The connection is formed by two layers of hexahedral cells, with minor influence on wave propagation. The right edge of the vocal tract was attached to the downstream free-field, where at distance 1 cm from the end of the vocal tract a microphone "MIC1" was placed.

In this work five geometric models of vocal tracts were created. The models correspond to vowels /u, i, ɑ, o, æ/. Lasota et al. (2021) discussed /u, i/, where the vocal tracts were relatively similar in terms of surface area function, hence extra vocal tracts for /ɑ, o, æ/ were built, see Fig. 3.4.

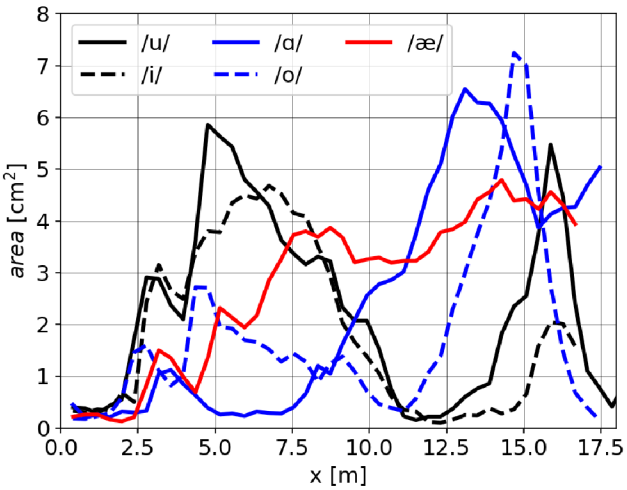


Fig. 3.4: Surface area function for the each geometrical segment of the used vocal tract. The origin refers to $x = 0.04$ m in Fig. 3.3.

For some vowels, a longer vocal tract is characteristic and thus it is necessary to use a higher number of segments. Tab. 3.1 lists the lengths of vocal tracts of five English vowels.

Tab. 3.1: List of used vocal tracts (VT).

| **Phonetic symbol** | **VT length** [m] | **Nb. of segments** | **Example of use** |
|---|---|---|---|
| /u/ | 0.1825 | 46 | who [hu:] |
| /i/ | 0.1667 | 42 | heed [hi:d] |
| /ɑ/ | 0.1746 | 44 | lock [lɑk] |
| /o/ | 0.1746 | 44 | rock [rok] |
| /æ/ | 0.1667 | 42 | have [hæv] |

As mentioned before, the shape parameters of vocal tracts came from the study provided by Story et al. (1996). The study subject was the author of the paper himself, 29-years-old male, 66 kg, 170 cm, a native of the Midwestern United States, no history of voice disorders. As the author says, the area functions of vocal tracts need to be considered an "average" shape for a particular vowel. The three-dimensional vocal tracts used in CAA simulations are shown in Figs. 3.5-3.7 and were built in Gmsh.

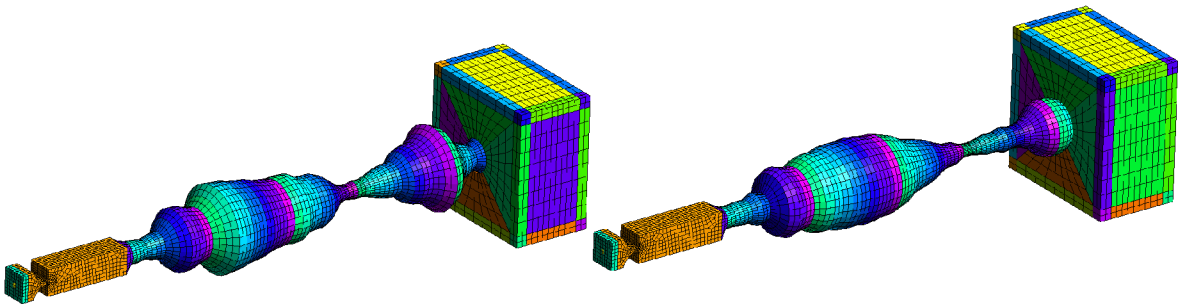

Fig. 3.5: Visualization of the acoustic mesh for /u/ (left) and /i/ (right).

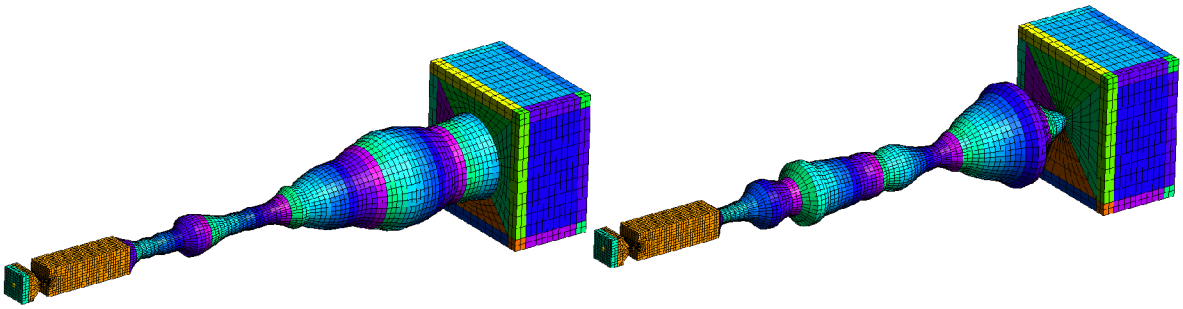

Fig. 3.6: Visualization of the acoustic mesh for /ɑ/ (left) and /o/ (right).

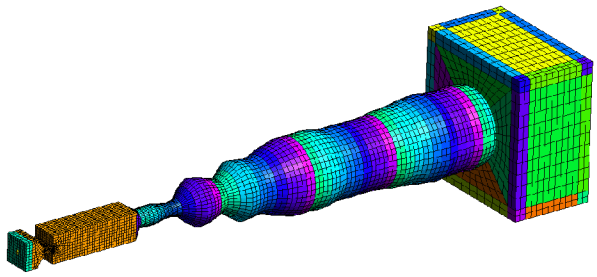

Fig. 3.7: Visualization of the acoustic mesh for /æ/.

The number of elements and nodes is listed in Tab. 3.2.

Tab. 3.2: Five computational meshes for the aeroacoustic simulation.

| **vowel** | **elements** | **nodes** |
|---|---|---|
| /u/ | 11,736 | 14,689 |
| /i/ | 11,256 | 14,077 |
| /ɑ/ | 18,818 | 23,051 |
| /o/ | 18,818 | 23,051 |
| /æ/ | 18,484 | 22,567 |

The cross-sectional view of the acoustic mesh is shown in Fig. 3.8. Hexahedral first order finite elements were used.

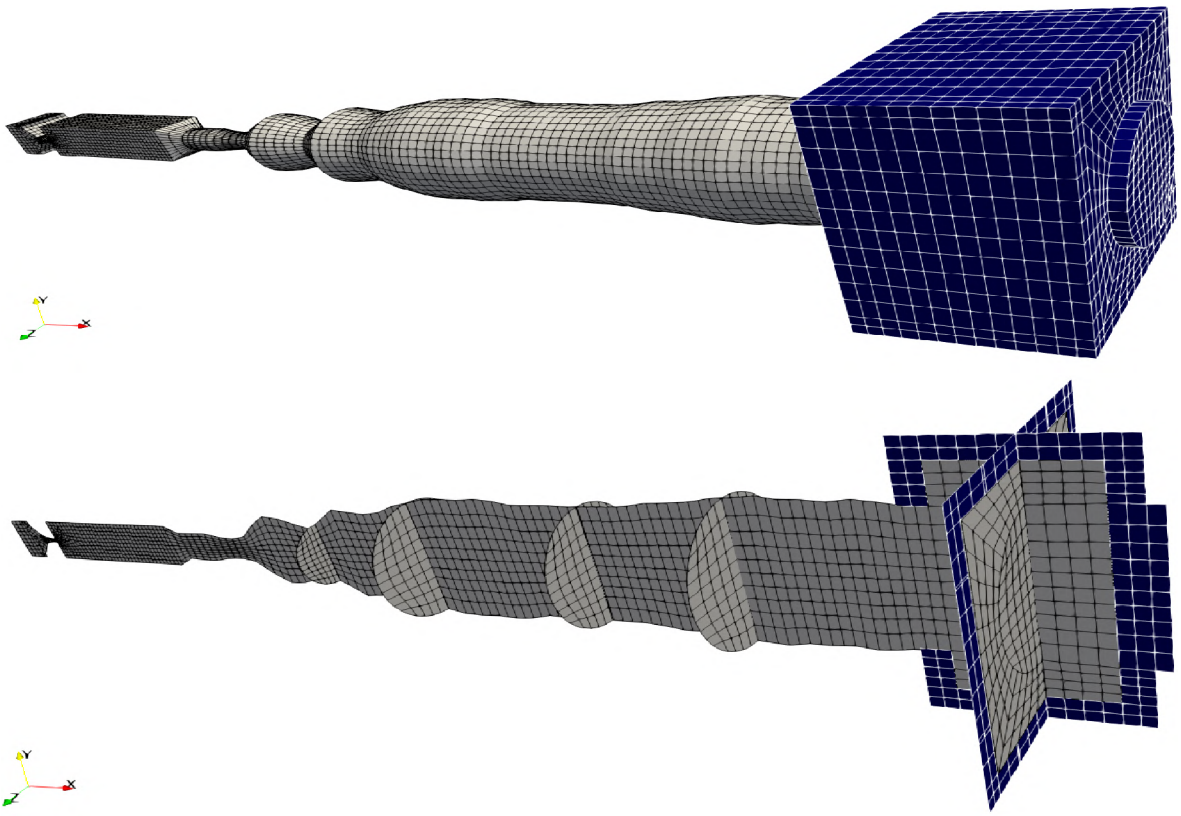

Fig. 3.8: Acoustic mesh for vowel /æ/ in transverse planes and cross-sectional view. Dark blue shaded surfaces indicate PML layers.

## 3.5 Boundary conditions

The partial differential equation (3.62) for the acoustic potential $\psi^a$, which will be solved numerically in the acoustic domain, is equipped with zero initial conditions and boundary condition

$$\boldsymbol{\nabla}\psi^a \cdot \mathbf{n} = 0, \tag{3.63}$$

where $\mathbf{n}$ is the outward unit normal. The boundary condition can be interpreted as a perfect reflection of a sound wave from a barrier, also the condition is called "sound hard". In these computations, the sound hard condition is applied at all boundaries except the inflow and outflow, where PML is used.

## 3.6 Discretization and numerical solution

An open source 3D finite element mesh generator Gmsh was used to build the computational mesh. The element length $\Delta l^a$ of the acoustic mesh and time step $\Delta t^a$ for the aeroacoustic simulation are given by estimations (Hüppe, 2012)

$$\Delta l^a \leq \frac{c_0}{20 f_{\max}} = 3.43 \text{ mm}, \quad \Delta t^a \leq \frac{1}{20 f_{\max}} = 1 \cdot 10^{-5} \text{ s}, \tag{3.64}$$

assuming that 20 linear finite elements per one acoustic wavelength are sufficient. In this case, the spatial discretization is limited by 3.43 mm and time step by $1 \cdot 10^{-5}$ s in order to resolve properly acoustic frequencies up to $f_{\max} = 5$ kHz. If the condition is not satisfied, then the acoustic results are affected by high dissipation and dispersion (Kaltenbacher, 2018). The acoustic material properties in simulations are defined by the density $\rho = 1.11703$ kg.m$^{-3}$, the bulk modulus $K = 0.1156$ MPa and the speed of sound $c_0 = 343.25$ m.s$^{-1}$.

The numerical solution (workflow) can be separated into three steps:

- The unsteady flow field in the larynx is computed in OpenFOAM on a fine CFD mesh over 20 periods of vocal fold oscillation.
- The aeroacoustic sources in the larynx are computed by OpenCFS, and conservatively interpolated on the coarse CAA mesh.
- In the last step, the wave propagation is simulated by OpenCFS on the coarse CAA mesh.

The computational time needed for one CAA simulation is much lower than for one CFD simulation, about five hours on a single CPU core compared to 34 days on 20 cores. But it should be noted that five CAA simulations have been computed on top of each of the CFD simulations. Altogether, four CFD simulations and 20 CAA simulations have been performed in this work. The conservative interpolation of the sound source from the very fine (2.2M) CFD mesh to the coarser (11k-18k) CAA mesh was performed by the cfsdat tool (part of the OpenCFS). The work of Schoder et al. (2020) contains an overview of the conservative strategies, granting a reduction of the simulation time.

## 3.7 CAA results

First part of this chapter is dedicated to aeroacoustic sources in the larynx. The sound sources can be analysed in the time or frequency domain:

- In temporal domain, spatial distributions of sound sources can be visualized at distinctive times corresponding to specific vocal fold positions.
- In the frequency domain, locations of sound sources within a specific frequency playing some role in human phonation can be highlighted - fundamental, harmonic and non-harmonic.

Second part is dedicated to the wave propagation through the vocal tract and further downstream to the far-field. Results are analysed in time and frequency domain, too:

- In the time domain, the acoustic pressure signal $p^a(t)$ is obtained from the probe located in the far field and used for voice analysis in terms of amplitudes.
- On the aeroacoustic frequency spectra, variations of sound pressure levels due to different subgrid-scale models can be exposed.

### 3.7.1 Visualization of sound sources in the time domain

The distribution of the aeroacoustic sources in the computational domain covering the larynx varies throughout the vocal fold oscillation period. Fig. 3.9 shows the aeroacoustic source field while the vocal folds are in the closed-divergent position. The jet is surrounded by spots of strong positive and negative acoustic sources related to turbulent eddies created from shear layers of the jet.

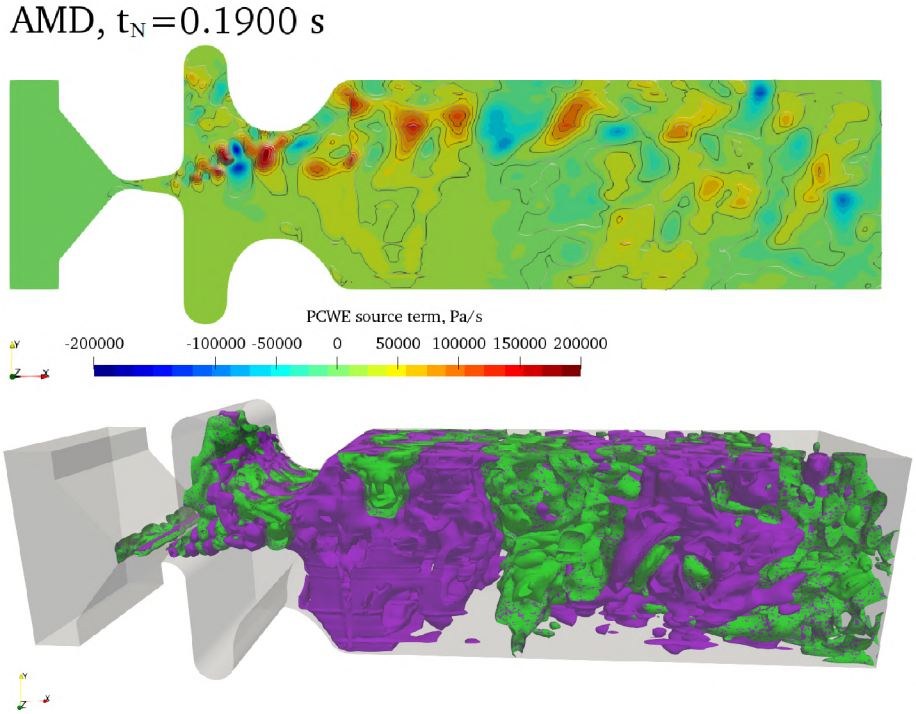


Fig. 3.9: Aeroacoustic source term ($\mathrm{D}p^{ic}/\mathrm{D}t$) from (3.62) at closed-divergent vocal folds positions during phonation. Twenty iso-surfaces in the range $\pm 2 \cdot 10^5$ Pa/s are shown (positive-purple ones, negative-green ones).

Fig. 3.10 shows the aeroacoustic sound source distribution corresponding to the closed-convergent position of vocal folds, which are visualized on the CFD mesh with closed-divergent position of vocal folds. The aeroacoustic sources computed on the moving geometry with oscillating vocal folds are mapped to a fixed geometry. This is done because the current version of the acoustic solver cannot handle moving meshes.

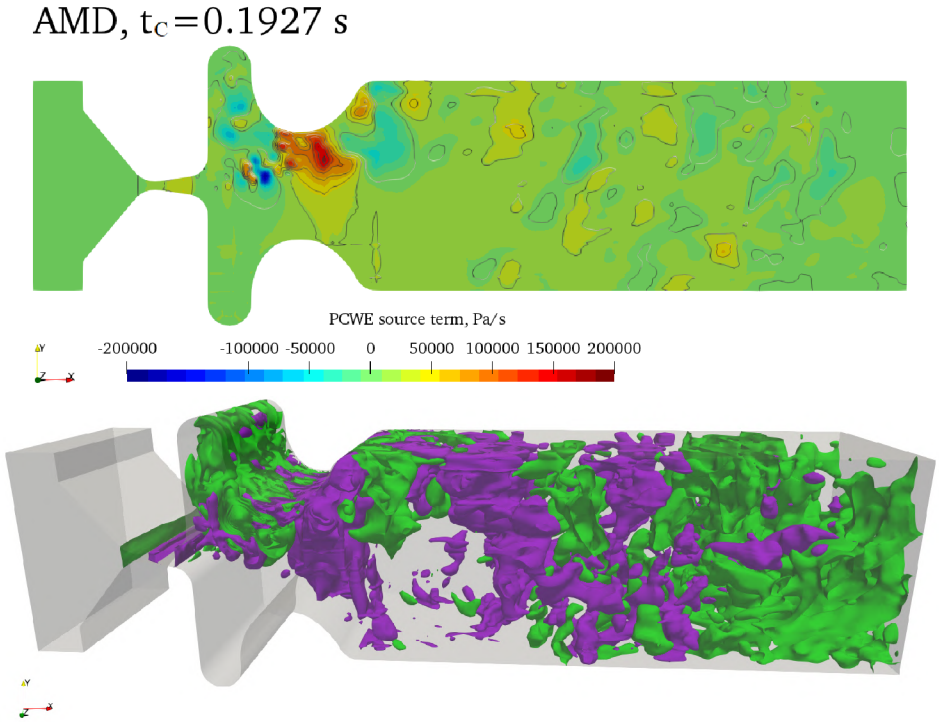


Fig. 3.10: Aeroacoustic source term ($\mathrm{D}p^{ic}/\mathrm{D}t$) computed by (3.62) at closed-convergent vocal folds positions during phonation which is mapped to the domain with closed-divergent vocal folds positions. Twenty iso-surfaces in the range $\pm 2 \cdot 10^5$ Pa/s are shown (positive-purple ones, negative-green ones).

Fig. 3.11 shows sound source distribution when vocal folds are fully open, and the results are mapped to the closed-divergent domain. A strong sound source is observed at the glottis, especially on the 2D view, while the 3D view shows preferred directions. This can be caused by the presence of high turbulent viscosity (see Fig. 2.16). Compared to adducted vocal folds, the sound sources in the larynx are stronger.

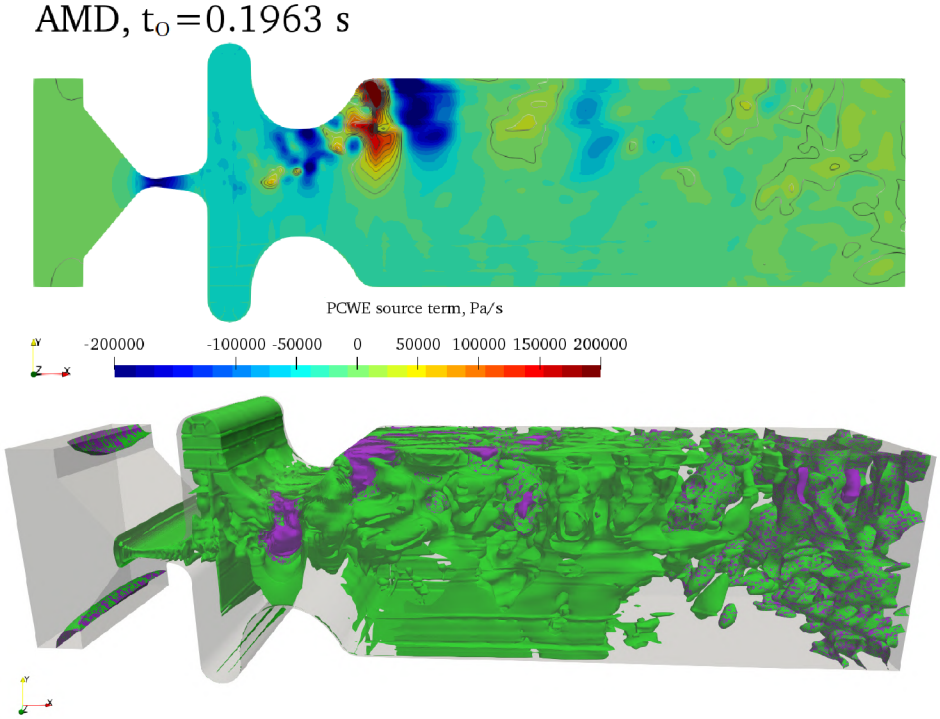


Fig. 3.11: Aeroacoustic source term ($\mathrm{D}p^{ic}/\mathrm{D}t$) computed by (3.62) at fully-open vocal folds positions during phonation which is mapped to the domain with closed-divergent vocal folds positions. Twenty iso-surfaces in the range $\pm 2 \cdot 10^5$ Pa/s are shown (positive-purple ones, negative-green ones).

It is not effective to present the sound sources in time domain for every subgrid-scale model. This will be done in the frequency domain where the comparison is more obvious.

### 3.7.2 Visualization of sound sources in the frequency domain

The conversion from the time to frequency domain was made by the field Fast Fourier Transform (field FFT), which brings useful insight into the spatial distribution of the aeroacoustic sources at distinct frequencies related somehow to human phonation.

The first row in Fig. 3.12 shows aeroacoustic sources at the fundamental frequency (frequency of vibration of the vocal folds). The strongest sources are located inside the glottis, which is consistent with the theory. Results obtained from the laminar simulation (LAM) show higher intensities than large-eddy simulations (OE, WALE and AMD). This correlates with the flow rate amplitude, which is also higher in the laminar case (see Fig. 2.7).

The second row shows the third harmonic frequency $f_2 = 300$ Hz. Aeroacoustic sources are observed within the glottis in accordance with the theory of higher harmonics. In the

laminar and WALE cases, weak aeroacoustic sources also occur in the vicinity of the jet and in the ventricular folds.

The last two rows refer to the higher harmonic frequency $f_9 = 1000$ Hz and a non-harmonic frequency $f = 1235$ Hz (randomly chosen). At these higher frequencies, the dominant aeroacoustic sources do not occur within the glottis but in the places where the fast glottal jet interacts with the ventricular folds and with the slowly moving recirculating air in the supraglottal volume.

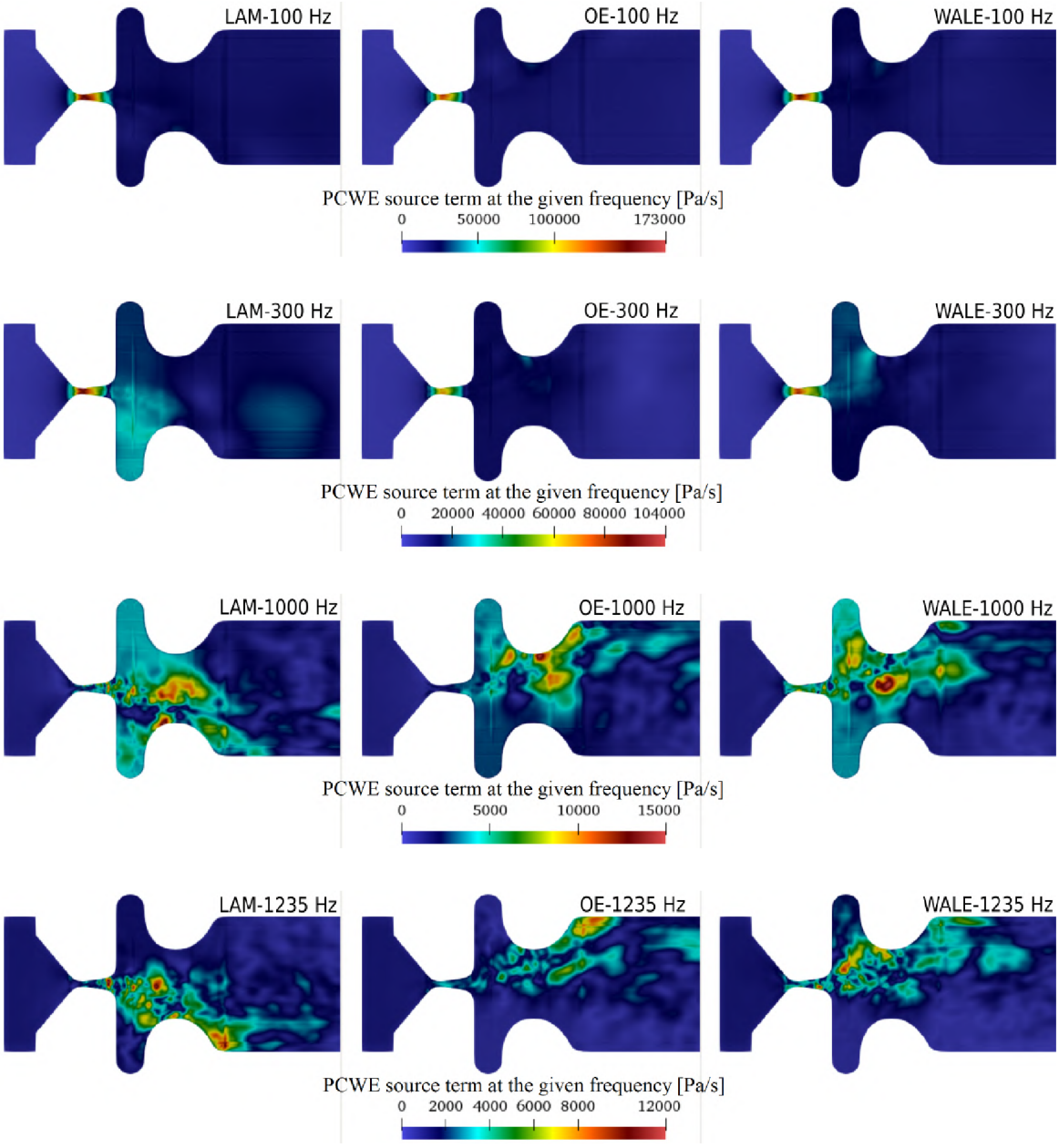


Fig. 3.12: Spatial distribution of PCWE sound sources in the mid-coronal plane at four frequencies (as a result of Fast Fourier Transform).

The visualization of sound sources based on AMD is diplayed separately in Fig. 3.13, since unlike OE and WALE the AMD is a non-standard subgrid-scale model newly

implemented into OpenFOAM by the author of this thesis. The sound source distribution at $f = 100\,\text{Hz}$ in the case based on the AMD subgrid-scale model is most similar to the simulation with OE, and the intensity of the sound sources at $f = 100\,\text{Hz}$ is also lower than with the LAM model. On the other side, the intensity of sound sources at $f = 1000\,\text{Hz}$ is 2.5-4x higher compared to the LAM, OE and WALE cases. The explanation may be hidden in the presence of higher turbulence intensity corresponding to the fully open glottis. At the higher harmonic frequency $f = 300\,\text{Hz}$ there is no evident difference among the simulations. The 2D visualization of the sound source distribution at $f = 1235\,\text{Hz}$ shows five times weaker sound sources within ventricles than at the higher harmonic frequency $f = 1000\,\text{Hz}$.

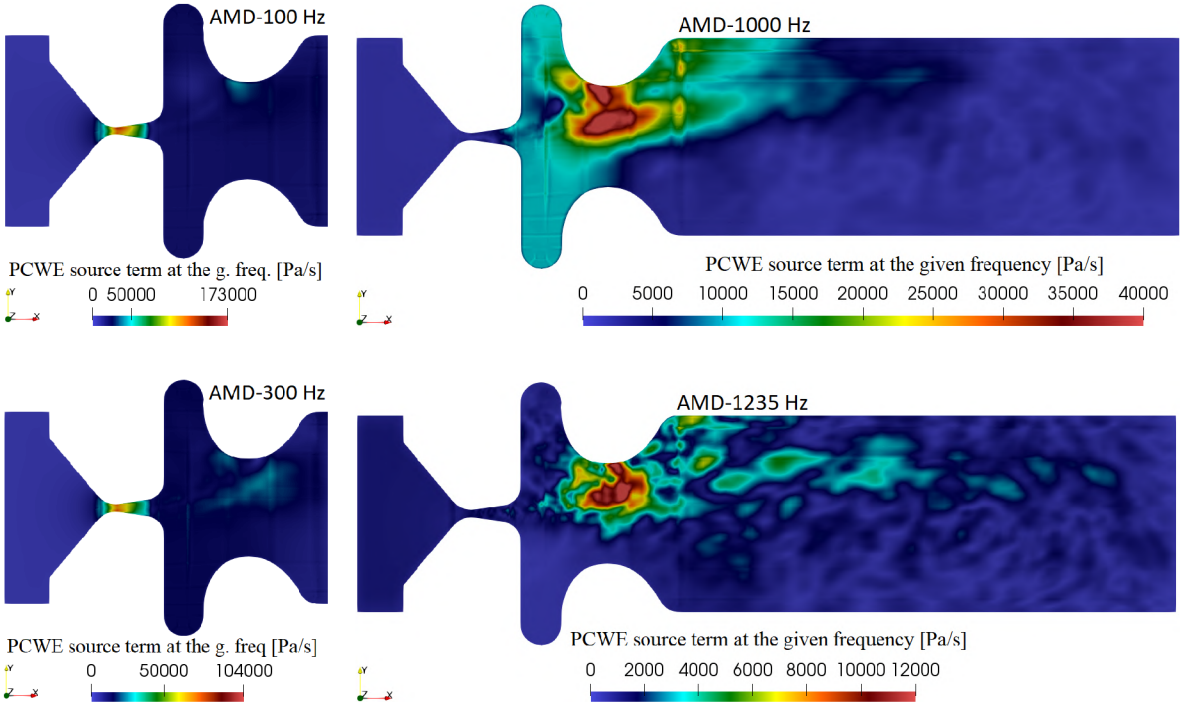


Fig. 3.13: Spatial distribution of sound sources in the mid-coronal plane at four frequencies (as a result of Fast Fourier Transform).

Fig. 3.14 shows the 3D spatial distribution of sound sources in the supraglottal volume at $f = 1000$ Hz and $f = 1235$ Hz, same as in Fig. 3.13. At the non-harmonic frequency the acoustic sources are distributed further downstream. The integrity of sound sources can be observed, along with several local sound spots at the superior (trailing) edge of vocal folds.

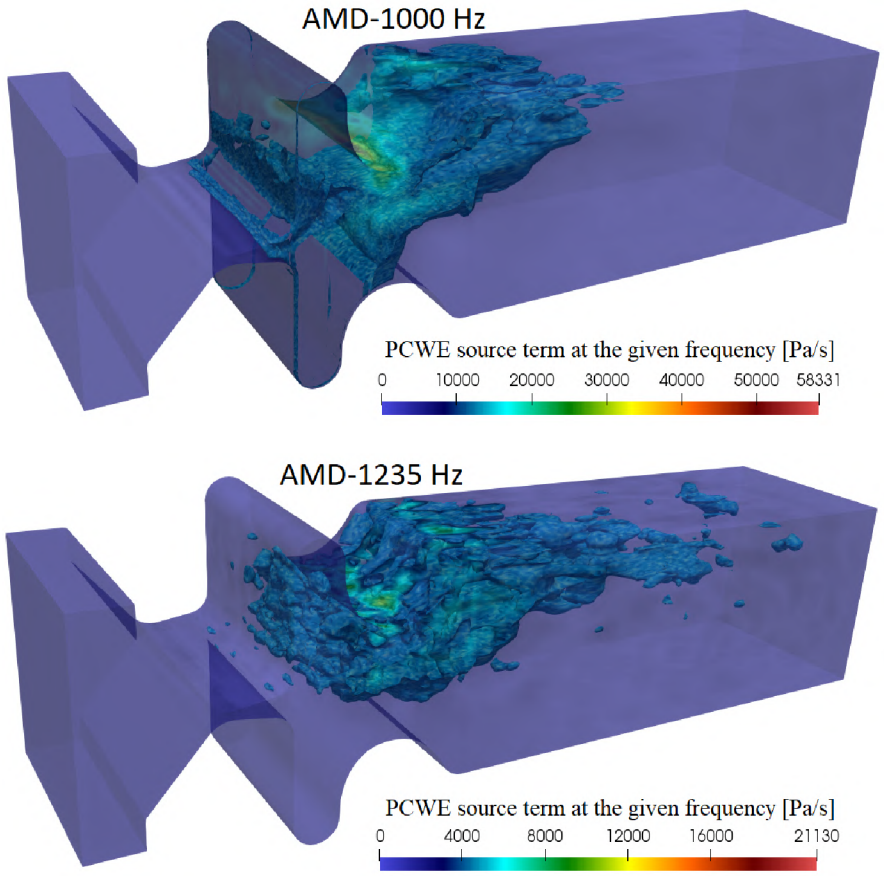


Fig. 3.14: 3D spatial distribution of the PCWE source term at the harmonic frequency $f$=1000 Hz and the non-harmonic frequency $f$ = 1235 Hz.

### 3.7.3 Wave propagation in the time domain

The wave propagation was studied based on 20 CAA simulations (five vocal tracts and four CFD simulations). In the following, the acoustic pressure fields $p^a(\mathbf{x}, t)$ will be analysed as a solution of equation (3.62) and (3.60).

Fig. 3.15 shows the acoustic field in the entire simulated domain. The usage of two color scales helps to visualize within a single figure waveforms in the radiation free field (MIC1 is located there) and 20x higher values of the acoustic pressure in the larynx and vocal tract. The probe MIC1 in the free field sampled values of $p^a(t)$. The perfectly matched damping layers (shaded by orange color in the scheme) at the inlet and around the free field ensure $p^a(t) = 0$ and non-reflecting wall.

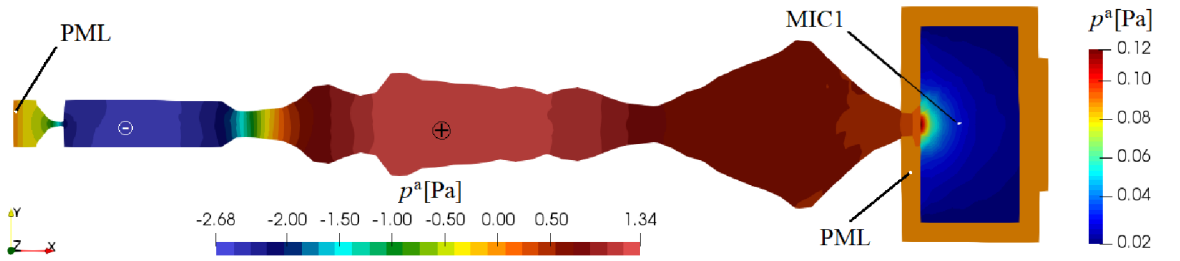


Fig. 3.15: Acoustic pressure field for vowel /ɑ/ at $t = 190$ ms. The right color scale bar corresponds only to the free field containing MIC1.

Signals $p^a(t)$ from the probe MIC1 will be discussed until the end of this work. Fig. 3.16 shows the last three periods of the vocal fold oscillation of five CAA simulations based on the AMD subgrid-scale model. The shortest and smoothest vocal tract /æ/ transferred most energy. This should be related with the front near-open unrounded character of the /æ/ vowel. On contrary, the back open unrounded vowel /ɑ/ occurs when the tongue opens the pharynx passage more gently, leading to pressure amplitudes ±0.05 Pa, compared to ±0.15 Pa for /æ/. The close-front /i/ and close-back /u/ vowels are known for the lowest amplitudes (Titze, 1994). The front vowel /i/ carries slightly more energy in amplitude than the back vowel /u/.

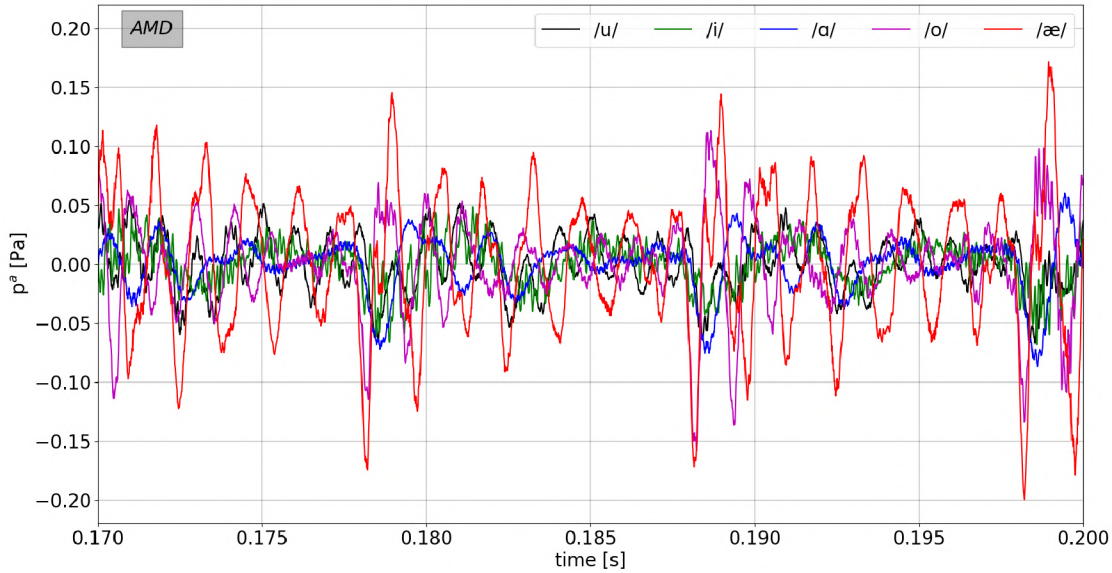


Fig. 3.16: Time history of the acoustic pressure in MIC1 for five vowels. CAA simulation based on the CFD simulation with the AMD SGS model.

The impact of the subgrid-scale model on $p^a(t)$ can be also analyzed in terms of amplitudes of $p^a(t)$ for a single vowel. Fig. 3.17 shows phonation of the close-back /u/, where the AMD case has higher amplitudes compared to others. On the contrary, the simulation of phonation of close-front vowel /i/ in Fig. 3.18 shows higher amplitudes of $p^a(t)$ computed by common subgrid-scale models.

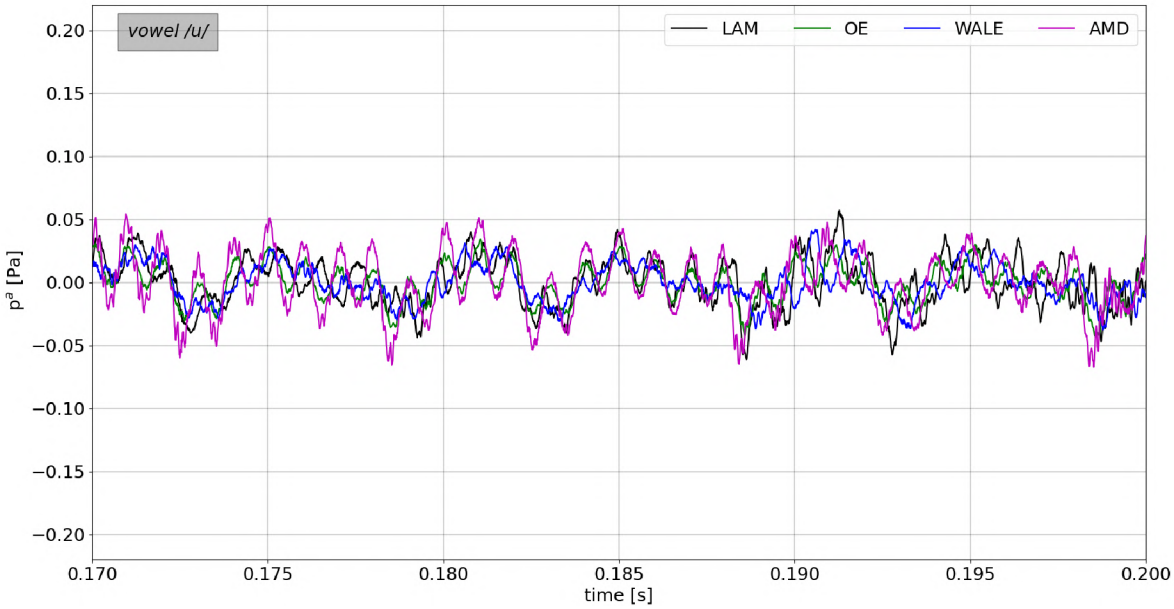


Fig. 3.17: Acoustic time signals at monitoring point MIC1 for vowel /u/.

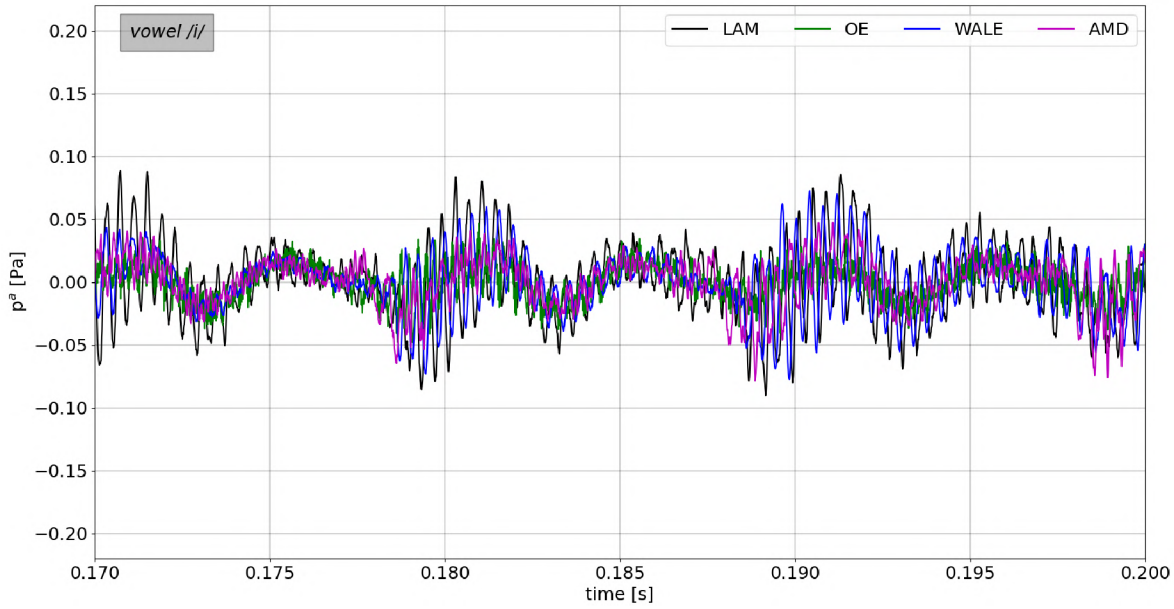


Fig. 3.18: Acoustic time signals at monitoring point MIC1 for vowel /i/.

Subsequent graphs of $p^a(t)$ plotted in the first three and last three periods of vocal fold oscillation (sorted by subgrid-scale models or by single vowels) are attached in appendix A.1-A.11.

The effective acoustic pressure is commonly measured by the sound pressure level (SPL). The SPL is defined

$$L = 20 \log_{10} \left( \frac{p^a_{\mathrm{rms}}}{p^a_{\mathrm{ref}}} \right), \tag{3.65}$$

where $p^a_{\text{ref}} = 20$ $\mu$Pa is the hearing threshold. The term $p^a_{\text{rms}}$ is the pressure root mean square value

$$p^a_{\text{rms}} = \sqrt{\frac{1}{T}\int (p^a)^2 \mathrm{d}t}. \tag{3.66}$$

Tab. 3.3 compares individual cases in terms of $L$ and $p^a_{\text{rms}}$. The SPL value of the radiated sound can be used as a measure of the acoustic energy transferred from the larynx through the vocal tract, and using this value the impact of the subgrid-scale model on aeroacoustics can be analysed. Minor differences in SPL are observed between the front open vowel /u/ and back close vowel /ɑ/. The simulations of front open/mid vowel /æ/ transferred most energy of all simulated vowels. The simulations based on the AMD model predicted the highest SPL of all vowels except the back-close /u/ and front-close /i/. This may lead to the conclusion that WALE model can transfer more energy in simulations with the so-called close vowels.

Tab. 3.3: Root mean square acoustic pressures [Pa] and sound pressure levels [dB] at MIC1 for all simulated vowels and SGS models

| Case | vowel | $p^a_{\text{rms}}$[Pa] | $L$[dB] |
|---|---|---|---|
| LAM | /u/ | 0.037184 | 65.39 |
| OE | /u/ | 0.016591 | 58.38 |
| WALE | /u/ | 0.015314 | 57.68 |
| AMD | /u/ | 0.023259 | 61.31 |
| LAM | /i/ | 0.034784 | 64.81 |
| OE | /i/ | 0.017512 | 58.85 |
| WALE | /i/ | 0.026830 | 62.55 |
| AMD | /i/ | 0.018500 | 59.32 |
| LAM | /ɑ/ | 0.016384 | 58.27 |
| OE | /ɑ/ | 0.013493 | 56.58 |
| WALE | /ɑ/ | 0.015125 | 57.57 |
| AMD | /ɑ/ | 0.023004 | 61.22 |
| LAM | /o/ | 0.041139 | 66.26 |
| OE | /o/ | 0.022411 | 60.99 |
| WALE | /o/ | 0.026176 | 62.34 |
| AMD | /o/ | 0.043374 | 66.72 |
| LAM | /æ/ | 0.045510 | 67.14 |
| OE | /æ/ | 0.023582 | 61.43 |
| WALE | /æ/ | 0.039824 | 65.98 |
| AMD | /æ/ | 0.062786 | 69.94 |

Total sound pressure levels computed at the 1 cm distance from the mouth, listed in Tab. 3.3, were computed to compare cases by energy transfer. The voice investigation at clinics is commonly performed in 15-30 cm distance from the mouth. Since the SPL value decreases by 6 dB each time the distance doubles, the signal at 30 cm would be about 30 dB lower. The whisper is defined as around 30 dB, normal conversation is about 60 dB. The results can be interpreted as a whisper, which is in full accordance with the prescribed flow boundary condition, where the pressure-driven flow was based on $P = 350\,\text{Pa}$ at $\Gamma_{in}$.

### 3.7.4 Wave propagation in the frequency domain

This section deals with frequency spectra. This kind of analysis can highlight fundamental, harmonic and non-harmonic frequencies, accompanied by background noise. The FFT analyses were performed on the signal spanning over 20 periods of the vocal fold oscillation (1 period = 10 ms = 1000 samples), and thus the frequency resolution is $\Delta f = 5$ Hz. The spectra will be analysed vowel by vowel, and in the closing of the chapter the computed formants will be compared with recorded formants obtained from natural speech recordings. The list of all SPL values at important frequencies evaluated from the spectra is attached in Tab. A.1.

*Vowel* /u/. Fig. 3.19 shows aeroacoustic spectrum based on the CFD simulation with different subgrid-scale models. SPL at fundamental frequency $f_o = 100$ Hz and higher harmonics $f_1 = 200$ Hz, $f_2 = 300$ Hz and so forth, are well visible, but SPL at $f_o$ is lower than at $f_1$ and $f_2$. Unfortunately, this trend is in contrast with the acoustic theory, meaning the oscillation of vocal folds is simultaneously the dominant frequency in the spectrum. Scientific groups (Falk et al., 2021; Schoder et al., 2020) report the same unbalance with the first harmonic $L_{f_1}$ higher than $L_{f_o}$. The second formant computed by the simulation with AMD is higher by 22% compared to the case with WALE. At the third formant, on the contrary, WALE is higher by 28% than AMD. This trend occurs only for vowels /u, ɑ/, even though the vocal tracts for /u, ɑ/ have very different shapes (see Fig. 3.7).

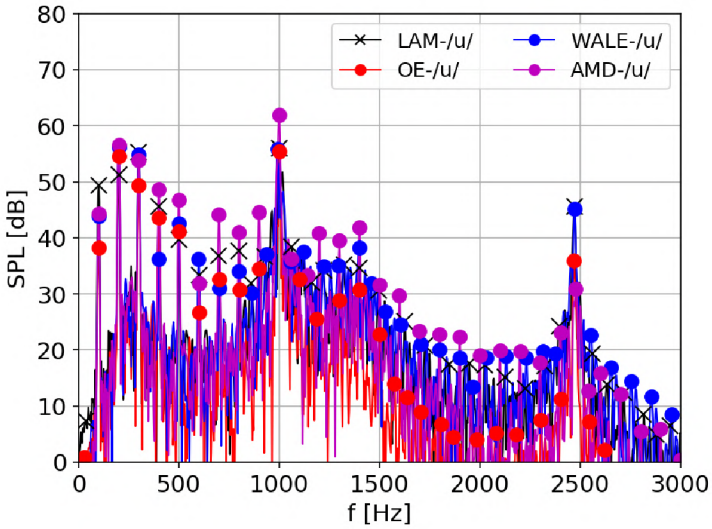


Fig. 3.19: Acoustic sound spectra from the numerical simulation of vocalization of /u/ at monitoring point MIC 1.

*Vowel* /i/. Fig. 3.20 shows the second aeroacoustic spectrum. The simulations with OE performed on vocal tracts /u, i/ predict the lowest SPL at the fundamental frequencies.

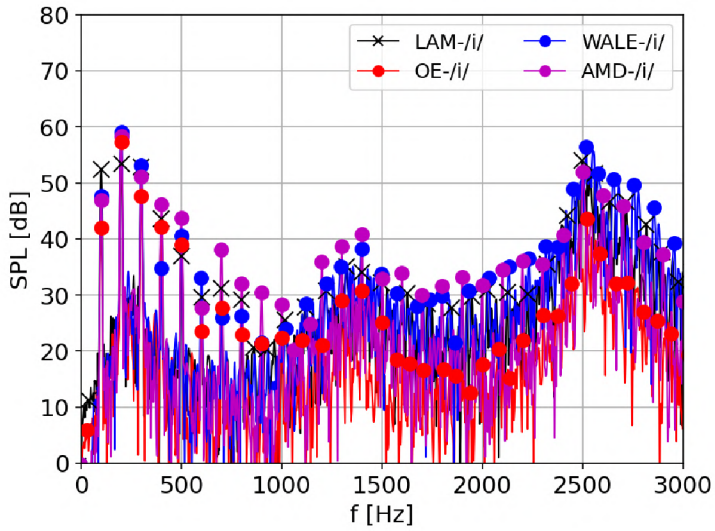


Fig. 3.20: Acoustic sound spectra from the numerical simulation of vocalization /i/ at monitoring point MIC 1.

*Vowel* /ɑ/. Fig. 3.21 shows that SPLs at fundamental frequency remain at the same level for all models. This happened only twice, in cases /ɑ, æ/ for open and mid-open vowels, when the tongue is pressed down most. The close distance between formants $F_1 - F_2$ is typical for vowels /u, ɑ, o/, but in the simulation of /ɑ/ the second formant around 1300 Hz was not detected. However, in the case of AMD, it appears that the second formant may be found. On the other hand, the third formant is clearly visible and presents the same behavior as in /u/, i.e. a 9-13 dB lower value of AMD compared to WALE and LAM.

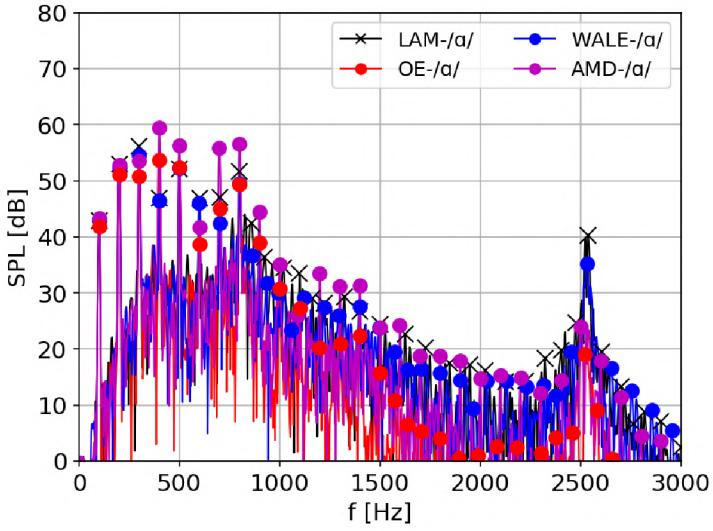


Fig. 3.21: Acoustic sound spectra from the numerical simulation of vocalization of /ɑ/ at monitoring point MIC 1.

*Vowel* /o/. Fig. 3.22 shows the aeroacoustic spectrum with the widest passage of the throat (7.25 $cm^2$) during phonation (see Fig. 3.4). The simulation with the AMD model

predicted the first formant around 900 Hz and SPL around 64 dB. At 30 cm, the value would reach 34 dB.

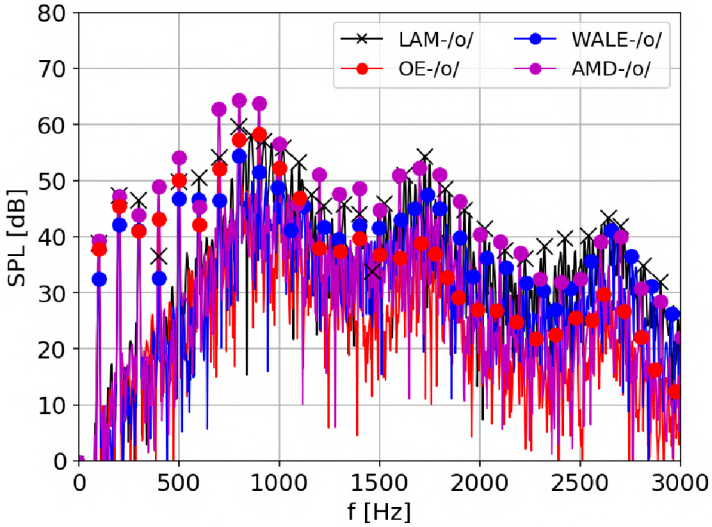


Fig. 3.22: Acoustic sound spectra from the numerical simulation of vocalization of /o/ at monitoring point MIC 1.

*Vowel* /æ/. Fig. 3.23 shows the aeroacoustic spectrum for the vocal tract /æ/, which transfers most acoustic energy – 70 dB with the AMD model, 66 dB with the WALE model (see Tab. 3.3). The first formant predicted by AMD is by 14 dB higher than the formant predicted by the WALE model. Detailed SPL values of all the formants are given in Tab. A.1. The formants in the high-frequency bandwidth are on the same level for AMD and WALE. For all vowels except /æ/, at 600 Hz was detected a significant drop in SPL.

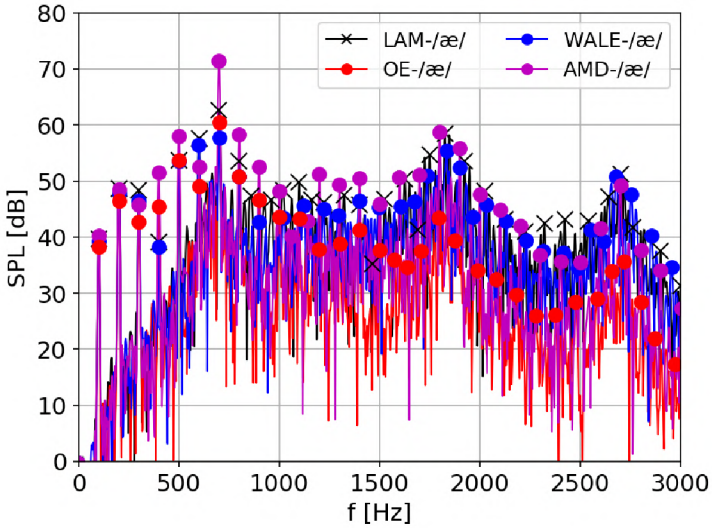


Fig. 3.23: Acoustic sound spectra from the numerical simulation of vocalization of /æ/.

Fig. 3.24 and Tab. 3.4 summarize locations of formants from previous spectra, together with the results of two investigations of human phonation obtained by measurements. The location of formants obtained from simulations is independent of the subgrid-scale

model used, and thus four simulations can be represented by one blue line. Three formant frequencies $F_1, F_2$ and $F_3$ are plotted on the y-axis as horizontal lines (blue), and compared with two in-vivo measurements published by Story et al. (1996) (black) and Ireland et al. (2015) (red). $F_1^{/o/}$ and $F_2^{/ɑ/}$ are not visible. The CAA simulations of human phonation agree relatively well with the measurements, although the extra resonant frequency at 1401 Hz in the case of the vowel /i/ is questionable.

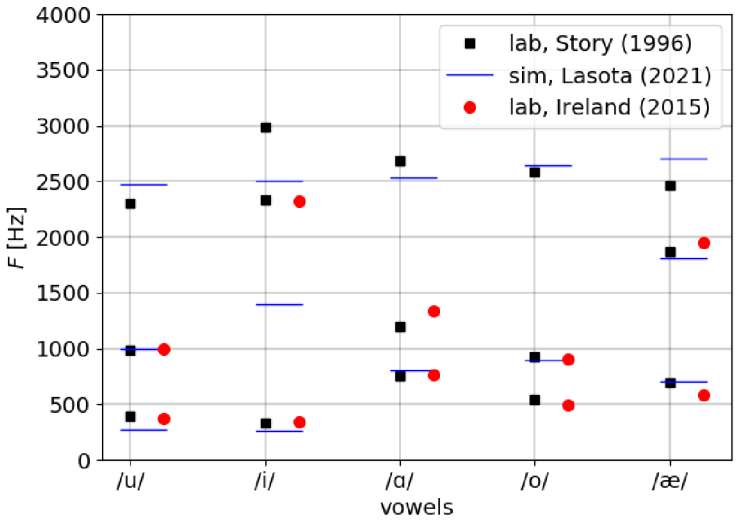


Fig. 3.24: An overview of frequency formants $F_1 - F_3$ related to the specific vowel (not always three formants are available).

Tab. 3.4: Location of formants. Values are obtained from CAA simulations (Lasota) and from recordings (Story, Ireland).

| Vowel | Formant | Lasota | Story | Ireland |
|---|---|---|---|---|
| /u/ | $F_1$ | 270 | 389 | 378 |
| | $F_2$ | 1000 | 987 | 997 |
| | $F_3$ | 2478 | 2299 | - |
| /i/ | $F_1$ | 265 | 333 | 342 |
| | $F_2$ | 1401 | 2332 | 2322 |
| | $F_3$ | 2499 | 2986 | - |
| /ɑ/ | $F_1$ | 803 | 754 | 768 |
| | $F_2$ | - | 1195 | 1333 |
| | $F_3$ | 2538 | 2685 | - |
| /o/ | $F_1$ | - | 540 | 497 |
| | $F_2$ | 900 | 922 | 910 |
| | $F_3$ | 2641 | 2584 | - |
| /æ/ | $F_1$ | 706 | 692 | 588 |
| | $F_2$ | 1805 | 1873 | 1952 |
| | $F_3$ | 2701 | 2463 | - |

Fig. 3.25 shows the formant ranges measured by Peterson and Barney (1952) together with the currently simulated formants. The simulated vowels /u, i, æ/ lie inside the measured ranges. Vowels /ɑ, o/ agree in one of the formants, which was detected, though

the other formant is unclear. The vowel tract geometry could be relatively easily modified to shift the location of formants where we need. Nevertheless, Fig. 3.25 confirms the usability of grids based on the circular vocal tracts (Story et al., 1996).

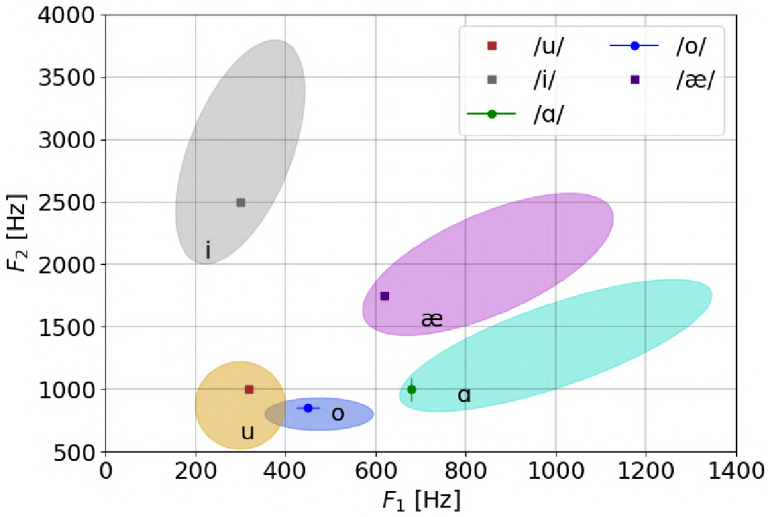


Fig. 3.25: Formant ranges measured by Peterson and Barney (1952) together with the currently simulated vowels.

## 3.8 Summary of findings

Analysis of the CAA simulations leads to the following important conclusions:

- For all vowels, the results of aeroacoustic simulations based on the AMD model have strongest SPL of higher harmonic frequencies up to about 2000 Hz. For frequencies between 2000-3000 Hz, the strongest harmonics are predicted by the WALE model.
- For all vowels, the usage of the AMD model leads to the stronger second formant, whereas the WALE model results in the stronger third formant.
- For all vowels, SPL at 100 Hz was lower than at higher harmonic frequencies. In the case with close-front and close-back vowels this might be an effect of the first formant, but in cases with mid/open and open vowels, when the first formant is far.
- Simulations of phonation including vowels /ɑ, æ/ computed higher SPL compared to vowels /u, i, o/. This could be explained by greater vocal tract passage before lips (see Fig. 3.4).
- The subgrid-scale model did not have any influence on the location of the formant frequencies.

# 4 Conclusion

Large-eddy simulations of laryngeal incompressible flow with no subgrid-scale model (LAM) and with various of subgrid-scale models were performed, namely: One-Equation (OE) (2.24), Wall-Adaptive Local-Eddy viscosity (WALE) (2.34) and the newly implemented Anisotropic Minimum-Dissipation (AMD) (2.49) model. The AMD model was tested on benchmark cases prior to use on the laryngeal flow. The chosen benchmark cases were turbulent plane channel (Chap. 2.1.5) and periodic hill (Chap. 2.1.6).

CAA simulations of the aeroacoustic sources and wave propagation during human phonation of five vowels /u, i, ɑ, o, æ/ were performed. The simulations were based on the hybrid approach using decomposition of the flow variables. The perturbed convective wave equation (3.62) was used in all cases.

Numerical results obtained from CFD and CAA simulations were discussed separately in summaries of findings (Chaps. 3.8, 2.6). The concluding assessment regarding the usage of SGS models in numerical modelling of human phonation can be formulated as follows: The OE model overpredicts the turbulent viscosity in regions where shear is dominant, i.e. in the boundary layer adjacent to the vocal folds and in the shear layers of the glottal jet (Figs. 2.17, 2.16, 2.15). The difference in glottal flow rate among the simulations is clearly induced by the subgrid-scale model, which adds the turbulent viscosity to the molecular viscosity of air and hinders the airflow in the glottis (Fig. 2.7, Tab. 2.4). The WALE model produced zero eddy viscosity in cases of pure shear flow (Figs. 2.17, 2.16, 2.15), and hence the flow simulation with WALE predicted by 5% higher maximum transglottal flow rate than AMD (Fig. 2.7, Tab. 2.4). Despite of this fact, the phonation simulation based on the AMD model transferred more energy in terms of total sound pressure level than WALE for all vowels except the front-close vowel /i/ (Tab. 3.3).

The WALE model, which is known to handle turbulent viscosity at the near-wall and high-shear regions more precisely than the OE model, resulted in higher SPLs than OE in all cases except the close-back vowel /u/ (Tab. 3.3). The OE model gives acceptable results in general, but peaks of frequency formants are hardly visible and weaker compared to the WALE or AMD model. The WALE model amplified third formants in high-frequency bandwidth most of all the models (Figs. 3.19-3.23). Hovewer, the third formant is not crucial for vowel characterization.

The AMD model seems to be a very promising successor to the WALE model in modelling laryngeal flow, since the AMD model resulted in significantly higher harmonic frequencies up to the second formant for all studied cardinal vowels (Figs. 3.19-3.23). This finding could be related to known features of the AMD model: consistency with the exact subgrid-scale stress tensor $\tau_{ij}$, no requirements on the approximation of the filter width $\Delta$ and usability on an anisotropic mesh. This thesis represents the first application of the AMD model in the field of human phonation.

# Appendices

## A.1 Tensor operations in OpenFOAM

Double dot product or double contraction of two second order tensors (A && B)

$$\begin{aligned}\mathbb{A} : \mathbb{B} = A_{ij}B_{ij} = A_{11}B_{11} + A_{12}B_{12} + A_{13}B_{13} + \\ + A_{21}B_{21} + A_{22}B_{22} + A_{23}B_{23} + \\ + A_{31}B_{31} + A_{32}B_{32} + A_{33}B_{33}.\end{aligned} \tag{A.1}$$

---

Inner dot product of two second order tensors (A & B)

$$\mathbb{A} \cdot \mathbb{B} = A_{ik}B_{kj}. \tag{A.2}$$

---

Trace of a second rank tensor (T && I, or tr(T))

$$\mathrm{tr}(\mathbb{T}) = \mathbb{T} : \mathbb{I} = T_{ii} = T_{11} + T_{22} + T_{33}. \tag{A.3}$$

---

Twice the symmetric part of a second rank tensor (twoSymm(T))

$$\mathrm{twoSymm}(\mathbb{T}) = \mathbb{T} + \mathbb{T}^{\top} = \begin{bmatrix} 2T_{11} & T_{12} + T_{21} & T_{13} + T_{31} \\ T_{21} + T_{12} & 2T_{22} & T_{23} + T_{32} \\ T_{31} + T_{13} & T_{32} + T_{23} & 2T_{33} \end{bmatrix}. \tag{A.4}$$

---

Gradient of a vector field (fvc::grad(u))

$$\boldsymbol{\nabla}\mathbf{u} = \frac{\partial u_i}{\partial x_j} = \begin{bmatrix} \partial u_1/\partial x_1 & \partial u_2/\partial x_1 & \partial u_3/\partial x_1 \\ \partial u_1/\partial x_2 & \partial u_2/\partial x_2 & \partial u_3/\partial x_2 \\ \partial u_1/\partial x_3 & \partial u_2/\partial x_3 & \partial u_3/\partial x_3 \end{bmatrix}. \tag{A.5}$$

---

Symmetric part of a second rank tensor

$$\mathrm{symm}(\mathbb{T}) = \frac{1}{2}(\mathbb{T} + \mathbb{T}^{\top}) = \frac{1}{2}\begin{bmatrix} 2T_{11} & T_{12} + T_{21} & T_{13} + T_{31} \\ T_{21} + T_{12} & 2T_{22} & T_{23} + T_{32} \\ T_{31} + T_{13} & T_{32} + T_{23} & 2T_{33} \end{bmatrix}. \tag{A.6}$$

Example: Calculation of the rate-of-strain tensor $S_{ij} = \frac{1}{2}\left(\frac{\partial U_i}{\partial x_j} + \frac{\partial U_j}{\partial x_i}\right)$.

```
1 tmp<volTensorField> tgradU(fvc::grad(U));
2 const volTensorField& gradU = tgradU();
3
4 volSymmTensorField S(symm(gradU));
```

Skew-symmetric part of a second rank tensor (skew(T))

$$\text{skew}(\mathbb{T}) = \frac{1}{2}(\mathbb{T} - \mathbb{T}^{\top}) = \frac{1}{2}\begin{bmatrix} 0 & T_{12} - T_{21} & T_{13} - T_{31} \\ T_{21} - T_{12} & 0 & T_{23} - T_{32} \\ T_{31} - T_{13} & T_{32} - T_{23} & 0 \end{bmatrix}. \tag{A.7}$$

Example: The rate-of-rotation (vorticity) tensor $\Omega_{ij} = \frac{1}{2}\left(\frac{\partial u_i}{\partial x_j} - \frac{\partial u_j}{\partial x_i}\right)$.

```
1 tmp<volTensorField> tgradU(fvc::grad(U));
2 const volTensorField& gradU = tgradU();
3
4 volTensorField Omega(skew(gradU));
```

Hodge dual (*T)

$$*\mathbb{T} = (T_{23}, -T_{13}, T_{12}). \tag{A.8}$$

Example: The vector of vorticity $\boldsymbol{\omega} = 2 \times (*\Omega_{ij}) = \left(\frac{\partial u_3}{\partial x_2} - \frac{\partial u_2}{\partial x_3}, \frac{\partial u_1}{\partial x_3} - \frac{\partial u_3}{\partial x_1}, \frac{\partial u_2}{\partial x_1} - \frac{\partial u_1}{\partial x_2}\right)$.

Deviatoric part of the tensor

$$\text{dev}(\mathbb{T}) = \mathbb{T} - \frac{1}{3}\text{tr}(\mathbb{T})\mathbb{I}. \tag{A.9}$$

Tensor (dyadic) product

$$\mathbb{A} \otimes \mathbb{B} = \mathbb{C}, \quad A_{ij}B_{kl} = C_{ijkl}. \tag{A.10}$$

mag - calculates the magnitude of a tensor

$$\text{mag}(\mathbb{D}) = |\mathbb{D}| = \sqrt{2\mathbb{D} : \mathbb{D}} = \sqrt{2D_{ij}D_{ij}}. \tag{A.11}$$

magSqr - calculates the magnitude-squared of a field

$$\text{magSqr}(\mathbb{D}) = |\mathbb{D}|^2 = 2D_{ij}D_{ij}. \tag{A.12}$$

## A.2 Time history of simulated sustained vowels

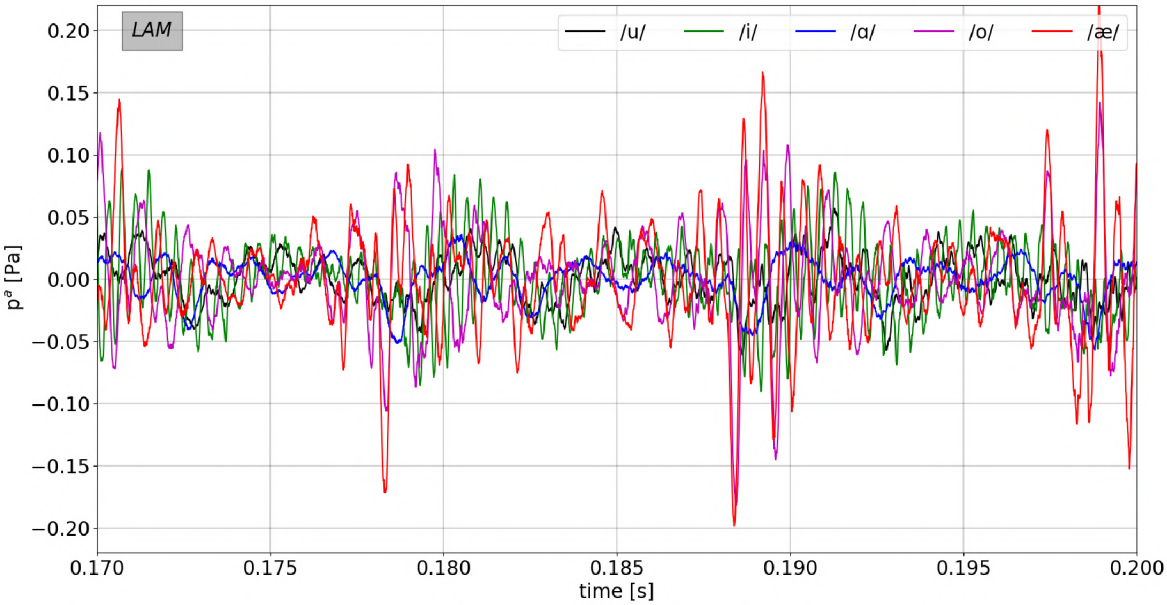


Fig. A.1: Time history of the acoustic pressure in MIC1 for five vowels. CAA simulation based on the CFD simulation with no SGS model.

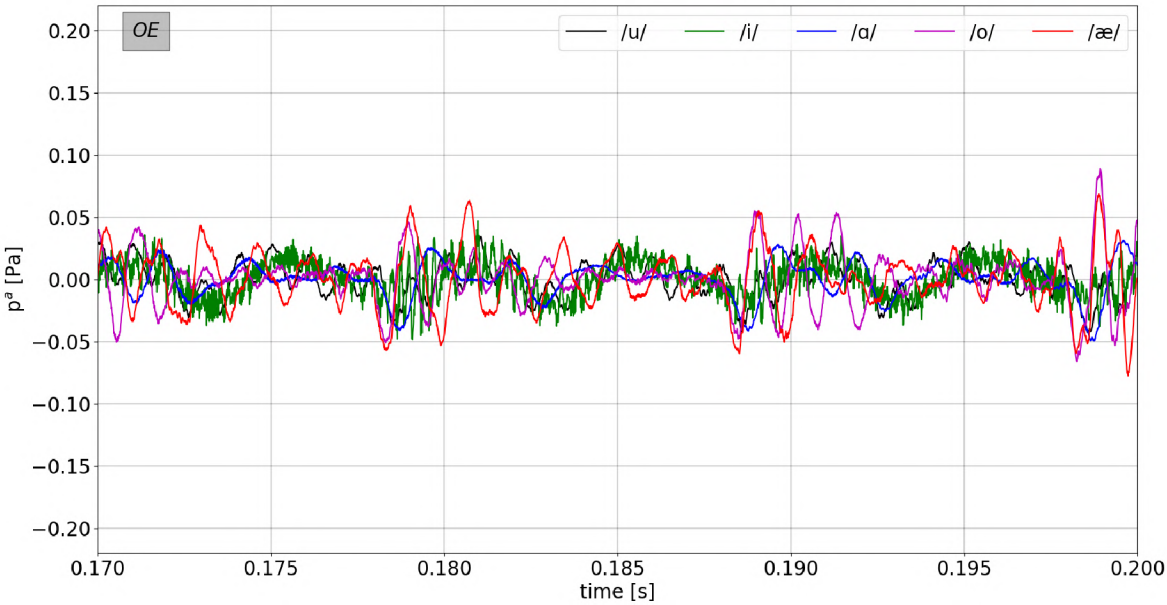


Fig. A.2: Time history of the acoustic pressure in MIC1 for five vowels. CAA simulation based on the CFD simulation with the OE SGS model.

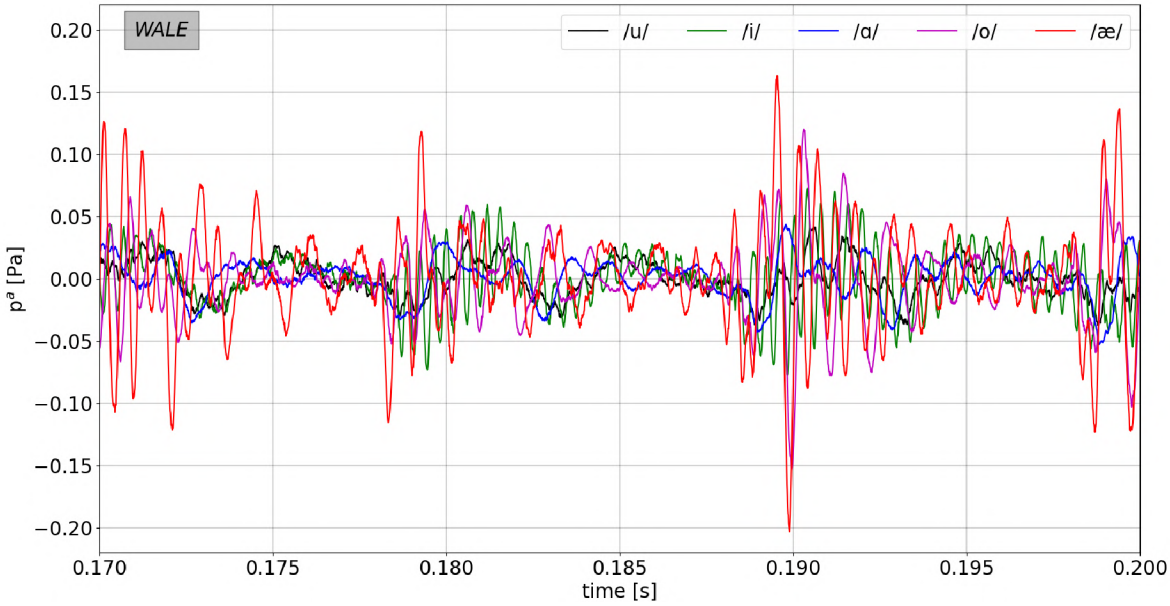


Fig. A.3: Time history of the acoustic pressure in MIC1 for five vowels. CAA simulation based on the CFD simulation with the WALE SGS model.

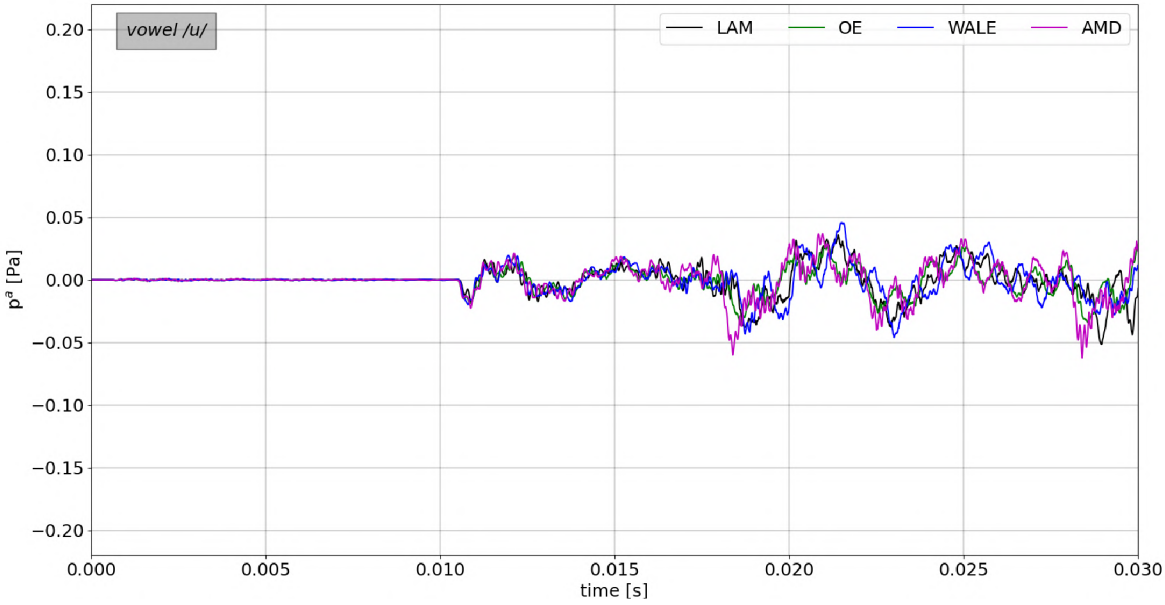


Fig. A.4: Acoustic time signals at monitoring point MIC1 for vowel /u/

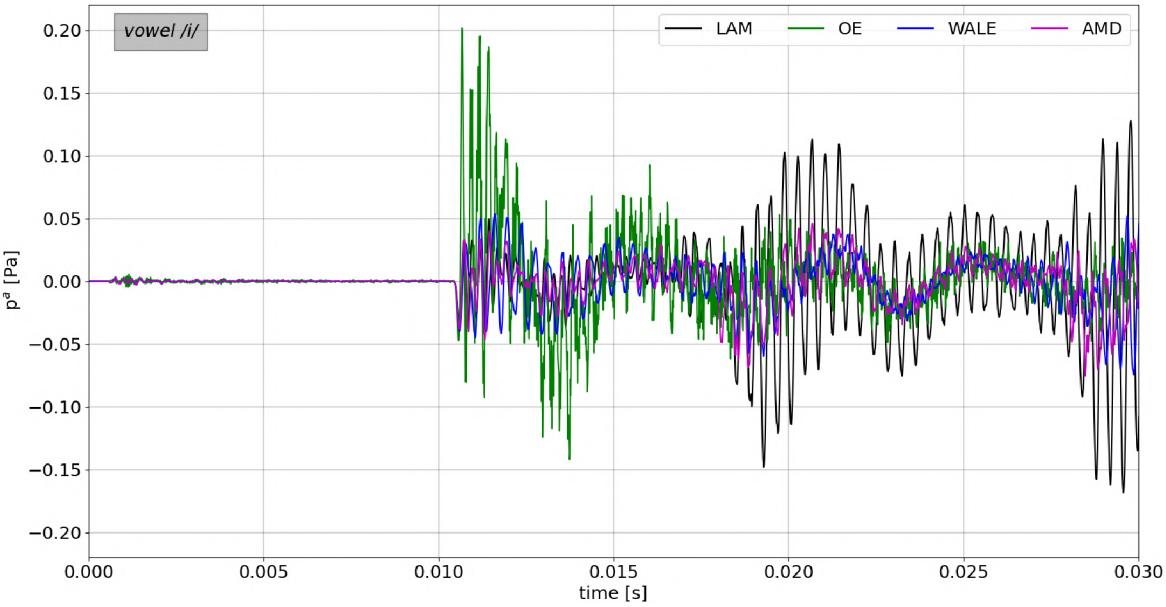


Fig. A.5: Acoustic time signals at monitoring point MIC1 for vowel /i/

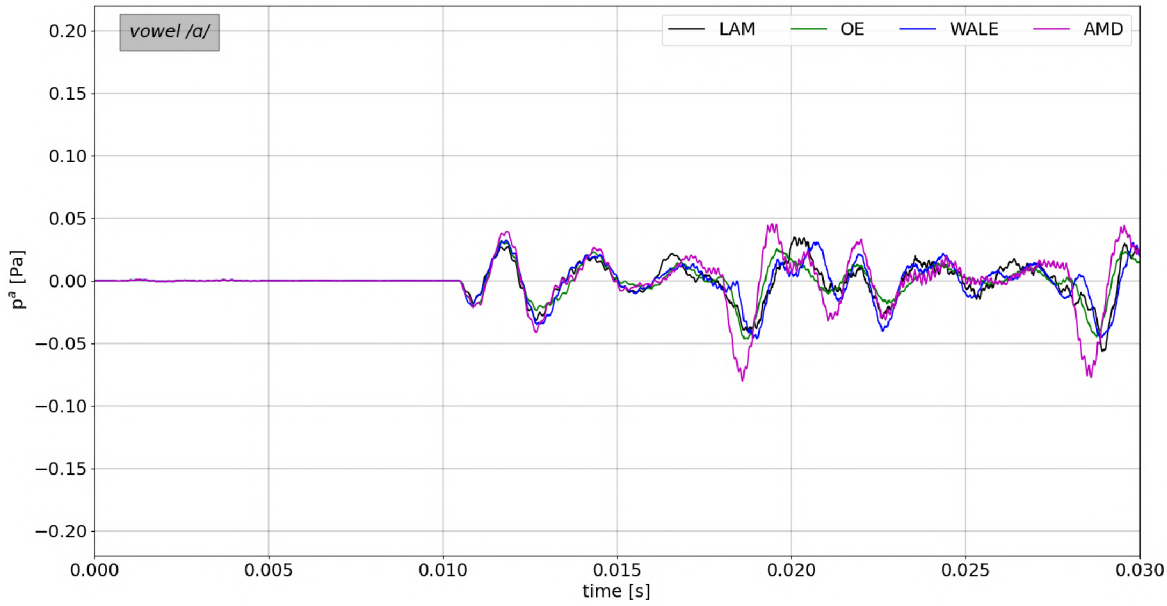


Fig. A.6: Acoustic time signals at monitoring point MIC1 for vowel /ɑ/

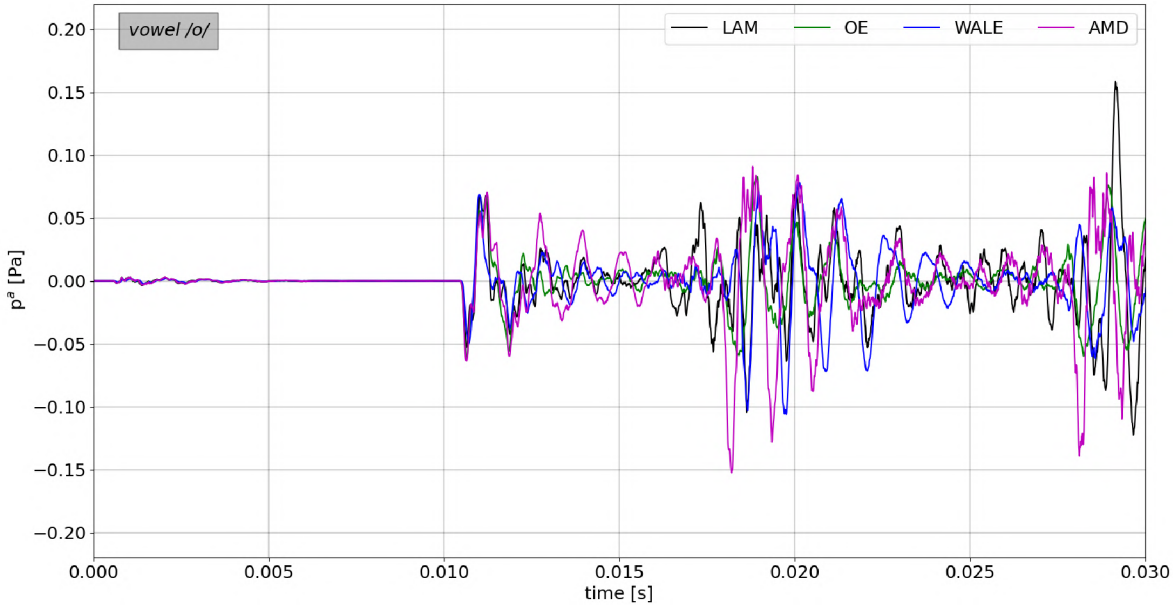


Fig. A.7: Acoustic time signals at monitoring point MIC1 for vowel /o/

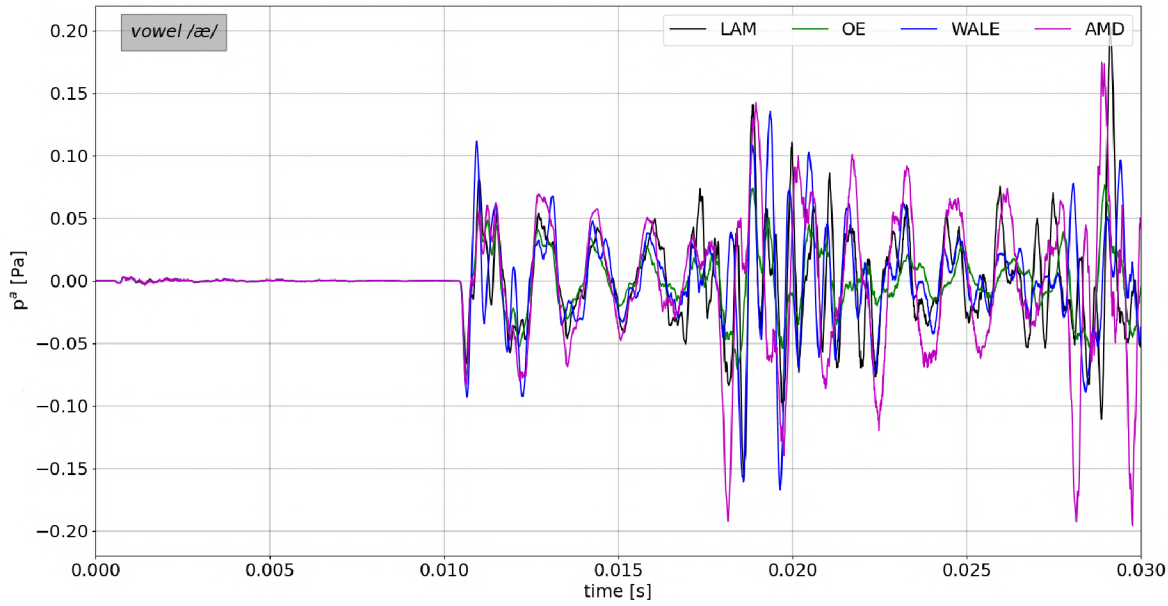


Fig. A.8: Acoustic time signals at monitoring point MIC1 for vowel /æ/

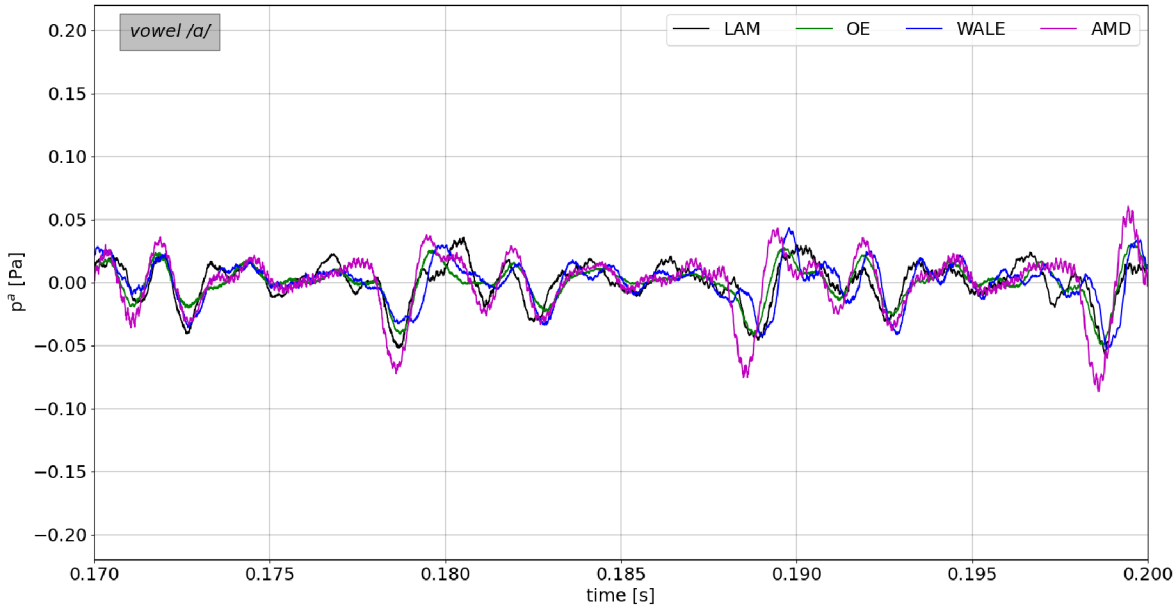


Fig. A.9: Acoustic time signals at the monitoring point MIC1 for vowel /ɑ/.

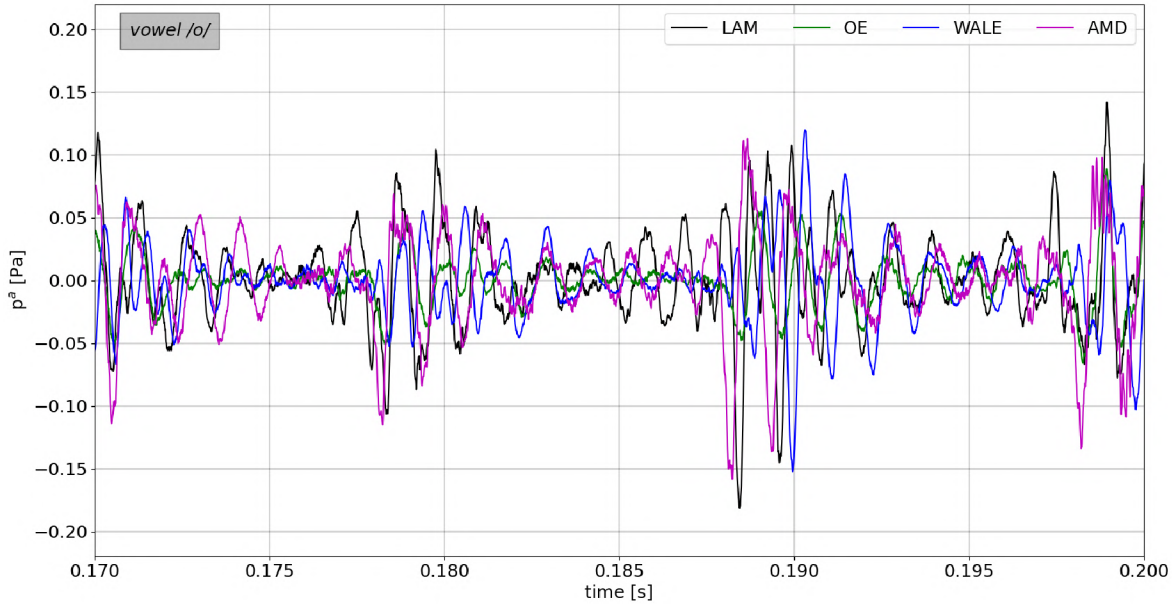


Fig. A.10: Acoustic time signals at the monitoring point MIC1 for vowel /o/.

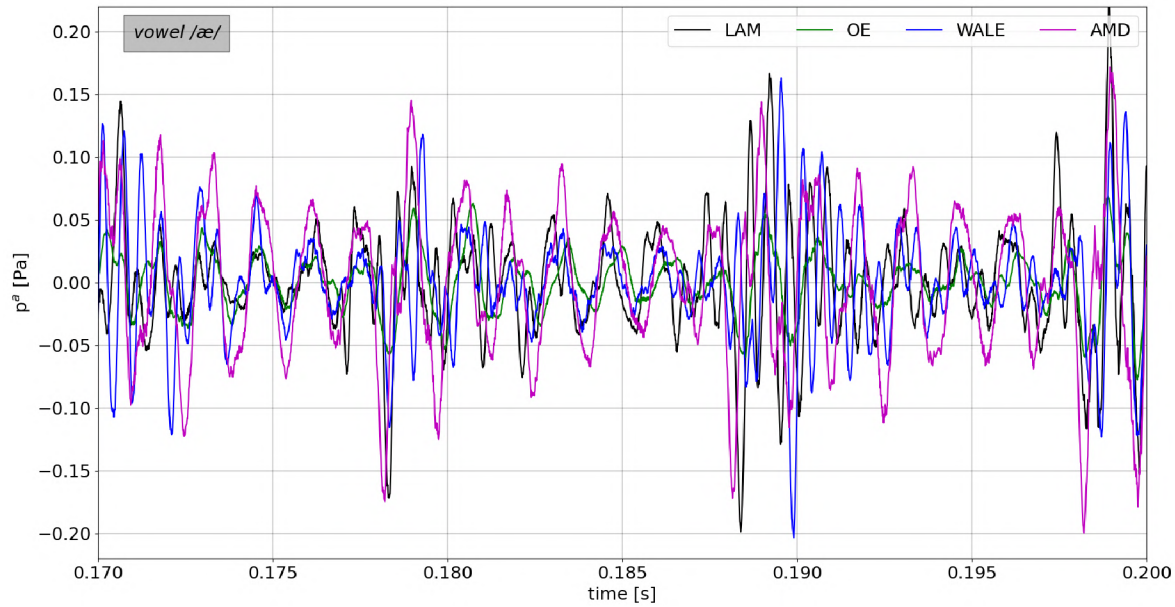


Fig. A.11: Acoustic time signals at the monitoring point MIC1 for vowel /æ/.

## A.3 Sound pressure levels

Tab. A.1: Sound pressure levels [dB] at the probe MIC1. 20 CAA simulations of five cardinal vowels /u, i, ɑ, o, æ/ based on four CFD simulations. The SPLs were evaluated for the fundamental frequency $f_o = 100$ Hz, higher harmonics $f_1 = 200$ Hz, $f_2 = 300$ Hz, non-harmonic frequency 1235 Hz and three formant frequencies $F_1 - F_3$.

| | $L_{f_o}^{/\mathrm{u}/}$ | $L_{f_1}^{/\mathrm{u}/}$ | $L_{f_2}^{/\mathrm{u}/}$ | $L_{1235}^{/\mathrm{u}/}$ | $L_{F1}^{/\mathrm{u}/}$ | $L_{F2}^{/\mathrm{u}/}$ | $L_{F3}^{/\mathrm{u}/}$ |
|---|---|---|---|---|---|---|---|
| LAM | 48.53 | 57.48 | 55.20 | 33.12 | 34.25 | 57.31 | 45.49 |
| OE | 38.34 | 55.13 | 47.79 | 15.33 | 28.94 | 40.88 | 35.76 |
| WALE | 44.06 | 56.86 | 53.52 | 20.03 | 33.42 | 48.29 | 42.15 |
| AMD | 44.20 | 56.46 | 53.75 | 27.80 | 32.71 | 62.02 | 30.52 |
| | $L_{f_o}^{/\mathrm{i}/}$ | $L_{f_1}^{/\mathrm{i}/}$ | $L_{f_2}^{/\mathrm{i}/}$ | $L_{1235}^{/\mathrm{i}/}$ | $L_{F1}^{/\mathrm{i}/}$ | $L_{F2}^{/\mathrm{i}/}$ | $L_{F3}^{/\mathrm{i}/}$ |
| LAM | 52.68 | 53.31 | 51.52 | 28.99 | 32.46 | 34.62 | 56.02 |
| OE | 42.07 | 57.76 | 46.08 | 15.24 | 28.49 | 29.70 | 43.95 |
| WALE | 47.69 | 59.45 | 51.88 | 19.86 | 34.13 | 35.96 | 58.77 |
| AMD | 46.80 | 58.35 | 51.15 | 26.20 | 58.50 | 41.25 | 52.30 |
| | $L_{f_o}^{/a/}$ | $L_{f_1}^{/a/}$ | $L_{f_2}^{/a/}$ | $L_{1235}^{/a/}$ | $L_{F1}^{/a/}$ | $L_{F2}^{/a/}$ | $L_{F3}^{/a/}$ |
| LAM | 42.98 | 52.75 | 55.86 | 25.44 | 51.19 | - | 39.62 |
| OE | 41.23 | 50.86 | 50.58 | 23.05 | 48.98 | - | 18.50 |
| WALE | 42.83 | 51.39 | 54.06 | 26.79 | 49.52 | - | 35.08 |
| AMD | 42.98 | 52.30 | 53.86 | 22.78 | 56.30 | - | 24.10 |
| | $L_{f_o}^{/\mathrm{o}/}$ | $L_{f_1}^{/\mathrm{o}/}$ | $L_{f_2}^{/\mathrm{o}/}$ | $L_{1235}^{/\mathrm{o}/}$ | $L_{F1}^{/\mathrm{o}/}$ | $L_{F2}^{/\mathrm{o}/}$ | $L_{F3}^{/\mathrm{o}/}$ |
| LAM | 38.63 | 46.76 | 45.79 | 41.86 | - | 56.17 | 43.59 |
| OE | 37.34 | 45.07 | 40.26 | 25.42 | - | 57.14 | 29.95 |
| WALE | 32.47 | 41.46 | 39.93 | 26.12 | - | 51.62 | 41.10 |
| AMD | 38.96 | 46.76 | 43.18 | 37.47 | - | 63.31 | 34.70 |
| | $L_{f_o}^{/\mathrm{æ}/}$ | $L_{f_1}^{/\mathrm{æ}/}$ | $L_{f_2}^{/\mathrm{æ}/}$ | $L_{1235}^{/\mathrm{æ}/}$ | $L_{F1}^{/\mathrm{æ}/}$ | $L_{F2}^{/\mathrm{æ}/}$ | $L_{F3}^{/\mathrm{æ}/}$ |
| LAM | 39.70 | 48.63 | 48.32 | 43.59 | 62.34 | 58.15 | 51.20 |
| OE | 38.23 | 46.44 | 42.65 | 26.63 | 60.71 | 52.74 | 35.79 |
| WALE | 39.24 | 47.73 | 46.43 | 30.15 | 57.47 | 55.26 | 50.25 |
| AMD | 40.22 | 48.54 | 45.79 | 22.37 | 71.42 | 49.46 | 49.46 |

# References

M. Abkar and P. Moin. Large-eddy simulation of thermally stratified atmospheric boundary-layer flow using a minimum dissipation model. *Boundary-layer meteorology*, 165(3):405–419, 2017. DOI 10.1007/s10546-017-0288-4.

M. Agarwal, R. Scherer, and H. Hollien. The false vocal folds: shape and size in frontal view during phonation based on laminagraphic tracings. *Journal of Voice*, 17(2):97–113, June 2003. DOI 10.1016/S0892-1997(03)00012-2.

F. Alipour and R. C. Scherer. Pulsatile airflow during phonation: An excised larynx model. *The Journal of the Acoustical Society of America*, 97(2):1241–1248, feb 1995. DOI 10.1121/1.412233.

F. Alipour and R. C. Scherer. Flow separation in a computational oscillating vocal fold model. *Journal of the Acoustical Society of America*, 116(3):1710–1719, Sept. 2004. DOI 10.1121/1.1779274.

F. Alipour and R. C. Scherer. Characterizing glottal jet turbulence. *Journal of the Acoustical Society of America*, 119(2):1063–1073, Feb. 2006. DOI 10.1121/1.2151809.

M. Arnela, O. Guasch, and F. Alías. Effects of head geometry simplifications on acoustic radiation of vowel sounds based on time-domain finite-element simulations. *The Journal of the Acoustical Society of America*, 134(4):2946–2954, 2013. DOI 10.1121/1.4818756.

M. Arnela, R. Blandin, S. Dabbaghchian, O. Guasch, F. Alías, X. Pelorson, A. Van Hirtum, and O. Engwall. Influence of lips on the production of vowels based on finite element simulations and experiments. *The Journal of the Acoustical Society of America*, 139(5):2852–2859, 2016a. DOI 10.1121/1.4950698.

M. Arnela, S. Dabbaghchian, R. Blandin, O. Guasch, O. Engwall, A. Van Hirtum, and X. Pelorson. Influence of vocal tract geometry simplifications on the numerical simulation of vowel sounds. *The Journal of the Acoustical Society of America*, 140(3): 1707–1718, 2016b. DOI 10.1121/1.4962488.

B. S. Atal and S. L. Hanauer. Speech analysis and synthesis by linear prediction of the speech wave. *The journal of the acoustical society of America*, 50(2B):637–655, 1971. DOI 10.1121/1.1912679.

Y. Bae and Y. J. Moon. Computation of phonation aeroacoustics by an ins/pce splitting method. *Computers & fluids*, 37(10):1332–1343, 2008. DOI 10.1016/j.compfluid.2007.12.002.

R. J. Baken and R. F. Orlikoff. *Clinical measurement of speech and voice*. Cengage Learning, 2000. ISBN 1565938690.

L. Barona-Lleo and S. Fernandez. Hyperfunctional voice disorder in children with attention deficit hyperactivity disorder (ADHD). A phenotypic characteristic? *Journal of Voice*, 30(1):114–119, 2016. DOI 10.1016/j.jvoice.2015.03.002.

A. H. Benade. *Fundamentals of musical acoustics*. Courier Corporation, 1990.

J.-P. Berenger. A perfectly matched layer for the absorption of electromagnetic waves. *Journal of computational physics*, 114(2):185–200, 1994. DOI 10.1006/jcph.1994.1159.

V. Birk, S. Kniesburges, M. Semmler, D. A. Berry, C. Bohr, M. Döllinger, and A. Schützenberger. Influence of glottal closure on the phonatory process in ex vivo porcine larynges. *The Journal of the Acoustical Society of America*, 142(4):2197–2207, 2017. DOI 10.1121/1.5007952.

D. Blokhintsev. Acoustics of a nonhomogeneous moving medium. 1956.

B.-T. Chu and L. S. Kovásznay. Non-linear interactions in a viscous heat-conducting compressible gas. *Journal of Fluid Mechanics*, 3(5):494–514, 1958. DOI 10.1017/s0022112058000148.

A. Clark, H. Ferziger, and C. Reynolds. Evaluation of subgrid-scale models using an accurately simulated turbulent flow. *Journal of fluid mechanics*, 91(1):1–16, 1979. DOI 10.1017/s002211207900001x.

N. Curle. The influence of solid boundaries upon aerodynamic sound. *Proceedings of the Royal Society of London. Series A. Mathematical and Physical Sciences*, 231(1187): 505–514, 1955.

C. F. de Luzan, J. Chen, M. Mihaescu, S. M. Khosla, and E. Gutmark. Computational study of false vocal folds effects on unsteady airflows through static models of the human larynx. *Journal of Biomechanics*, 48(7):1248–1257, 2015. DOI 10.1016/j.jbiomech.2015.03.010.

M. de Oliviera Rosa, J. Pereira, M. Grellet, and A. Alwan. A contribution to simulating a three-dimensional larynx model using the finite element method. *Journal of the Acoustical Society of America*, 114(5):2893–2905, Nov. 2003. DOI 10.1121/1.1619981.

T. Dodderi, M. Narra, S. M. Varghese, and D. T. Deepak. Spectral analysis of hypernasality in cleft palate children: a pre-post surgery comparison. *Journal of clinical and diagnostic research: JCDR*, 10(1):MC01, 2016. DOI 10.7860/jcdr/2016/15389.7055.

C. Drioli and P. Aichinger. Modelling sagittal and vertical phase differences in a lumped and distributed elements vocal fold model. *Biomedical Signal Processing and Control*, 64:102309, 2021. DOI 10.1016/j.bspc.2020.102309.

J. P. Dworkin. Laryngitis: types, causes, and treatments. *Otolaryngologic clinics of North America*, 41(2):419–436, 2008. DOI 10.1016/j.otc.2007.11.011.

M. Döllinger, J. Kobler, D. A Berry, D. D Mehta, G. Luegmair, and C. Bohr. Experiments on analysing voice production: Excised (human, animal) and in vivo (animal) approaches. *Current bioinformatics*, 6(3):286–304, 2011. DOI 10.2174/157489311796904673.

B. Erath and M. Plesniak. An investigation of asymmetric flow features in a scaled-up driven model of the human vocal folds. *Experiments in Fluids*, 49(1):131–146, 2010. DOI 10.1007/s00348-009-0809-0.

R. Ewert and W. Schröder. Acoustic perturbation equations based on flow decomposition via source filtering. *Journal of Computational Physics*, 188(2):365–398, 2003. DOI 10.1016/s0021-9991(03)00168-2.

S. Falk, S. Kniesburges, S. Schoder, B. Jakubaß, P. Maurerlehner, M. Echternach, M. Kaltenbacher, and M. Döllinger. 3d-fv-fe aeroacoustic larynx model for investigation of functional based voice disorders. *Frontiers in Physiology*, 12:226, 2021. ISSN 1664-042X. DOI 10.3389/fphys.2021.616985.

G. Fant. *Acoustic theory of speech production*. Number 2. Walter de Gruyter, 1970.

E. Fares, B. Duda, and M. R. Khorrami. Airframe noise prediction of a full aircraft in model and full scale using a lattice boltzmann approach. In *22nd AIAA/CEAS Aeroacoustics Conference*, page 2707, 2016. DOI 10.2514/6.2016-2707.

H. Ferziger. Direct and large eddy simulation of turbulence. *Numerical methods in fluid mechanics*, 16:53–73, 1998. DOI 10.1299/kikaib.66.651$_2$754.

J. E. Ffowcs Williams and D. L. Hawkings. Sound generation by turbulence and surfaces in arbitrary motion. *Philosophical Transactions of the Royal Society of London. Series A, Mathematical and Physical Sciences*, 264(1151):321–342, 1969. DOI 10.1098/rsta.1969.0031.

W. T. S. Fitch. *Vocal tract length perception and the evolution of language*. PhD thesis, Brown University Providence, RI, 1994.

C. A. Fletcher. Fluid dynamics: The governing equations. In *Computational Techniques for Fluid Dynamics 2*, pages 1–46. Springer: Berlin/Heidelberg, 1991. DOI 10.1007/978-3-642-58239-4$_1$.

J. Freund, S. Lele, and P. Moin. Numerical simulation of a mach 1.92 turbulent jet and its sound field. *AIAA journal*, 38(11):2023–2031, 2000. DOI 10.2514/3.14646.

J. Fröhlich, C. P. Mellen, W. Rodi, L. Temmerman, and M. A. Leschziner. Highly resolved large-eddy simulation of separated flow in a channel with streamwise periodic constrictions. *Journal of Fluid Mechanics*, 526:19–66, 2005. DOI 10.1017/s0022112004002812.

N. J. Georgiadis, D. P. Rizzetta, and C. Fureby. Large-eddy simulation: current capabilities, recommended practices, and future research. *AIAA journal*, 48(8):1772–1784, 2010. DOI 10.2514/1.j050232.

M. Germano, U. Piomelli, P. Moin, and W. H. Cabot. A dynamic subgrid-scale eddy viscosity model. *Physics of Fluids A: Fluid Dynamics*, 3(7):1760–1765, 1991. DOI 10.1063/1.857955.

J. Grisel, S. Khosla, S. Murugappan, R. Lakhamraju, J. Aubry, E. Gutmark, and G. Huntress. How does the absence or presence of subglottal medialization affect glottal airflow? *Annals of Otology, Rhinology & Laryngology*, 119(8):559–566, 2010. DOI 10.1177/000348941011900809.

P. Hájek, P. Švancara, J. Horáček, and J. G. Švec. Finite element modelling of the effect of stiffness and damping of vocal fold layers on their vibrations and produced sound. In *Applied Mechanics and Materials*, volume 821, pages 657–664. Trans Tech Publ, 2016. DOI 10.4028/www.scientific.net/amm.821.657.

J. Hardin and D. Pope. An acoustic/viscous splitting technique for computational aeroacoustics. *Theoretical and computational fluid dynamics*, 6(5):323–340, 1993. DOI 10.1007/bf00311844.

A. L. Hemmerich, E. M. Finnegan, and H. T. Hoffman. The distribution and severity of tremor in speech structures of persons with vocal tremor. *Journal of Voice*, 31(3): 366–377, 2017. DOI 10.1016/j.jvoice.2016.05.004.

S. Hertegård, S. Granqvist, and P.-Å. Lindestad. Botulinum toxin injections for essential voice tremor. *Annals of Otology, Rhinology & Laryngology*, 109(2):204–209, 2000. DOI 10.1177/000348940010900216.

J. Horáček, A.-M. Laukkanen, and P. Šidlof. Estimation of impact stress using an aeroelastic model of voice production. *Logopedics Phoniatrics Vocology*, 32(4):185–192, 2007. DOI 10.1080/14015430600628039.

M. Howe. *Acoustics and Aerodynamic Sound*. Cambridge University Press, 2014. DOI 10.1017/CBO9781107360273.

A. Hüppe and M. Kaltenbacher. Investigation of interpolation strategies for hybrid schemes in computational aeroacoustics. In *Proc DAGA*, pages 16–19, 2015.

A. Hüppe, J. Grabinger, M. Kaltenbacher, A. Reppenhagen, G. Dutzler, and W. Kühnel. A non-conforming finite element method for computational aeroacoustics in rotating systems. In *20th AIAA/CEAS Aeroacoustics Conference*, page 2739, 2014. DOI 10.2514/6.2014-2739.

A. Hüppe. *Spectral Finite Elements for Acoustic Field Computation*. PhD thesis, Alps-Adriatic University of Klagenfurt, 2012.

D. Ireland, C. Knuepffer, and S. J. McBride. Adaptive multi-rate compression effects on vowel analysis. *Frontiers in bioengineering and biotechnology*, 3:118, 2015. DOI 10.3389/fbioe.2015.00118.

H. Jasak. *Error analysis and estimation for the finite volume method with applications to fluid flows*. PhD thesis, 1996.

T. Jeffery, S. Cunningham, and S. P. Whiteside. Analyses of sustained vowels in down syndrome (ds): A case study using spectrograms and perturbation data to investigate voice quality in four adults with ds. *Journal of Voice*, 32(5):644–e11, 2018. DOI 10.1016/j.jvoice.2017.08.004.

W. Jiang, X. Zheng, and Q. Xue. Computational modeling of fluid–structure–acoustics interaction during voice production. *Frontiers in bioengineering and biotechnology*, 5: 7, 2017. DOI 10.3389/fbioe.2017.00007.

X. Jiang and C.-H. Lai. *Numerical techniques for direct and large-eddy simulations*. CRC press, 2016. DOI 10.1201/9781420075793.

Y. Jo, H. Ra, Y. J. Moon, and M. Döllinger. Three-dimensional computation of flow and sound for human hemilarynx. *Computers & Fluids*, 134:41–50, 2016. DOI 10.1016/j.compfluid.2016.04.029.

B. Kaltenbacher, M. Kaltenbacher, and I. Sim. A modified and stable version of a perfectly matched layer technique for the 3-d second order wave equation in time domain with an application to aeroacoustics. *Journal of computational physics*, 235:407–422, 2013. DOI 10.1016/j.jcp.2012.10.016.

M. Kaltenbacher. *Computational Acoustics*. Springer, 2018. ISBN 978-3-319-59038-7. DOI 10.1007/978-3-319-59038-7.

R. G. Kamiloğlu, A. H. Fischer, and D. A. Sauter. Good vibrations: A review of vocal expressions of positive emotions. *Psychonomic bulletin & review*, 27(2):237–265, 2020. DOI 10.3758/s13423-019-01701-x.

R. D. Kent, G. Weismer, J. F. Kent, H. K. Vorperian, and J. R. Duffy. Acoustic studies of dysarthric speech: Methods, progress, and potential. *Journal of communication disorders*, 32(3):141–186, 1999. DOI 10.1016/S0021-9924(99)00004-0.

S. Kniesburges, S. L Thomson, A. Barney, M. Triep, P. Sidlof, J. Horacek, C. Brucker, and S. Becker. In vitro experimental investigation of voice production. *Current bioinformatics*, 6(3):305–322, 2011. DOI 10.2174/157489311796904637.

S. Kniesburges, C. Hesselmann, S. Becker, E. Schlücker, and M. Döllinger. Influence of vortical flow structures on the glottal jet location in the supraglottal region. *Journal of Voice*, 27(5):531–544, 2013. DOI 10.1016/j.jvoice.2013.04.005.

K. Konstantopoulos, Y.-P. Christou, P. Vogazianos, E. Zamba-Papanicolaou, and K. A. Kleopa. A quantitative method for the assessment of dysarthrophonia in myasthenia gravis. *Journal of the neurological sciences*, 377:42–46, 2017. DOI 10.1016/j.jns.2017.03.045.

P. K. Kuhl, J. E. Andruski, I. A. Chistovich, L. A. Chistovich, E. V. Kozhevnikova, V. L. Ryskina, E. I. Stolyarova, U. Sundberg, and F. Lacerda. Cross-language analysis of phonetic units in language addressed to infants. *Science*, 277(5326):684–686, 1997. DOI 10.1126/science.277.5326.684.

M. Larsson and B. Müller. Numerical simulation of confined pulsating jets in human phonation. *Computers & Fluids*, 38:1375–1383, 2009. DOI 10.1016/j.compfluid.2008.01.033.

M. Lasota, P. Šidlof, M. Kaltenbacher, and S. Schoder. Impact of the sub-grid scale turbulence model in aeroacoustic simulation of human voice. *Applied Sciences*, 11(4): 1970, Feb. 2021. DOI 10.3390/app11041970.

D. R. Launchbury. *Unsteady turbulent flow modelling and applications*. Springer: Berlin/Heidelberg, 2016.

G.-S. Lee, C.-P. Wang, and S. Fu. Evaluation of hypernasality in vowels using voice low tone to high tone ratio. *The Cleft Palate-Craniofacial Journal*, 46(1):47–52, 2009. DOI 10.1597/07-184.1.

A. Leonard. Energy cascade in large-eddy simulations of turbulent fluid flows. In *Advances in geophysics*, volume 18, pages 237–248. Elsevier: Amsterdam, The Netherlands, 1975. DOI 10.1016/S0065-2687(08)60464-1.

M. Lesieur, O. Métais, and P. Comte. *Large-eddy simulations of turbulence*. Cambridge University Press: Cambridge, UK, 2005.

M. J. Lighthill. On sound generated aerodynamically. I. General theory. In *Proceedings of the Royal Society of London A: Mathematical, Physical and Engineering Sciences*, volume 211, pages 564–587. The Royal Society, 1952. DOI 10.1098/rspa.1952.0060.

M. J. Lighthill. On sound generated aerodynamically II. Turbulence as a source of sound. *Proceedings of the Royal Society of London. Series A. Mathematical and Physical Sciences*, 222(1148):1–32, 1954. DOI 10.1098/rspa.1954.0049.

G. Link, M. Kaltenbacher, M. Breuer, and M. Döllinger. A 2D finite-element scheme for fluid–solid–acoustic interactions and its application to human phonation. *Computer Methods in Applied Mechanics and Engineering*, 198(41-44):3321–3334, 2009. DOI doi:10.1016/j.cma.2009.06.009.

A. Lodermeyer, S. Becker, M. Döllinger, and S. Kniesburges. Phase-locked flow field analysis in a synthetic human larynx model. *Experiments in Fluids*, 56(4):1–13, 2015. DOI 10.1007/s00348-015-1942-6.

H. Luo, R. Mittal, X. Zheng, S. A. Bielamowicz, R. J. Walsh, and J. K. Hahn. An immersed-boundary method for flow–structure interaction in biological systems with application to phonation. *Journal of computational physics*, 227(22):9303–9332, 2008. DOI 10.1016/j.jcp.2008.05.001.

S. Marié, D. Ricot, and P. Sagaut. Comparison between lattice boltzmann method and navier–stokes high order schemes for computational aeroacoustics. *Journal of Computational Physics*, 228(4):1056–1070, 2009. DOI 10.1016/j.jcp.2008.10.021.

P. Mason and N. Callen. On the magnitude of the subgrid-scale eddy coefficient in large-eddy simulations of turbulent channel flow. *Journal of Fluid Mechanics*, 162:439–462, 1986. DOI 10.1017/s0022112086002112.

W. Mattheus and C. Brücker. Asymmetric glottal jet deflection: differences of two-and three-dimensional models. *The Journal of the Acoustical Society of America*, 130(6): EL373–EL379, 2011. DOI 10.1121/1.3655893.

P. Maurerlehner, S. Schoder, C. Freidhager, A. Wurzinger, A. Hauser, F. Kraxberger, S. Falk, S. Kniesburges, M. Echternach, M. Döllinger, et al. Efficient numerical simulation of the human voice. *Elektrotechnik und Informationstechnik*, 138(3):219–228, 2021. DOI 10.1007/s00502-021-00886-1.

O. Mcmillan, J. Ferziger, and R. Rogallo. Tests of subgrid-scale models in strained turbulence. In *13th Fluid and PlasmaDynamics Conference*, page 1339, 1980. DOI 10.2514/6.1980-1339.

W. C. Meecham and G. Ford. Acoustic radiation from isotropic turbulence. *The Journal of the Acoustical Society of America*, 30(4):318–322, 1958. DOI 10.1121/1.1909583.

C. Meneveau and J. Katz. Scale-invariance and turbulence models for large-eddy simulation. *Annual Review of Fluid Mechanics*, 32(1):1–32, 2000. DOI 10.1146/annurev.fluid.32.1.1.

M. Mihaescu, S. M. Khosla, S. Murugappan, and E. J. Gutmark. Unsteady laryngeal airflow simulations of the intra-glottal vortical structures. *Journal of the Acoustical Society of America*, 127(1):435–444, 2010. ISSN 00014966. DOI DOI:10.1121/1.3271276.

M. Mihaescu, G. Mylavarapu, E. J. Gutmark, and N. B. Powell. Large eddy simulation of the pharyngeal airflow associated with obstructive sleep apnea syndrome at pre and post-surgical treatment. *Journal of Biomechanics*, 44(12):2221–2228, Aug. 2011. ISSN 0021-9290. DOI 10.1016/j.jbiomech.2011.06.006.

R. Mittal, B. D. Erath, and M. W. Plesniak. Fluid dynamics of human phonation and speech. *Annual Review of Fluid Mechanics*, 45:437–467, 2013. DOI 10.1146/annurev-fluid-011212-140636.

L. Mongeau, N. Franchek, C. H. Coker, and R. A. Kubli. Characteristics of a pulsating jet through a small modulated orifice, with application to voice production. *The Journal of the Acoustical Society of America*, 102(2):1121–1133, 1997. DOI 10.1121/1.419864.

D. Moser, J. Kim, and N. Mansour. Direct numerical simulation of turbulent channel flow up to Re $\tau$= 590. *Physics of fluids*, 11(4):943–945, 1999. DOI 10.1063/1.869966.

C. P. Moura, L. M. Cunha, H. Vilarinho, M. J. Cunha, D. Freitas, M. Palha, S. M. Pueschel, and M. Pais-Clemente. Voice parameters in children with down syndrome. *Journal of Voice*, 22(1):34–42, 2008. ISSN 0892-1997. DOI 10.1016/j.jvoice.2006.08.011.

F. Nicoud and F. Ducros. Subgrid-scale stress modelling based on the square of the velocity gradient tensor. *Flow, turbulence and Combustion*, 62(3):183–200, 1999. DOI 10.1023/A:1009995426001.

L. Oren, S. Khosla, S. Murugappan, R. King, and E. Gutmark. Role of subglottal shape in turbulence reduction. *Annals of Otology, Rhinology and Laryngology*, 118(3):232–240, 2009. DOI 10.1177/000348940911800312.

J. R. Orozco-Arroyave, F. Hönig, J. D. Arias-Londoño, J. F. Vargas-Bonilla, S. Skodda, J. Rusz, and E. Nöth. Voiced/unvoiced transitions in speech as a potential bio-marker to detect parkinson's disease. *In Sixteenth Annual Conference of the International Speech Communication Association*, 2015. DOI 10.21437/interspeech.2015-34.

G. Peters, O. Wendler, D. Böhringer, A.-O. Gostian, S. K. Müller, H. Canziani, N. Hesse, M. Semmler, D. A. Berry, S. Kniesburges, et al. Human laryngeal mucus from the vocal folds: Rheological characterization by particle tracking microrheology and oscillatory shear rheology. *Applied Sciences*, 11(7):3011, 2021. DOI 10.3390/app11073011.

G. E. Peterson and H. L. Barney. Control methods used in a study of the vowels. *The Journal of the acoustical society of America*, 24(2):175–184, 1952. DOI 10.1121/1.1906875.

B. A. Pickup and S. L. Thomson. Identification of geometric parameters influencing the flow-induced vibration of a two-layer self-oscillating computational vocal fold model. *The Journal of the Acoustical Society of America*, 129(4):2121–2132, 2011. DOI 10.1121/1.3557046.

U. Piomelli, P. Moin, and J. H. Ferziger. Model consistency in large eddy simulation of turbulent channel flows. *The Physics of fluids*, 31(7):1884–1891, 1988. DOI 10.1063/1.866635.

S. B. Pope. *Turbulent Flows*. Cambridge University Press, Aug. 2000. DOI 10.1017/cbo9780511840531.

J. Probst, A. Lodermeyer, S. Fattoum, S. Becker, M. Echternach, B. Richter, M. Döllinger, and S. Kniesburges. Acoustic and aerodynamic coupling during phonation in mri-based vocal tract replicas. *Applied Sciences*, 9(17):3562, 2019. DOI 10.3390/app9173562.

L. Rammage. *Disorders of voice*. Cambridge Handbooks in Language and Linguistics. Cambridge University Press, 2013. DOI 10.1017/CBO9781139108683.030.

H. Ribner. Aerodynamic sound from fluid dilatations. A theory of the sound from jets and other flows. university of toronto. *Institute for Aerospace Studies, UTIA Rep*, 86, 1962.

W. Rozema, H. J. Bae, P. Moin, and R. Verstappen. Minimum-dissipation models for large-eddy simulation. *Physics of Fluids*, 27(8):085107, 2015. DOI 10.1063/1.4928700.

J. Rusz, R. Cmejla, T. Tykalova, H. Ruzickova, J. Klempir, V. Majerova, J. Picmausova, J. Roth, and E. Ruzicka. Imprecise vowel articulation as a potential early marker of parkinson's disease: effect of speaking task. *Journal of the Acoustical Society of America*, 134(3):2171–2181, 2013. DOI 10.1121/1.4816541.

H. Sadeghi, M. Döllinger, M. Kaltenbacher, and S. Kniesburges. Aerodynamic impact of the ventricular folds in computational larynx models. *The Journal of the Acoustical Society of America*, 145(4):2376–2387, 2019a. DOI 10.1121/1.5098775.

H. Sadeghi, S. Kniesburges, S. Falk, M. Kaltenbacher, A. Schützenberger, and M. Döllinger. Towards a clinically applicable computational larynx model. *Applied Sciences*, 9(11):2288, 2019b. DOI 10.3390/app9112288.

H. Sadeghi, S. Kniesburges, M. Kaltenbacher, A. Schützenberger, and M. Döllinger. Computational models of laryngeal aerodynamics: Potentials and numerical costs. *Journal of Voice*, 33(4):385–400, 2019c. DOI 10.1016/j.jvoice.2018.01.001.

L. Sanders, E. Manoha, M. Murayama, Y. Yokokawa, K. Yamamoto, and T. Hirai. Lattice-boltzmann flow simulation of a two-wheel landing gear. In *22nd AIAA/CEAS Aeroacoustics Conference*, page 2767, 2016. DOI 10.2514/6.2016-2767.

R. Scherer, D. Shinwari, J. De Witt, C. Zhang, R. Kucinschi, and A. Afjeh. Intraglottal pressure profiles for a symmetric and oblique glottis with a divergence angle of 10 degrees. *The Journal of the Acoustical Society of America*, 109(4):1616–1630, 2001. DOI 10.1121/1.1333420.

L. Schickhofer, J. Malinen, and M. Mihaescu. Compressible flow simulations of voiced speech using rigid vocal tract geometries acquired by mri. *The Journal of the Acoustical Society of America*, 145(4):2049–2061, 2019. DOI 10.1121/1.5095250.

H. Schlichting and K. Gersten. *Boundary-layer theory*. Springer, 2016.

S. Schoder, M. Kaltenbacher, and K. Roppert. Helmholtz's decomposition applied to aeroacoustics. In *25th AIAA/CEAS Aeroacoustics Conference*, page 2561, 2019. DOI 10.2514/6.2019-2561.

S. Schoder, M. Weitz, P. Maurerlehner, A. Hauser, S. Falk, S. Kniesburges, M. Döllinger, and M. Kaltenbacher. Hybrid aeroacoustic approach for the efficient numerical simulation of human phonation. *The Journal of the Acoustical Society of America*, 147(2):1179–1194, 2020. DOI 10.1121/10.0000785.

R. Schwarze, W. Mattheus, J. Klostermann, and C. Brücker. Starting jet flows in a three-dimensional channel with larynx-shaped constriction. *Computers & Fluids*, 48 (1):68–83, 2011. DOI 10.1016/j.compfluid.2011.03.016.

S. Seifpanahi, M. Bakhtiar, and T. Salmalian. Objective vocal parameters in farsi-speaking adults with down syndrome. *Folia Phoniatrica et Logopaedica*, 63(2):72–76, 2011. DOI 10.1159/000316326.

J.-H. Seo and Y. J. Moon. Perturbed compressible equations for aeroacoustic noise prediction at low mach numbers. *AIAA journal*, 43(8):1716–1724, 2005. DOI 10.2514/1.3001.

J. H. Seo and Y. J. Moon. Linearized perturbed compressible equations for low mach number aeroacoustics. *Journal of Computational Physics*, 218(2):702–719, 2006. DOI 10.1016/j.jcp.2006.03.003.

L. D. Shriberg, R. D. Kent, and B. Munson. *Clinical phonetics*. Allyn and Bacon Boston, MA, 2003.

P. Šidlof, S. Zörner, and A. Hüppe. A hybrid approach to the computational aeroacoustics of human voice production. *Biomechanics and modeling in mechanobiology*, 14(3):473–488, 2015. DOI 10.1007/s10237-014-0617-1.

S. Skodda, W. Grönheit, and U. Schlegel. Impairment of vowel articulation as a possible marker of disease progression in parkinson's disease. *PloS one*, 7(2):e32132, 2012. DOI 10.1371/journal.pone.0032132.

J. Smagorinsky. General circulation experiments with the primitive equations: I. the basic experiment. *Monthly weather review*, 91(3):99–164, 1963. DOI 10.1175/1520-0493(1963)091¡0099:gcewtp¿2.3.co;2.

S. L. Smith and S. L. Thomson. Effect of inferior surface angle on the self-oscillation of a computational vocal fold model. *The Journal of the Acoustical Society of America*, 131(5):4062–4075, 2012. DOI 10.1121/1.3695403.

S. L. Smith and S. L. Thomson. Influence of subglottic stenosis on the flow-induced vibration of a computational vocal fold model. *Journal of fluids and structures*, 38: 77–91, 2013. DOI 10.1016/j.jfluidstructs.2012.11.010.

J. C. Stemple, N. Roy, and B. K. Klaben. *Clinical voice pathology: Theory and management*. Plural Publishing, 2018.

B. H. Story, I. R. Titze, and E. A. Hoffman. Vocal tract area functions from magnetic resonance imaging. *The Journal of the Acoustical Society of America*, 100(1):537–554, 1996. DOI 10.1121/1.415960.

J. Suh and S. Frankel. Numerical simulation of turbulence transition and sound radiation for flow through a rigid glottal model. *Journal of the Acoustical Society of America*, 121(6):3728–3739, June 2007. DOI 10.1121/1.2723646.

J. Sundberg and T. Rossing. The science of singing voice. *DeKalb: Northern Illinois University*, 1987. DOI 10.1121/1.399243.

J. G. Švec and H. K. Schutte. Kymographic imaging of laryngeal vibrations. *Current opinion in otolaryngology & head and neck surgery*, 20(6):458–465, 2012. DOI 10.1097/moo.0b013e3283581feb.

P. Sváček and J. Horáček. Finite element approximation of flow induced vibrations of human vocal folds model: Effects of inflow boundary conditions and the length of subglottal and supraglottal channel on phonation onset. *Applied Mathematics and Computation*, 319:178–194, 2018. DOI 10.1016/j.amc.2017.02.026.

S. Thomson. Investigating coupled flow-structure-acoustic interactions of human vocal fold flow-induced vibration. *The Journal of the Acoustical Society of America*, 138(3): 1776–1776, sep 2015. DOI 10.1121/1.4933619.

I. R. Titze. *Principles of Voice Production*. Prentice Hall: Englewood Cliffs, NJ, USA, 1994.

I. R. Titze and F. Alipour. *The myoelastic aerodynamic theory of phonation*. National Center for Voice and Speech, 2006.

L. Traser, P. Birkholz, T. V. Flügge, R. Kamberger, M. Burdumy, B. Richter, J. G. Korvink, and M. Echternach. Relevance of the implementation of teeth in three-dimensional vocal tract models. *Journal of Speech, Language, and Hearing Research*, 60(9):2379–2393, 2017. DOI 10.1044/2017_jslhr-s-16-0395.

E. Vaiciukynas, A. Verikas, A. Gelzinis, and M. Bacauskiene. Detecting parkinson's disease from sustained phonation and speech signals. *PloS one*, 12(10), 2017. DOI 10.1371/journal.pone.0185613.

J. Valášek. *Numerical Simulation of Fluid-Structure-Acoustic Interaction in Human Phonation*. PhD thesis, Czech Technical University in Prague, 2021.

J. Valášek, M. Kaltenbacher, and P. Sváček. On the application of acoustic analogies in the numerical simulation of human phonation process. *Flow, Turbulence and Combustion*, pages 1–15, 2018. DOI 10.1007/s10494-018-9900-z.

D. d. Vasconcelos, A. d. O. C. Gomes, and C. M. T. d. Araújo. Vocal fold polyps: literature review. *International archives of otorhinolaryngology*, 23:116–124, 2019. DOI 10.1055/s-0038-1675391.

R. Verstappen. When does eddy viscosity damp subfilter scales sufficiently? *Journal of Scientific Computing*, 49(1):94–110, 2011. DOI 10.1007/978-94-007-0231-8_38.

H. K. Versteeg and W. Malalasekera. *An introduction to computational fluid dynamics: the finite volume method*. Pearson Education: London, UK, 2007.

A. Vreman. An eddy-viscosity subgrid-scale model for turbulent shear flow: Algebraic theory and applications. *Physics of fluids*, 16(10):3670–3681, 2004. DOI 10.1063/1.1785131.

B. Vreman. *Direct and large-eddy simulation of the compressible mixing layer*. PhD thesis, Holland: University of Twente, 1995.

C. A. Vreugdenhil and J. R. Taylor. Large-eddy simulations of stratified plane couette flow using the anisotropic minimum-dissipation model. *Physics of Fluids*, 30(8):085104, 2018. DOI 10.1063/1.5037039.

J. Wolfe, M. Garnier, and J. Smith. Vocal tract resonances in speech, singing, and playing musical instruments. *HFSP journal*, 3(1):6–23, 2009. DOI 10.2976/1.2998482.

Q. Xue, X. Zheng, R. Mittal, and S. Bielamowicz. Computational study of effects of tension imbalance on phonation in a three-dimensional tubular larynx model. *Journal of Voice*, 28(4):411–419, 2014a. DOI 10.1016/j.jvoice.2013.12.016.

Q. Xue, X. Zheng, R. Mittal, and S. Bielamowicz. Subject-specific computational modeling of human phonation. *The Journal of the Acoustical Society of America*, 135(3):1445–1456, 2014b. DOI 10.1121/1.4864479.

A. Yoshizawa and K. Horiuti. A statistically-derived subgrid-scale kinetic energy model for the large-eddy simulation of turbulent flows. *Journal of the Physical Society of Japan*, 54(8):2834–2839, 1985. DOI 10.1143/jpsj.54.2834.

A.-P. Zahiri and E. Roohi. Anisotropic minimum-dissipation (AMD) subgrid-scale model implemented in openfoam: verification and assessment in single-phase and multi-phase flows. *Computers & Fluids*, 180:190–205, 2019. DOI 10.1016/j.compfluid.2018.12.011.

C. Zhang, W. Zhao, S. H. Frankel, and L. Mongeau. Computational aeroacoustics of phonation, part ii: Effects of flow parameters and ventricular folds. *The Journal of the Acoustical Society of America*, 112(5):2147–2154, 2002a. DOI 10.1121/1.1506694.

Z. Zhang. Mechanics of human voice production and control. *The Journal of the Acoustical Society of America*, 140(4):2614–2635, oct 2016. DOI 10.1121/1.4964509.

Z. Zhang, L. Mongeau, and S. H. Frankel. Experimental verification of the quasi-steady approximation for aerodynamic sound generation by pulsating jets in tubes. *The Journal of the Acoustical Society of America*, 112(4):1652–1663, 2002b. DOI 10.1121/1.1506159.

W. Zhao, C. Zhang, S. H. Frankel, and L. Mongeau. Computational aeroacoustics of phonation, part i: Computational methods and sound generation mechanisms. *The Journal of the Acoustical Society of America*, 112(5):2134–2146, 2002. DOI 10.1121/1.1506693.

S. Zörner, P. Šidlof, A. Hüppe, and M. Kaltenbacher. Acoustic perturbation equations and lighthill's acoustic analogy for the human phonation. In *Proceedings of Meetings on Acoustics ICA2013*, volume 19, page 060309. ASA, 2013. DOI 10.1121/1.4806760.

S. Zörner, P. Šidlof, A. Hüppe, and M. Kaltenbacher. Flow and acoustic effects in the larynx for varying geometries. *Acta Acustica united with Acustica*, 102(2):257–267, 2016. DOI 10.3813/AAA.918942.